Investigation of depositional processes in pyroclastic surges: a large-scale experimental approach

A thesis presented in partial fulfilment of the requirements for the degree of

Master of Science

In

Earth Science

At Massey University, Manawatū,

New Zealand.

James Ardo

2022

Abstract

Dilute pyroclastic density currents (dilute PDCs or pyroclastic surges) are frequent and highly lethal phenomena found on volcanoes. They are hot flows of particles and gas that are capable of inflicting significant damage to life and infrastructure. The study and interpretation of sedimentary structures of their natural deposits have been invaluable in recognizing and characterizing their internal flow dynamics. Traditionally, these field based observations and interpretations are largely based on concepts from sediment transport mechanisms developed for fluvial and aeolian systems. Nonetheless, how well these analogies capture sediment transport in PDCs is still unclear, due to a lack of direct measurements inside these currents because of their inherent hostile nature.

This thesis presents the results from large-scale experiments, where scaled hot dilute PDCs were synthesised on a variable substrate roughness, in order to investigate sedimentation processes and lateral evolution of sedimentary structures. Proximal to distal evolution of the deposit emplaced by the experimental currents display high resemblance to deposits emplaced by natural PDCs. The proximally emplaced regressive structure composed of massive, poorly sorted lithofacies is comparable to proximal breccias observed in real world deposits. At medial to distal runout lengths, the experimental flows emplace a deposit with a characteristic ‘tripartite’ geometry that is often found in deposits of blast-like surges. This study finds that the tripartite geometry of experimental dilute PDCs reflects the passage of a flow with i) a head (responsible for the rapid deposition of massive layer A); ii) a body (responsible for tractional bedload aggradation of the stratified layer B); and iii) a tail and buoyant ash cloud (responsible for grain-by-grain aggradation of layer C in weakly tractive conditions). The experimental flows confirm the existence of a non-depositional flow front. Deposits emplaced by the flows propagating on contrasting roughness substrate are very comparable. Analogous deposition despite differing roughness conditions are due to the flow’s ability to deposit and subsequently travel on its own deposit which acts as a roughness substrate. Insights from the internal flow structure (velocity, density, and dynamic pressure) reveal that non-deposition and erosional phases are characterised by the passage of coherent turbulent structures, where episodes of elevated sedimentation rates represent periods between the passage of coherent turbulent structures. This research will help better understand the relationship between the observed sedimentary structures and the internal flow structure of by-passing dilute PDCs, which will ultimately add more understanding to the interpretations of natural dilute PDC deposits.

Acknowledgements

I would like to extend my appreciation for excellent supervision and constant guidance, whether be it for professional or personal development, by Gert Lube and co-supervisor Ermanno Brosch, without whom the contents of this thesis would not come to fruition.

The assistance of Daniel Uhle in running the experimental series and troubleshooting python codes; the support from Lucas Corna in the setup and running of PELE; the help of Hayden Jones in post-experiment sampling; and the setup and processing of the laser scanner by Gabor Kereszturi is also acknowledged with thanks.

The assistance and tutelage in proper lab procedures and constant support by Anja Moebis, and the organisation of financial support by Kate Arentsen is also acknowledged with thanks.

Thank you especially to the friends who are always supportive, especially Ciaran, Becki, Aimee, Jeremy, Daniel, Ben, and Jonathan. The many different mentors who guided me throughout these years, particularly Julie Palmer, are also recognized.

I am grateful for the legacy of investment in education by my grandfather and father that has paved my way to realise this opportunity.

And finally, to my wife and life-long partner who is always supportive and patient with proof-reading, Ruth Ardo.

Table of contents

List Of Figures

List of tables

1. Introduction

1.1 Foreword

Pyroclastic density currents (PDCs) are complex and dangerous phenomena associated with explosive volcanism (Brosch et al., 2021; Lube et al., 2020; Sulpizio et al., 2014). PDCs sweep across the volcanic landscape as highly turbulent, fast-propagating (tens to hundreds of meters per second), long-reaching (up to several hundreds of kilometers), ground-hugging mixtures of hot pyroclastic material (up to eruptive temperatures c. 600-1000°C) and gasses that overcome anything in their path (Cronin et al., 2013; Jenkins et al., 2013; Lube et al., 2014; Lube et al., 2020). Their capacity to inflict significant damage to life, environment and infrastructure is the consequence of their flow hazards which are generated through internal dynamic pressures (up to 100s of kPa), high temperatures (up to 600-1000°C can inflict significant burns), and asphyxiating effects of ash (Clarke & Voight, 2000; Gardner et al., 2018; Valentine, 1998). Over 100 million people worldwide may be exposed to hazards posed by PDCs, and understanding their behavior is essential to reducing the risks they pose to society (Brosch et al., 2021; Small & Naumann, 2001).

With their high mobility, velocities, and dynamic pressures, PDCs have been responsible for over 90,000 volcanic fatalities globally since 1600 CE (Auker et al., 2013). The earliest scientific study, coming from the notable 1902 eruption of Mount Pelée on Martinique which resulted in the loss of 28,000 lives, underlined the difficulty to elucidate the inner workings of PDCs (Bourdier et al., 1989; Lacroix, 1904). Sparse observation of the exterior ash cloud with no internal measurements led to many speculations about the inner working of these volcanic flow phenomena (Dufek, 2016). Despite the loss of thousands of lives, advancements in the understanding of PDC dynamics and flow evolution during propagation stagnated until the events of the 1980 eruption of Mount St. Helens (Hoblitt, 1986; Lipman & Mullineaux, 1981). The enormous quantity of observations made on the eruption of Mount St. Helens allowed for a detailed understanding of the eruptive sequence, and stratigraphy of the blast deposits (Belousov et al., 2007). Since then, the continual 21st century population growth and development near volcanoes has led to the drastic increase of exposure of people and infrastructure to PDCs (Auker et al., 2013). In the past decade alone, PDC forming eruptions in Mt. Merapi (2010, Indonesia), Mt. Ontake (2014, Japan), Mt. Sinabung (2014 & 2016, Indonesia), Volcán de Fuego (2018, Guatemala), Mt. Stromboli (2019, Italy) and most recently White Island (2019, New Zealand) has resulted in the loss of 650 lives (Lube et al., 2020).

1.2 Current understandings in PDC research

PDCs are a type of particle-laden gravity current which cover a wide range of flow types, ranging from high concentration/density granular flows to less concentrated/more dilute, turbulent flows (Dufek, 2016). The dilute endmember of PDCs, also known as pyroclastic surges, represent the low particle concentration field of the PDC spectrum. Dilute PDCs are characterized with a bulk flow particle concentration of less than 1 vol.% (Wohletz, 2001). Dilute PDCs are characterized by high degrees of turbulence, velocity, temperatures, dynamic pressures and mobility. Despite their low flow solids concentrations, these density stratified flows can cause vast-ranging devastation (Brosch et al., 2021; Valentine, 1998). The current understanding of internal PDC mechanisms have stemmed from estimates formed from broad flow approximations mostly through indirect observations. Bulk flow properties have been inferred from deposit and sedimentary characteristics whilst borrowing concepts from turbulent boundary layer theory and hydraulic sediment transport (Brosch et al., 2021). These techniques were developed to utilize deposit information, such as particle size, shape and density, as proxies to infer local bulk PDC flow properties such as velocity, density, and thickness (Dellino et al., 2008; Dioguardi & Mele, 2018). Bulk flow data derived from sedimentary and depositional features (Branney & Kokelaar, 2002; Sparks, 1976), have been complemented by occasional rare direct measurements from geophysical sensors (Scharff et al., 2019), and from analogue and theoretical numerical modelling (Dufek, 2016; Smith et al., 2020; Sulpizio et al., 2014; Valentine, 1987).

Sedimentary structures in a deposit have been classically used to interpret and understand the internal behavior of the flow that led to their emplacement (Best & Bridge, 1992; Bouma et al., 1962; Middleton, 1965). Pioneering work on dilute PDC deposits was conducted by comparing deposits to those generated by turbulent debris-laden nuclear base surges during nuclear weapon tests (Fisher & Waters, 1969; Valentine, 1998). The various sedimentary features, characteristic for dilute PDCs, such as cross-stratification, progressive and regressive dunes, chute and pool structures, and ripple bedforms are interpreted to have been emplaced by tractional processes known from sedimentology (Douillet et al., 2013; Schmincke et al., 1973). Moreover, applying concepts from hydrodynamics, dilute PDC deposits are interpreted to be deposited under supercritical flow conditions (Crowe & Fisher, 1973; Fisher & Waters, 1969). Unlike their dilute counterpart, the denser and more granular-type PDCs are characterized to be more voluminous (dilute PDCs are typically < 1km^3) , and lack any sedimentary structures, i.e. deposits are massive in appearance (Branney & Kokelaar, 2002; Sparks, 1976).

The characterization and interpretation of PDC deposits has played a key role in distinguishing past eruption styles and PDC dynamics, which resulted in an increase in hazard forecasting aiding decision making. However, these studies have fallen short of satisfactorily characterizing the intricacies of such flow mechanisms presented by a PDC. This is due to the heavy reliance on interpreting sedimentological and depositional mechanisms of dilute PDCs from those observed in sub-aqueous, fluvial and aeolian environments (Brosch & Lube, 2020; Lube et al., 2020). Drawing interpretations on PDC dynamics from these analogue systems are arguably too assumptive, and unlike these very well observed, measured, and quantified analogues (Best & Bridge, 1992; Bouma et al., 1962; Hjulstrom, 1935; Livingstone et al., 2007; Middleton, 1965), in situ dilute PDC sedimentation processes have never been properly measured, characterized, and observed. Despite the large amount of progress in studying PDC deposits over the past several decades (Dellino & La Volpe, 2000; Dellino et al., 2008; Dioguardi & Mele, 2018), there are still several shortcomings that must be addressed. Methods used in interpreting time-integrated velocity, temperature and density properties of dilute PDCs from deposits still cannot describe the complex temporal changes of the propagating flow. Consequently, knowledge regarding the spatiotemporally evolving internal flow structure and mechanisms remain sparse. For example, dilute PDCs tend to temporally be non-depositional, which limits the use of the techniques outlined above for hazard assessment (Lube et al., 2020).

In an effort to further improve hazard forecasting, and consequently better decision making, the relationship between deposit characteristics and PDC flow behaviors must be better understood. As natural PDCs are too dangerous to be directly measured and observed, several analogous laboratory experiments have been developed in the past two decades. Classically, parallels has often been drawn between the inner mechanisms of the dilute PDC system and to those observed in aqueous gravity currents (i.e. Huppert & Simpson, 1980; Simpson, 1999), but there are fundamental differences in aqueous gravity currents and naturally occurring hot volcanic PDCs. The differences include, but are not limited to, density contrasts of particle and fluid phases, compressibility of the particle carrier phase, extent of turbulence magnitudes, viscosity of the fluid phase, and density contrast between the flow and the ambient fluid. Limitations in understanding the range of fluid-particle transport processes associated with the complex spatiotemporal evolution of PDCs restrict the ability to interpret dilute PDC deposits. The ability to do so is key, charactering and linking deposit features to the flow's internal dynamics is crucial to understand the mechanisms that generate flow hazard potential. Moreover, aqueous and small bench-top experiments that have been designed to synthesize simplified end-member PDCs did not dynamically and kinematically scale to their natural counterparts. This further demonstrates the complexity of characterizing the natural processes occurring in a PDC (Burgisser et al., 2005; Lube et al., 2015). Aqueous and small bench-top PDC experiments are afflicted by several scaling limitations and are thus not suitable for testing and validation purposes required to progress current flow models.

Recent experimental advances have focused on generating scaled flows using novel large-scale approaches, generating direct insights, measurements and observations into PDCs (Andrews & Manga, 2011; Dellino et al., 2007; Lube et al., 2015). The pyroclastic flow eruption large scale-experiment (abbreviated as PELE), located at Massey University, is a large-scale experimental apparatus capable of producing scaled dense and dilute end-member PDCs (Lube et al., 2015). PELE is an advanced, fully instrumented system that enables direct measurements and observations into both dense (Breard & Lube, 2017; Lube et al., 2015; Lube et al., 2019) and dilute PDCs (Brosch & Lube, 2020; Brosch et al., 2021). Flows synthesized in PELE utilize natural polydispersed volcanic material, and scale well to real world flow, featuring high degrees of turbulence (Reynolds >10^6), flow velocities up to 32 m s^{-1}, and flow runouts up to 35m. Recent dilute PDC generated using PELE (Brosch & Lube, 2020) have presented initial relationships between deposit and internal flow processes at one observer location, but to what extent these relationships hold or evolve in the spatiotemporal domain is still unknown.

1.3 Objectives of the study

This master's study is motivated by the limitations described in section 1.2, and the need to improve current understanding of PDCs to ultimately effectively predict the hazards posed by these flows. Through synthesizing a series of dilute PDCs, the goals of the study are to: i) characterize the intricate spatiotemporal evolution of deposition and erosion processes in PDCs; and ii) interrogate the potential relationships between the evolving flow and deposit characteristics.

The study is based on the research hypothesis that, with well-defined input and boundary conditions that act as analogues to natural boundary conditions, the natural transport and sedimentation processes of dilute PDCs can be synthesized and characterized in a large-scale experiment environment. The experimental series conducted in this study differs from previous studies by: i) running two sets of experiments with the same initial input conditions, but with different substrate roughness to investigate the influence of variant substrates have on sedimentation/erosion processes; and ii) utilizing four observation locations along the PDC runout path, as opposed to one observer location presented in Brosch and Lube (2020).

In order to further understanding of depositional processes associated with dilute PDCs, this research was guided by the following research objectives:

Objective 1: In experimental dilute PDCs, measure the spatiotemporal deposition and compare the sequence of experimental deposits with that of natural deposits documented in the literature.

Objective 2: By comparing the spatiotemporal deposition of experimental dilute PDCs over hydraulically smooth and rough surfaces, investigate possible effects of the bottom roughness on deposition.

2. Methodology

2.1 Large scale experimental setup

On volcanic flanks, it is deemed too large of a risk to directly observe and measure inside naturally occurring PDCs, and the undertaking to peer into the inner mechanics of PDC is immediately hazardous to life. Therefore, there is a lack of internal measurements and real-world observations from past PDC events. At the **P**yroclastic flow **E**ruption **L**arge-scale **E**xperiment, or PELE for short, however, large-scale, high-temperature and high energy experimental PDCs are readily synthesisable under safe, controlled conditions. PELE is designed and built with the aim of i) characterising transport and deposition mechanisms of PDCs: ii) understanding gas-particle coupling processes inside PDCs; iii) demonstrating how changing boundary conditions (e.g., initial flow conditions, material properties, temperature, bed roughness, discharge height) may influence flow behaviours; and iv) deriving a benchmark dataset to build and validate numerical PDC models (Lube et al., 2015). The experimental laboratory was installed in 2013 in a large indoor 16m tall, 25m long x 18m wide, old Boiler house building located at Massey University, Manawatu, New Zealand.

PELE is the second of two facilities capable of synthesising large-scale PDC analogues using natural volcanic materials, with the other being an older setup located in Italy. The Italian setup generates relatively dilute PDCs through asymmetric column collapse of volcanic material from source (Dellino et al., 2007). However, PELE can produce more energetic, higher volume and particle density PDCs under longer material discharge conditions in a channelised setting through vertical gravitational free-fall of the experimental mixture. PELE can produce PDCs with up to 4 t of natural volcanic material, and the capability of heating the material up to 400 °C, producing flows with velocities up to 30m s^{-1}, with flow thicknesses ranging from 2 m up to 4.5 m, and a total runout distance of 35m before hitting a natural barrier.

Figure 1-1 highlights the current setup of PELE which is divided into five main structural components: 1) The tower; 2) The hopper; 3) The shrouding; 4) The channel; and 5) The runout. These elements are outlined below.

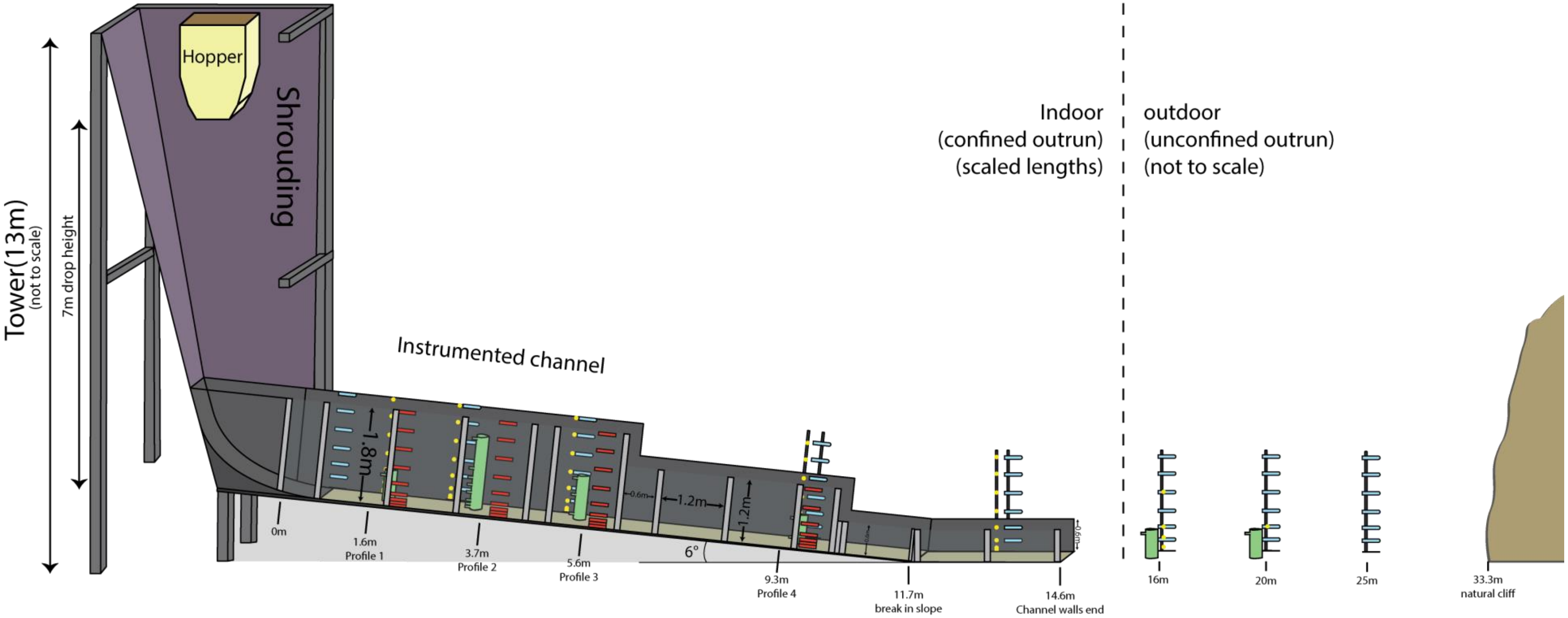

Figure 2-1 : Current setup of PELE. The 13 m tall steel tower supports a custom designed hopper capable of holding volumes up to 0.7m^3 and heating materials up to 400 °C. The discharge height (distance from the base of the hopper to the base of the slope) is 7m. The instrumented channel measures 11.7 m in length, 0.5m in width, and is inclined at an angle of 6°. The channel changes to a flat runout at 11.7m and remains confined until 14.6m, from where the flow propagates under unconfined until stopped by a natural cliff-face at 33.3m. Piezoelectric pressure sensors (green) are mounted on specially designed wing shaped profiles that sit in the mid-point of the channel. Time-resolved flow samplers (red rectangles) are installed on the window channel side, while time integrated sediment samplers (blue rectangles) and high-speed thermocouples (yellow dots) are installed on the channel steel back wal

1. *The Tower.* Standing at 13m high, with a width and length of 3m, the tower is a large steel structure that can support two differently sized hoppers, with the intention of varying discharge volumes and discharge. The hoppers' positions within the tower can be adjusted vertically and horizontally.
2. *The Hopper.* The smaller of the two hoppers is used in the experimental series conducted for this thesis. This hopper is designed to produce repeatable hot and dilute PDCs under constant discharge conditions. The maximum total filling volume is $0.7m^{3.}$ To generate hot PDCs, a heating mechanism with a total power flux of 24 kW m^{-3} is installed inside the hopper. Furthermore, the hopper is thermally insulated with rock wool to ensure effective heating and minimize loss of thermal energy. Four ZEMIC loadcells (each with a capacity of 1500 kg) allow for measuring material discharge rates from the hoppers which to ensure constant experimental input boundary conditions
3. *The Shrouding.* A fire-resistant tarpaulin is fitted tautly between the hopper and the channel. This not only guarantees that the discharged volcanic mixture channelizes, but it also ensures minimal entrainment of ambient air on during vertical free-fall of the material towards the channel.
4. *The Channel.* A 12 m long and 0.5 m wide inclinable steel channel sits underneath the hopper. The channel floor is made of steel and designed to fit in modular pieces of roughness plates. The "0m" point inside the channel is set right after the impact zone from where the flow expands horizontally downslope inside the channel. The channel walls are made of black painted steel on one side, and a tempered glass on the other side. The channel walls are 1.8 m in height for the initial 6.4 m (from the impact zone 0, to 6.4m), and decrease to 1.2 m in height (from 6.4 to 10.6 meters). Piezoelectric pressure sensors (PCB PIEZOTRONICS 106B51) sit on a specially designed wing profiles on different heights along designated distances (1.6m, 3.7m, 5.6m, 9.6m). Along the steel wall, vertical profiles of thermocouples, and bulk flow sediment samplers are installed. Moreover, a second set of time-resolved sediment samplers are installed on the glass wall.
5. *The Runout.* As the flow propagates downstream, the inclined channel terminates at 11.7 m. From this break in slope point onwards, the channel walls decrease to 0.6 m in

height up to 14.6m. From 14.6 m until 33.5 m (natural cliff face) the flow propagates outside of the experimental building under unconfined conditions. In this runout section, two sets of piezoelectric sensors and thermocouple profiles are installed at 16m and 20m distance, respectively, along with three sets of sediment sampler profiles located at 16m, 20m, and 25m.

2.2 Experiment designs

An experimental series consisting of three experiments was investigated as part of this thesis with the goal of characterising pyroclastic surge deposits. The three experiments were performed under identical conditions (initial solid mass; solid mass temperature; and atmospheric conditions (ambient temperature and humidity)), while changing only the substrate roughness. Experiment 1 featured a rough substrate made of 4-8mm rock pebbles (effective roughness of 5 mm). Experiment 2 was characterised by a smooth MDF surface (hydraulically smooth). The objective of this experimental series was to see how substrate roughness impacts on dilute PDC sedimentation processes and depositional characteristic.

2.2.A Boundary Conditions

PELE is by design able to synthesise a wide range of replicable PDCs by means of systematic changes and variations of starting and boundary conditions. In this thesis, a set of three different experiments are conducted under the following boundary conditions (summarized in Table 2-1):

- *Initial Solid Mass*. One of the main parameters that affects the potential energy of the system is the initial solid mass. Thus, the mass of the material used for all the experiments is kept constant at 125kg. The constant mass ensures constant discharge condition between all the experiments.
- *Channel geometry*. The channel width and inclination of 0.5m and 6° degrees, respectively, are maintained constant throughout the experimental series.
- *Substrate/Bed roughness.* The experimental series is designed to be performed on differing substrate roughness. The first (1) experiment will focus on a rough surface, with a substrate of rounded fine pebbles between -2 to -3 ϕ in size (4-8mm). The second (2) experiment will be performed on a smooth MDF surface.
- *Grainsize Distribution.* The experimental material will consist of grainsizes ranging from -4 to 9 ϕ (16 mm to 2 µm), and fines content (>4ϕ) of c. 20 wt%. The same

material will be used across all experiments to guarantee similar particle transport and sedimentation mechanisms. Further details to the experimental material are given in the next section.

- *Temperature of material.* The hopper can heat up the experimental mixture up to 400°C, as well as running experiments at ambient temperatures (c. 20°C). For this experimental series, the temperature will be kept at a constant 125°C.
- *Drop height.* The drop height of the volcanic material influences the impact velocity. With the current experimental setup, the drop height is set to 7m, which produces impact velocities up to c. 7 m s^{-1}.

Table 2-1 Summary of boundary conditions set for the experimental series

Parameter	**Experiment**	
	1	**2**
Initial Solid mass	125 kg	125 kg
Channel inclination	6°	6°
Channel width	0.5m	0.5m
Substrate roughness	-2 to -3 ϕ	Hydraulically Smooth
Grain size distribution	-4 to 9 ϕ	-4 to 9 ϕ
Fine ash content	20 wt%	20 wt%
Mixture temperature	120 °C	120 °C
Drop height	7m	7m

2.2.B Volcanic Material

The material used for the experiments is taken from natural PDC deposits originating from the 232 AD Taupo Ignimbrite (Hogg et al., 2011; Lowe & Pittari, 2021; Wilson & Walker, 1985). The material was sampled from two different facies of the Taupo ignimbrite and then mixed to account for spatial grainsize variability in the deposits. Grainsize distributions are gathered from combining standard manual sieving practices and laser particle size analyses. The first facies (S2) is taken from a deposit located 19km to the north-east of the inferred vent (38°43'8.90"S 176° 9'56.31"E, Figure 2-2). Grainsize distribution of the S2 deposit shows a unimodal distribution with a median grain size of c. 1.6 ϕ with fine ash (>4.5 ϕ) content of 3.7 wt% (Figure 2-3), which represents a proximal medium-ash ignimbrite deposit. The second facies (Hatepe) can be found around 7km south-east of the inferred vent location (38°51'27.90"S 176° 2'11.30"E, Figure 2-2). The Hatepe facies represents a proximal, fines-rich base of the Taupo ignimbrite represented by poorly sorted, trimodal distribution with a median grain size of c. 3.6 ϕ containing fine-ash (>4.5 ϕ) content of 43.65 wt% (Figure 2-3).

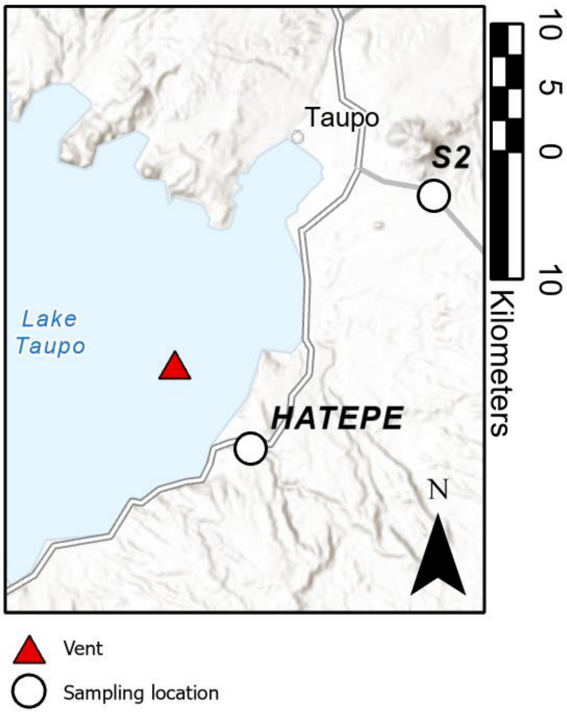

Figure 2-2: Sampling locations for the experimental materials. S2 deposit is a medium-ash ignimbrite facies that is located about 19km north-east of the vent location. The Hatepe deposit is a proximal fines-rich base deposit of the Taupo ignimbrite that roughly sits about 7km southeast from the vent.

Both facies are composed of clasts of quartz, feldspars, titanomagnetite crystals, and dense lithics along with glassy vesicular pumice and ash. Material collection was conducted under standard sampling procedures which include sampling deposits that are minimally affected by organic activity, and weathering. Material collected from both locations is cleaned from organic material and then sieved using a -4 ϕ standardised metal sieve, keeping the fractions that are sieved through. The materials are then placed into a 100 °C oven for around 4 to 7 days to remove moisture and afterwards stored into airtight containers in a dry storage room.

Given the variations in the natural grainsize distribution of the ignimbrite deposits, a mixture that reflects natural surge PDC is needed. Therefore, the mixture used for the experiments is a combination of the S2 and Hatepe deposits, with a weight ratio of 60:40, resulting in a grain size range from -4 to 9 ϕ. The represented grainsize distributions (Figure 2-4) show a statistical average result of three grainsize analyses from the separately collected volcanic deposits (S2 and Hatepe) as well as the final experimental mixture (Figure 1-4). The grainsize analyses show a highly reproducible result, thus, showing the homogeneity of the experimental mixture ensuring a reproducible flow.

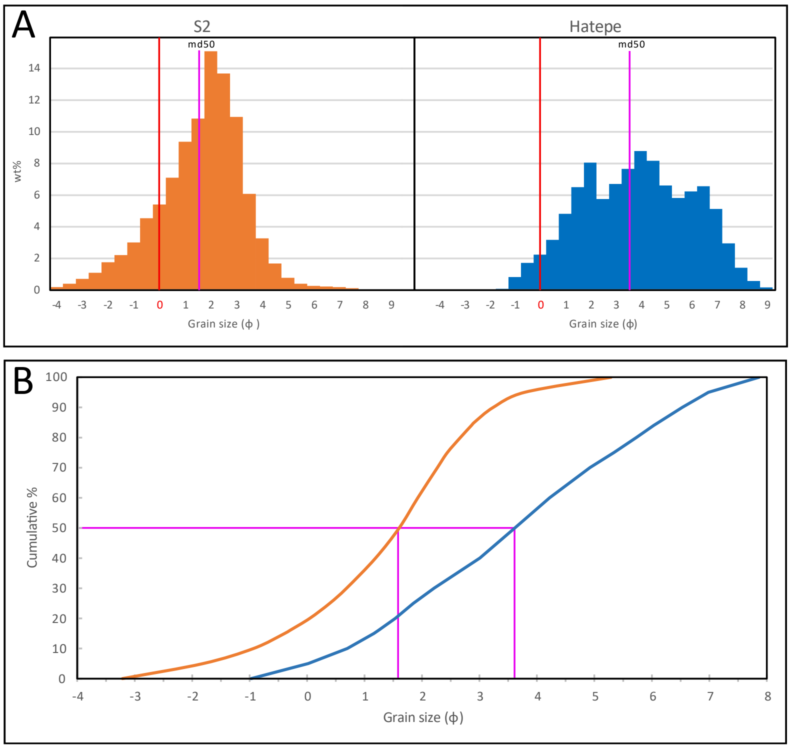

Figure 2-3 : A) Grainsize distribution of the two different facies used for the experimental mixture. Purple lines represent median values which sit at 1.6 and 3.6 ϕ respectively. B) Cumulative grainsize distributions of S2 (orange) and Hatepe (blue) components.

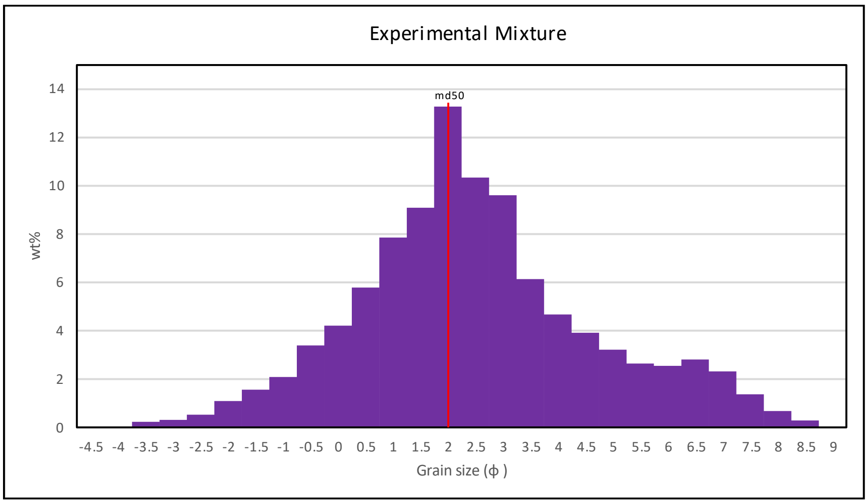

Figure 2-4: The final experimental mixture used during the experiments. The resultant mixture is the product of combining the proximal medium-ash facies (S2, 60 wt%) with the proximal fines-ash facies (Hatepe, 40wt%). The grain size distribution shows a bi-modal distribution, with a median grainsize of c. 2 ϕ, with fine ash (>4.5 ϕ) content of around 20 wt%.

2.2.C Scaling parameters and analysis

PELE allows to observe directly into the experimental flows which are scaled to real world PDCs. Large-scale experiments which allow to synthesise scaled conditions of natural PDCs minimise largely limitation of previous investigations done at a benchtop scale. Previous PELE experiments have consistently reproduced kinematic and dynamic scaling that closely resembles real world flows (Brosch & Lube, 2020; Brosch et al., 2021; Lube et al., 2015). In order to guarantee scaling resemblance between synthesised flow and real world dilute PDCs, relevant non-dimensional numbers must be compared (Table 2-2). The relevant non-dimensional numbers are Reynolds number (Re), Richardson number (Ri), thermal Richardson number (Ri_T), Froude number (Fr), Stokes number (S_T), Stability number (Σ_T), and Rouse number (P_n). Dilute PDCs, synthesised in PELE show an excellent agreement with natural PDCs in terms of kinematic, fluid-dynamic and thermodynamic processes. This is due to previous extensive scaling analyses and systematic testing of input and boundary conditions conducted at PELE. The usage of natural pyroclastic deposit material (natural grain size and density distribution), along with the variable temperatures as well as large length and energy-scales ensure that the conducted experiments reproduce excellent agreement with natural flows.

Non-dimensional numbers show excellent scaling with natural PDCs. In the synthesised flows, the Reynolds number (ratio of inertial and viscous forces, and characterises turbulence intensity) have observed values up to 1.5×10^6; Richardson numbers (stratification stability of turbulent flows, ratio of buoyant forces to shear forces) have values ranging from 0.01-10; thermal Richardson number (ratio of forced to buoyant convection) of 0.02-4.5; Stokes number (characterises particle coupling in the flow) values of 10^{-3}-10^{0}; and the Stability number (ratio of particle settling velocity relative to turbulent fluid motion) of 10^{-2}-10^{1}. These scaling results ensure close comparability to natural PDCs.

The channel configuration in PELE utilizes sidewalls which introduce boundary effects dissimilar to naturally occurring PDCs. To minimize these boundary effects, the use of scaled base surface roughness and the use of hydraulically smooth sidewalls (laminar layer thickness/sidewall roughness <5) are employed. Sensors are also installed to protrude through the boundary layer of the flow (thermocouples protrude several cm form the sidewalls, and pressure sensors sit in the middle of the channel). Past PELE experiments show minor boundary effects through observations of the shapes of cross-channel profiles of deposits, revealing slight deposit overthickening in the corners of the side walls (Brosch & Lube, 2020).

Table 2-2: Scaling parameters of dilute PDCs synthesised in PELE compared to naturally occurring PDCs. Modified from Brosch et al. (2021)

Parameter	Definition	Formula	PELE Dilute PDCs	Natural dilute PDCs
Particle diameter		d	10^{-6}-10^{-2}m	10^{-6} – 10^{-1} m
Solid density		ρ_S	350-2600 kg m^{-3}	300 - 2600 kg m^{-3}
Ambient density		ρ_A	0.8-1.2 kg m^{-3}	0.6 - 1.2 kg m^{-3}
Flow dynamic viscosity		μ_c	3×10^{-5}-3×10^{-3} kg m^{-1} s^{-1}	1×10^{-5}-4×10^{-3} kg m^{-1} s^{-1}
Velocities		U	< 0.5 – 9 m s^{-1}	10-200 m s^{-1}
Kinetic energy density		$\frac{\rho_C U^2}{2}$	10^{-2}-10^{3} J m^{-3}	10^{3}-10^{4} J m^{-3}
Buoyant thermal energy density		$\rho_C \frac{C_{p_C}}{C_{p_A}} \alpha T g h$	10^{1} – 10^{3} J m^{-3}	10^{3}-10^{4} J m^{-3}
Reynolds number (Re)	Turbulence intensity. Ratio of inertial to viscous forces	$\frac{\rho_c U h}{\mu_c}$	4.8×10^{4} – 1.5×10^{6}	3.3×10^{6}-6.7×10^{9}
Richardson number (Ri)	Stability of density stratification.	$\frac{\Delta\rho h g}{\rho_a U^2}$	0.01 – 10	0-10
Thermal Richardson number (Ri_T)	Ratio of forced to buoyant convection	$\frac{\Delta T \alpha h g}{U^2}$	0.02 – -4.5	0-5
Froude number (Fr)	Ratio of inertial to gravitational forces	$\frac{U}{\sqrt{g' h \cos(\theta)}}$	0.75 – -2	~ 1
Stokes number (S_T)	Particle coupling in the flow	$\frac{U_T \Delta U_i}{\delta g}$	1×10^{-3}-9.9×10^{0}	1.1×10^{-3}-9.7×10^{7}
Stability number (Σ_T)	Ratio of particle settling velocity relative of turbulent fluid motion	$\frac{U_T}{\Delta U_i}$	1.3×10^{-2}-3.2×10^{1}	2.8×10^{-6}-9.7×10^{9}
Rouse number (P_n)	Characterises sediment transport in a turbulent flow	$\frac{U_T}{k U_s}$	6.6×10^{-1}-1.9×10^{1}	10^{-3}-10^{2}

Scaling parameters, comparing values of dilute PDCs generated in PELE to values of natural dilute PDCs from Burgisser et al. (2005). Rouse number obtained from Choux and Druitt (2002). U- flow velocity; h - flow height; $\Delta\rho$- difference in flow and ambient density; ρ_c- flow density; ρ_a- ambient density; ΔT- difference in flow and ambient temperature; α- thermal air expansion coefficient; U_T- terminal fall velocity; ΔU_i- eddy rotation velocity; U_s- shear velocity; δ- eddy diameter; μ_c- dynamic viscosity of the flow; g- acceleration due to gravity; g'- reduced gravity; k- von Karman constant; and θ is the slope.

2.3 Sensors, Measurements & Data acquisition

2.3.A Cameras and Sensors

Table 2-3: Sensors and their quantity utilized in the PELE experiments, and associated measurements.

Sensor Type	**Name/Make**	**Amount**	**Specifications**	**Measurements**
High resolution, high speed cameras	*NAC Memrecam HX-7ST-839*	1	1920x1080, 500fps, Colour sensor	Velocity fields; particle concentration and density from volumetric filling of samplers. Flow outlines, flow height, and flow front kinematics. Time-resolved sediment height and sedimentation rates.
	NAC Hotshot 1280	1	1024x640, 500fps	
	Basler A2000-340km	4	1920x760, 500fps, Monochrome sensor	
High resolution, Normal/fast cameras	*GoPro Hero 3 to 6*	20	1920x1080, 30, 60, 120, 240 fps	
	Sony α6000	2	1920x1080, 50fps	
	Panasonic LUMIX TZ110	1	1920x1080, 50fps	
	Canon EOS 600D	1	1280x720, 50fps	
Laser Scanner	*Leica MS50*	1	1000 Hz, 1.0 mm scanning precision	Deposit thickness
Thermal Camera	*Infratec VarioCAM*	1	7.5 - 14 µm spectral range, 640 × 480, 50fps	Temperature distribution of unconfined flow
Temperature sensors	*TC Direct 410-345 Type K thermocouples*	45	Ultra fine wire (0.08mm dia) thermocouple, very fast response (c. 15ms) , -75 to 250 °C.	Flow temperature distribution
Pressure sensors	*PCB PIEZOTRONICS 106B51*	15	5 PSI measurement range, 1000 mV/psi sensitivity, 0.5 Hz Low Frequency response, 40kHz Resonant Frequency	Time-resolved flow dynamic pressures, and particle impacts
Hopper Load cell	*Zemic H8C-C3-1.5T-4B*	4	Maximum Capacity 1.5 t	Hopper Discharge rates, Material input weight

(i) High speed Cameras

A combination of six different high-speed cameras operating at 500fps at variable resolutions are used to record the passage of flow at four different static observer locations along flow runout (profiles marked at 1.6, 3.7 5.6, 9.3 meters). At the different profiles, the high-speed camera field of view is either the full height of the windows (1.8m) and c. 0.4-0.6m horizontally (for Profiles 1 and 2), or up to 1.2 m window height and c. 0.4-0.6m horizontally (for Profiles 3 and 4).High resolution, Normal/Fast speed Cameras

GoPro cameras (20 cameras; models range from Hero 3 to Hero 6) are installed throughout the PELE setup at various locations and various angles to observe the flow. They are set to observe: i) broad, lateral overviews of the flows at high resolution; ii) capture the filling of the time-resolved sediment samplers at high resolution at 60fps; iii) extend missing views above the highspeed cameras, at high resolution and frame rates of 120 and 240fps, respectively.

Additionally, four sedimentation cameras (2x Sony α6000, Panasonic LUMIX TZ110, and Canon Eos 600D) are operating with a frame rate of 50fps at the four profiles. The cameras are recording the basal section up to a maximum of 0.2m of the flow at a high resolution. These cameras are setup to record time-resolved sedimentation/erosional processes occurring as the flow passes past the static profile locations.

(ii) Laser Scanner

The Leica MultiStation 50 (MS50) is a laser scanner that is used to capture the deposit surface area of the channelized section in PELE. Before and after experiment 3D point cloud measurements are taken to quantify the deposited material. Two static geo-referenced reflectors (360-degree prism) are used as reference frames for the laser scanner to triangulate its position. Generated scans are georeferenced and geospatial data are processed in a geographic information system application (ArcGIS Pro).

(iii) Thermal Camera

A single Thermal camera (Infratec VarioCAM) is positioned at the unconfined runout section perpendicular to flow propagation to measure vertical temperature profiles of the flow.

(iv) Thermocouples

A total of 45 TC Direct 410-345 Type K thermocouple sensors are installed at various distances and heights to obtain direct heat measurements as the flow passes. The thermocouples are installed as vertical arrays at several profile locations (Table 2-4), on the steel wall of the channel. The sensors reach into the by-passing flow by being installed inside very small aluminium tubes (2.5mm outer diameter, 5 cm long) to both protect the sensors and ensure the thermocouple does not move during flow passage.

Table 2-4: Thermocouple profile locations and distribution.

Profile	1	2	3	4	5	Unconfined 1	Unconfined 2
Runout distance (m)	1.8	3.4	5.4	7	9.6	16	20
Sensor Count	8	8	8	8	8	4	1
Sensor Heights (m)	0.035, 0.085, 0.21, 0.45, 0.75, 1.1, 1.45, 1.8	0.035, 0.085, 0.21, 0.45, 0.75, 1.1, 1.45, 1.8	0.035, 0.085, 0.21, 0.45, 0.75, 1.1, 1.45, 1.8	0.035, 0.085, 0.21, 0.45, 0.75, 1.1, 1.45, 1.8	0.035, 0.085, 0.21, 0.45, 0.75, 1.1, 1.45, 1.8	0.08, 0.25, 0.45, 1.1	0.45

(v) Hopper Load cells

The hopper sits on four Zemic H8C-C3-1.5T-4B, which measure the mass of material in the hopper and during discharge.

2.3.B Flow and deposit samplers

Different types of sediment samplers are utilized in the experiments. The time-resolved samplers allow for time-resolved grainsize distribution measurements (and resulting particle solids concentration) of the flow, while the time-integrated samplers allow for obtaining bulk mass and grain size distribution of the flow and deposit.

Table 2-5: Flow deposit samplers and their amount used in the experiments.

Sampler Type	Specifications	Amount	Measurements
Time-resolved samplers	Square glass (borosillicate) tubes, 5 -15 cm length, square inner diameter of 1.3cm	34	Time-resolved volumetric, mass, grainsize filling rate. Sediment concentration and flow density
Time-integrated flow sampler	2.4x15.0 cm glass (borosillicate) test tubes	48	Bulk sediment transport information (mass and grainsize)
Time-integrated deposit sampler	Aluminium trays with 0.165m2	15	Final deposit grain size and mass distributions

(i) Time-resolved samplers

In order to obtain time-variant volume of the flow material, a total of 34 specially designed rectangular glass tubes are glued on to the channel glass wall in vertical arrays and filmed by fast speed, high resolution cameras. The rectangular glass tubes are 5-15 cm long, with a cross-sectional opening area of 1.96 cm^2. These tubes are opened on the upstream side to allow flow material to enter, and the downstream side is closed with two-layers of fine mesh (15 µm) that prevent the passage of particles but allows for air to exit. When a layer of sediment builds up on the fine back mesh, back-pressure effects are minimised through the large dimension of the upstream opening, which enables the passage of the gas phase back through the sampler. The deposited material within each tube can be temporally resolved, sampled, and analysed to acquire grainsize data.

(ii) Time-integrated samplers

Round glass tubes with an upstream opening are installed as vertical arrays on the steel wall of the channel (the tube opening sits 5cm into the flow from the channel wall). Suspended flow material passing the sampler point will be accumulated and generates a time integrated mass and grainsize information. The samplers have a cross sectional opening area of 3.5cm^2 and measure 15 cm in length.

(iii) Time-integrated deposit samplers

Aluminium trays (surface area of 0.165 m^2) are used to collect flow material that is deposited at the base of the channel and along the unconfined runout area. A total of 15 deposit samplers are used throughout the flow runout area at regularly spaced intervals following the flow centreline. Accumulated material is used to quantify deposit mass per area and grainsize evolution over runout distance.

2.4 Data Processing and Analysis

2.4.A Flow Geometry & internal flow parameters

After each experiment, there are large amounts of video data that require analysis in order to extract important flow parameters. Flow parameters such as flow front positions, flow geometry, velocity, density, temperature and solid concentration are extracted with methods described in the subsequent section.

(i) Flow front position and flow geometry

Flow front positions are obtained by converting video sequences to image sequences in VirtualDub2. Image sequences of the flow are then analysed using ImageJ, where flow front is tracked, mapped and exported as time-distance data set. Flow front mapping is achieved with a temporal resolution of 16 ms (60fps).

(ii) Particle image velocimetry

Velocity extraction workflow closely resembles the methods described by Brosch (2020) with slight changes (different PIVlab version, and improved photoshop pre-processing step). Image sequences are exported from high-speed (500fps, 2ms time resolution) video footages using VirtualDub2. Footage sequences ranging up to 4- 5.5 seconds (2000- 2750 frames) are analysed as part of the study. As part of the workflow (Figure 2-5), the images are pre-prepared using Adobe Photoshop(Figure 2-5, ii) before velocities are measured using particle image velocimetry (PIV) in MATLAB using PIVlab version 2.56 (Thielicke & Stamhuis, 2014).

In PIVlab, a region of interest (ROI) is defined, and further image pre-processing takes place. Contrast limited adaptive histogram equalization (CLAHE, PIVlab values of 50-100) and Wiener filter (PIVlab values of 3-4) setting are applied during PIVlab pre-processing to increase the readability of the image data (Figure 2-5, iii). The algorithm used for PIV is FFT (Fast-Fourier-Transform). This algorithm is a direct Fourier transform correlation which has multiple passes and deforming windows (important for real flows, where particle patterns can be sheared and rotated). The data will be analysed though multiple passes using FFT, starting with a relatively large interrogation area to initially calculate the displacement of the image data consistently (large interrogation areas will, however, result in a very low vector resolution), which is followed by smaller interrogation areas for subsequent passes (which produce a higher vector resolution, and noise). The many passes required by FFT also more computationally demanding. For the experiments, the interrogation windows are set to four passes following 256, 128, 64, 32 px in size, with the aim of producing a vector resolution of c. 1cm/vector. As for the newly added correlation robustness settings (Thielicke & Sonntag, 2021), the standard settings are used, as increasing the settings to high or extreme significantly increase computing resources.

The PIV algorithm analyses takes c. 5 hours to complete. Once completed, the resulting vector field is produced (Figure 2-5, iv). Vector information (px/frame) is converted to real world values (m/s) by calibrating the images to known distance (mm) and time (ms). Furthermore, velocity limits are applied to eliminate inaccurate values, that can occur from image noise, or algorithm errors. Resulting velocity data can be exported from PIVlab as .mat files of u and v velocity matrices, or as .txt of separated u and v velocity matrices of a defined vertical profile.

As the channel is inclined at an angle of 6°, the true u and v components are corrected in MATLAB.

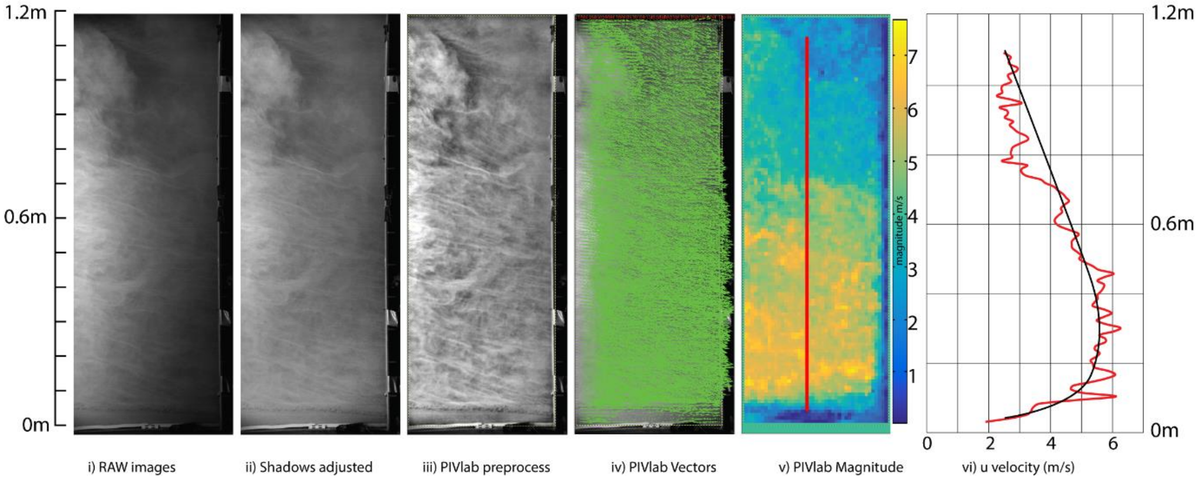

i) RAW images ii) Shadows adjusted iii) PIVlab preprocess iv) PIVlab Vectors v) PIVlab Magnitude vi) u velocity (m/s)

Figure 2-5: PIV workflow from raw images to final velocity, example taken from profile 1 (1.6m) at a flow after 2.03 seconds. i) Unaltered image from the Basler A2000-340km high speed camera. ii) Adobe Photoshop adjustments. iii) PIVlab pre-processing (CLAHE and Wiener filter). iv) Magnitude vector results from PIV analysis. v) Velocity magnitude visualized; red line indicates extracted velocity profile location. vi) Extracted u velocity (red) and mean velocity (black).

(iii) Particle solids concentration

The time-resolved particle concentration can be calculated through the direct observation of the time-resolved samplers. Vertical arrays of time-resolved samplers are filmed through high resolution, fast-speed cameras, in order to extract time-resolved vertical concentration distribution within the flow. Captured flow material area (A) are then mapped at a high temporal and spatial resolution using a combination of VirtualDub2 and ImageJ.

Between a time step T and $T+t$, the deposit volume (V_d)can be extracted by:

$$V_d = A\,w \qquad \text{Eq. 2-1}$$

Where w is the inner width of the time-resolved sampler. The deposit volume may be calculated in this manner as the deposit filling is observed to occur homogenously across the sampler.

Volumetric flux (Q_f in $m^3\ s^{-1}$) can be calculated through multiplying a 20ms averaged (moving average) u velocity between the time step T and $T+t$ and the tube opening area (A_o):

$$Q_f = \bar{u}A_0 \qquad \text{Eq. 2-2}$$

Thus, Volumetric flow (V_f in m^3) between times T and $T + t$ is the product of Q_f and t:

$$V_f = Q_f\, t \qquad \text{Eq. 2-3}$$

Solid concentrations (C_s) between times T and $T + t$ is the quotient of V_d (with a porosity constant of ε, set to c. 45%) and V_f:

$$C_s = \frac{V_d(1-\varepsilon)}{V_f} \qquad \text{Eq. 2-4}$$

The method outlined generates continuous, high-resolution, spatial and time-variant particle solid concentrations at defined profile locations during flow passage.

(iv) Flow density

Flow density (ρ_c) can then be calculated from solid concentrations (C_s) (Hallworth & Huppert, 1998) following:

$$\rho_c = (1 - C_s)\rho_a + C_s\rho_p \qquad \text{Eq. 2-5}$$

Where ρ_a is the ambient density, and ρ_p the particle density.

(v) Dynamic pressure

Time (t) and height (z) resolved Dynamic pressures (P_{dyn}) are then obtained by combining velocity magnitude ($|\vec{v}|$) and flow density (ρ_c)

$$P_{dyn} = \frac{\rho_c}{2}|\vec{v}|^2 \qquad \text{Eq. 2-6}$$

(vi) Temperature

Temperatures of the bypassing flow are directly observed by the vertical arrays of thermocouples and recorded by the data logging system (three data loggers: NI cDAQ-9171, NI cDAQ-9174 and NI cDAQ-9178). The resulting data sets produce a set of vertically distributed temperature profiles with a temporal resolution of c.10ms.

2.4.B Flow deposit analysis

(i) Grain Size Analysis

Standard procedures were applied to obtain grain size distributions of the flow material collected in the sediment sampler profiles and deposits sampler. Materials were first manually hand sieved using standardized lab sieves down to 2ϕ (200 µm), where fractions smaller than 2ϕ were processed through a laser diffraction particle distribution analyser

(Horiba Partica LA-950V). In order to compile and analyse the grain size distribution, the grain size statistics package GRADISTAT program is utilized (Blott & Pye, 2001).

(ii) Time-resolved deposit height and sedimentation rate

Four dedicated high resolution, fast cameras (50fps) directly observe the lowermost c. 0.05-0.1m thick region of the flow at designated profile locations (1.6, 3.7,5.6, 9.3m). Recorded footages are exported as image sequences in VirtualDub2 and subsequently analysed using ImageJ. Cameras are set to record at a relatively low shutter speed to easily identify static deposit to the moving flow. Deposit heights are mapped and recorded into MS Excel. Sediment heights are recorded at a high resolution of c. 0.5mm and temporal resolution of 20ms. Sedimentation rates are finite differences averaged over a window of 200ms.

(iii) Time & Height resolved flow grainsize distribution

Between a time step T and $T + t$, the mapped deposit volume (V_d) are extracted from the time-resolved samplers and processed as described in 1.4.B (i) Grain Size Analysis). The resulting grain size data produces a time and height resolved grain size distribution at the previously defined profile locations. The time steps (t) are 500ms, yielding a dataset at half a second of resolution.

(iv) Deposit Geometry

The runout section was scanned before and after experimental runs using the Leica laser scanner. Point cloud information were processed in ArcGIS Pro. Resulting rasters were interpolated in ArcGIS using the inverse distance weighted (IDW) method. Differences in pre and post experiment scanning thicknesses were used to determine the net deposit thickness over distance for each experiment

3. Results

3.1 Overall flow characteristics

In this research, two experimental PDCs were generated under similar starting conditions, but propagating over hydraulically smooth and rough surfaces. Section 3.1 provides an overview of the general flow and deposit characteristics created in these two experimental situations.

At the onset of each experiment, the hot (c. 120 °C) 125kg volcanic material discharged from the elevated hopper and accelerated vertically from a position of rest due to gravity. For both the rough substrate and the hydraulically smooth substrate experiments, the mixture impacted onto the channel c. 1.8s after trap door opening. Instantly after impact, the confined mixture laterally expanded into the channel and propagated downstream where it entrained ambient air and underwent significant dilution. At c. 0.3 s after impact, a distinctive gravity current structure (Figure 3-1 a) with a bulk density of c. 3.15 kg m^{-3} developed, comprised of leading 1.5-2.5 m thick flow head structure. This was characterized by an elevated frontal edge, or the *nose* and a c. 1-1.5m thick flow *body* and *tail*, topped by the flow *wake*. The wake formed due the shedding of vortexes produced in the rear of the head. During its runout to c. 24 m in around 12 seconds, the density of the experimental PDCs decreases to c. 0.01 vol.% due a combination of entrainment of ambient air and particle deposition. The highly diluted flow rose buoyantly and formed a buoyant ash cloud that sedimented fine ash particles above the deposit surface over the duration of several minutes after the cessation of the main flow propagation.

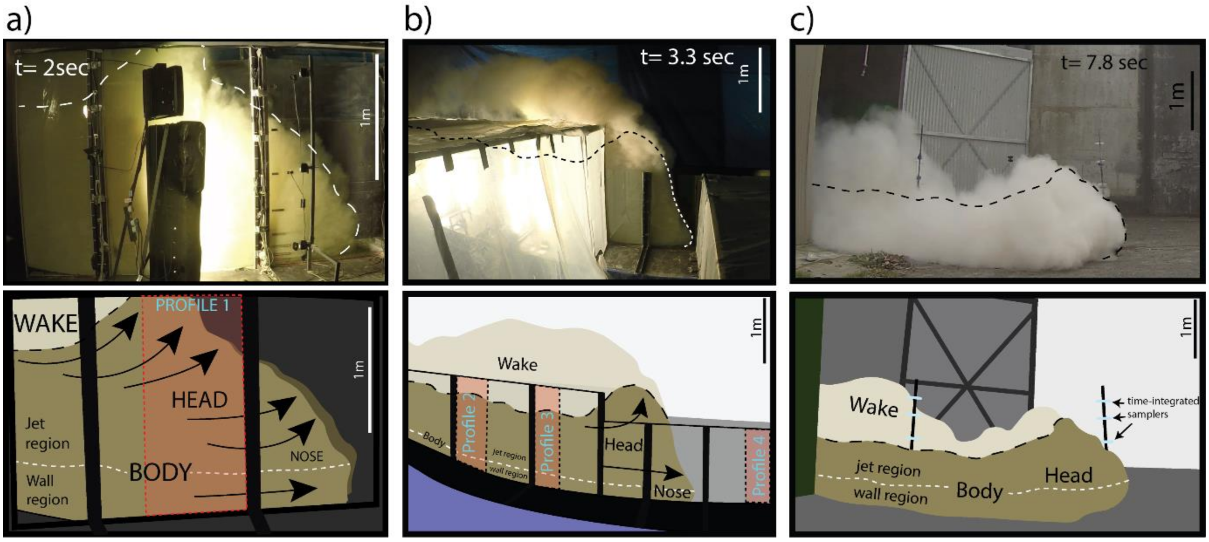

Figure 3-1 : Lateral views and schematic sketches of the synthesised dilute PDC at different flow times after channel impact. Top panels- Lateral camera views of the flow (flow body is outlined in dashed lines) at different locations during channel-confined (a-b) and unconfined (c) propagation. Bottom panels - Schematic sketches of the flow highlighting the body and head, body-wake boundary (wide dashed lines), and wall-jet region boundary (dashed white line, region where the velocity is at a maximum and shear is minimum). Red rectangles mark the locations of static observer profiles (1-4) and sensor/sampler location

The position and velocity of the flow front as a function of time are shown for both experiments in Figure 3-2 show general decelerating behaviour. The initial flow front velocities of the two experiments differ only slightly where, immediately after impact, the smooth experiment and rough experiment flows acquired velocities of c. 6.1 and 5.5 m s^{-1}, respectively. The smooth experiment flow followed an overall constantly decreasing flow front velocity trend as the flow propagated down the channel (red dashed line, Figure 3-2 a), while the rough experiment flow displayed a period of acceleration starting at 3.2 s until c. 7 s after impact (blue solid line, Figure 3-2 a). Conversely, the smooth experiment flow remained in a phase of constant deceleration. Although the rough experiment flow was initially slower than the smooth experiment flow, for both experimental flows the flow front positions eventually converged towards the final runout distances.

Throughout the runout, both the rough and smooth experiments flows experienced significant deceleration, with velocities of c. 1.87 and 1.64 m s^{-1} at half the runout time (6 s), further decreasing to only several decimetres per second slightly before 11 s of runout time. At c.11 s of runout time, both flows, at the same runout distance (c. 24 m) achieves buoyancy reversal and lifts-off the flow surface (Figure 3-2 b).

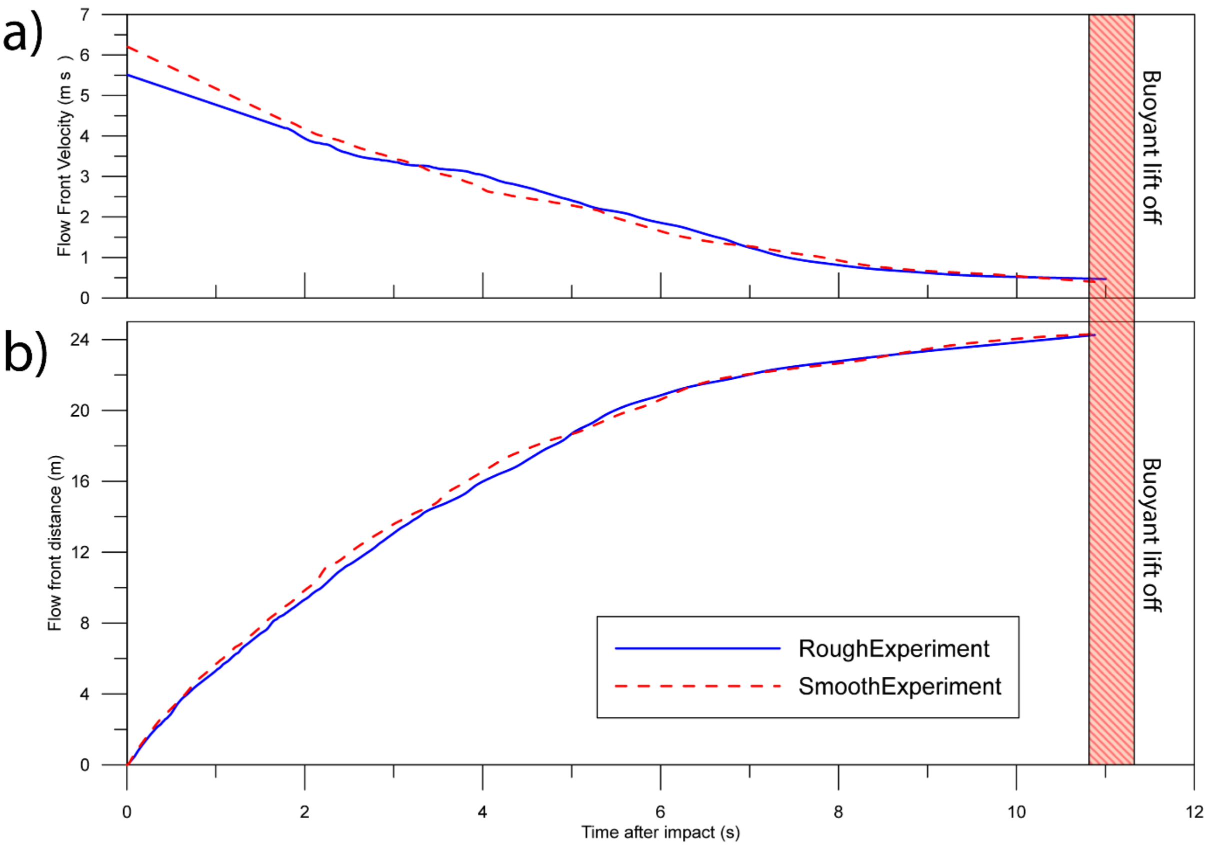

Figure 3-2 : Flow-front position and velocity as a function of time after impact. a) Flow front velocities of the rough experiment (blue solid line) and smooth experiment (red dashed line) flows. b) Flow front position for the rough experiment (blue solid line) and smooth experiment (red dashed line) flows. In general, both flows gradually decrease in flow front propagation velocity as a function of distance and time from impact and display a comparable trend. The smooth experiment flow exhibits a slightly faster initial flow front velocity of c. 6.1 m s^{-1}, but decelerates gradually during runout. The rough experiment flow displays a slightly slower initial velocity of 5.5 m s^{-1}, followed by a gradual decrease until c. 3.2s from where the flow mantains a slightly higher velocity than the smooth experiment flow for c. 4 s. In distal reaches, both flows lost momentum due to flow expansion from entraining ambient gas and ongoing sedimentation processes, which led to flow stalling and buoyant lift-off (shaded red).

The deposit emplacement by the rough and smooth experiments flows was concluded after c. 12 s. After the flows ceased to propagate, particles suspended in the buoyant ash cloud required several tens of seconds to slowly settle out of suspension onto the deposit surface. Both the rough and smooth experiment flows produced comparable deposit thickness distributions (Figure 3-3 a-b) up to 25 m runout distance, which is the region where the flows stopped propagating and buoyant lift-off commenced. Most of the deposit mass (80%) was emplaced within the first 2.5 m runout distance. The thickest deposit occurred at c. 1 m from impact location, with a maximum thickness of c. 0.2m. This is the region where a regressive dune structure has been emplaced.

Deposit thickness decreases exponentially (Figure 3-3 a-b) in both experiments. Both experiment flows emplaced a similarly thick deposit. The thickness decays in the two experiments slightly deviate from each other from c. 12 m runout distance onwards. This coincides with the location of a break in slope (transition from inclined to flat runout) occurring at 11.7 m and the decrease in height of the channel walls from 1.2m to 0.6m. Furthermore, the change from confined to unconfined runout (at 15.7 m, vertical black line, Figure 3-3 a-b) is visible as a decrease in the deposit thickness of both experimental runs, with overall higher deposit thicknesses and deposited mass for the smooth experiment.

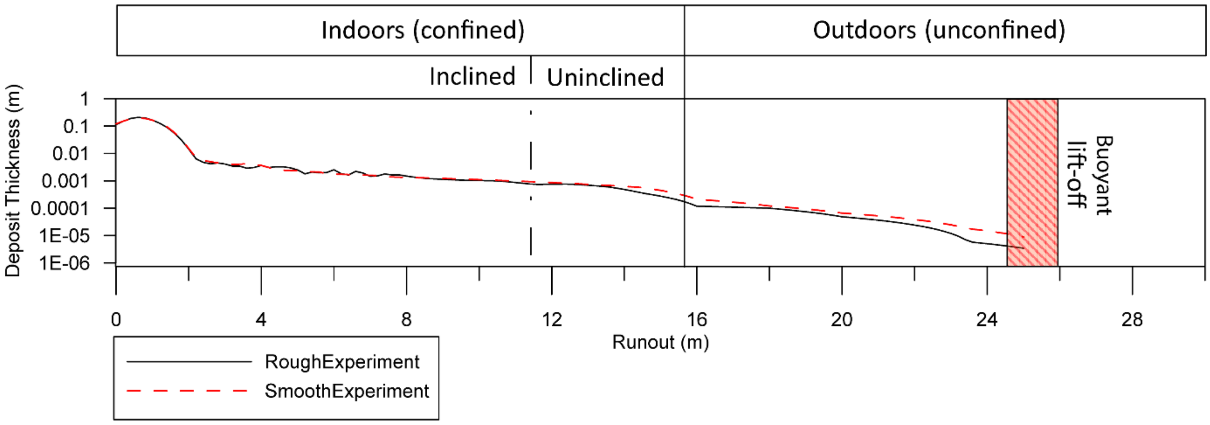

Figure 3-3: Proximal and distal deposit characteristics from the rough and smooth experiments flows. Rough experiment (solid black line) and smooth experiment (red dashed line) deposit thickness distributions up to 25 m runout distance. In both cases, most of the deposited mass is concentrated within the first 2.5 m runout distance. After that, deposit thicknesses and mass per area distributions are very comparable until c. 9 m, from where the smooth experiment flow (red dashed line) produced a slightly thicker deposit (less than one order of magnitude) compared to the rough experiment flow. This shift coincides which a change from inclined to flat runout (dash-dotted line) at c. 11.5 m distance from impact. To note is also a change in both the rough and smooth experiments flow deposit thickness after the change from confined to unconfined runout, where the flow can laterally expand during the final stage of propagation.

Figure 3-4 illustrates the shapes of the evolving experimental PDCs and the shapes of the aggrading deposit at three different times. Over time, the current deposited outwards and upwards progressively. At 0.5 s after impact with the channel, where the flow had reached approximately 3 m runout distance, the current had already deposited 12.6% of the final deposit volume regardless of the substrate roughness. At 4 s, where both flows reached a comparable runout distance of c. 17 m, the flow had deposited close to 95% of their final deposit volume. Just before partial buoyancy, the flow at 8 s had deposited 99.6% of their final deposit volume.

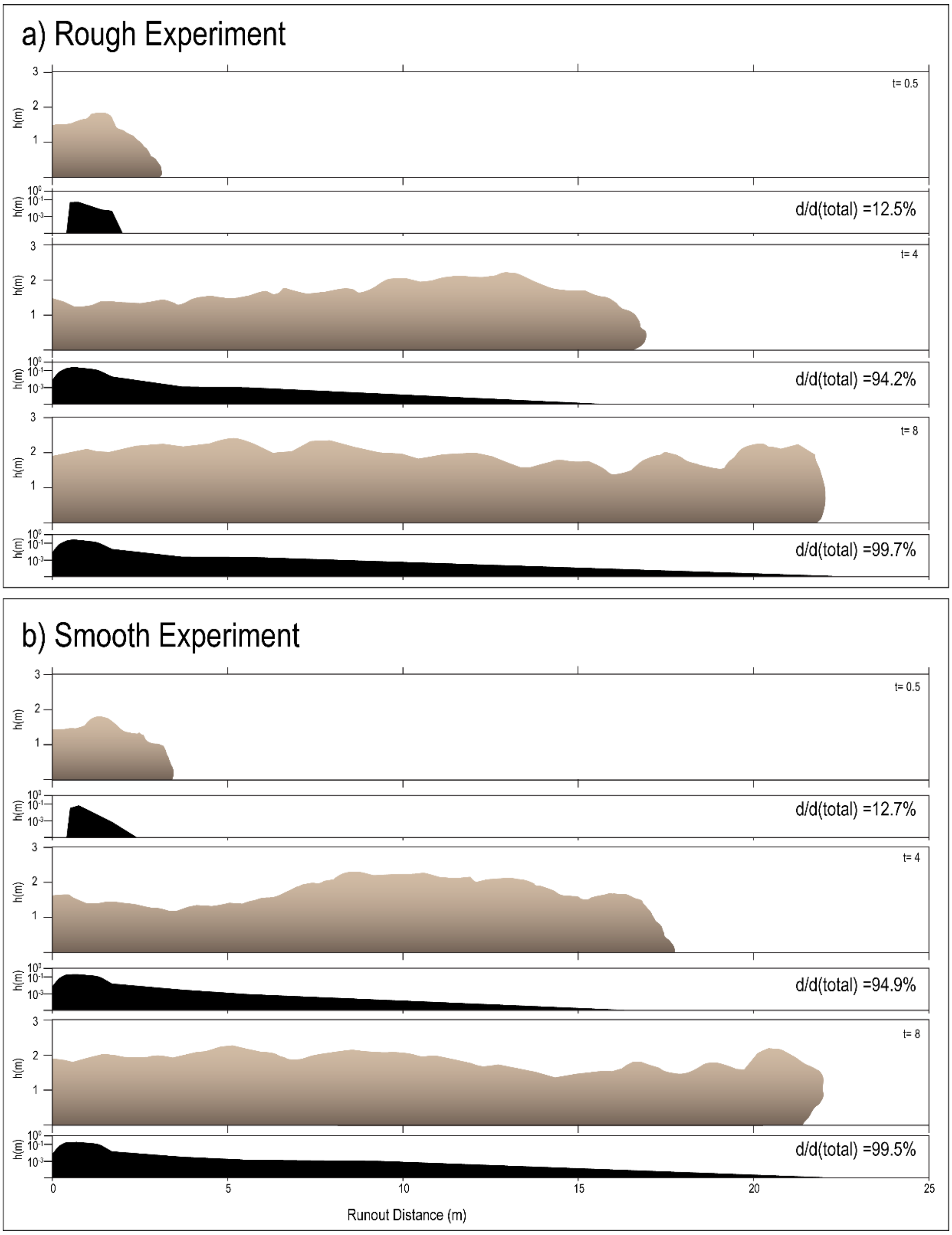

Figure 3-4: Two-dimensional flow geometry (including wake and buoyant ash cloud) evolution and deposit extent of the two synthesised dilute PDC at selected time (t) after impact. Growth in flow volume is attributed to constant entrainment of ambient air. Deposit thickness (h) is plotted in a log scale for better visualisation. At each time step the ratio between currently deposit volume (d) and final deposit volume (d(total)) is reported. Flows synthesised on different substrate roughness do not display major differences in deposition rate. At 4s after impact, both flows deposited c. 95% of their final deposit volume. At 8s after impact, the smooth experiment flow started to partially lift off at a runout length of 23 m.

Similar to real world PDCs, the experimental PDCs are characterised by a strong vertical density stratification. This density stratification is associated with a marked gradation of the size of particles suspended in the flow. Figure 3-5 depicts height-distance contour plots of the median grainsize diameter (d_{50}) of the two experimental currents at three different times.

The evolution of the vertical flow grainsize gradation is relatively similar in both experiments. However, in Figure 3-5 at the same times and elevations the rough experiment flow carries slightly coarser particles than the gravity current propagating over the hydraulically smooth surface.

In general, the median diameter strongly decreases as a function of height and distance during flow propagation, as visualised by isolines of constant median grain size diameter. Furthermore, the isolines of the median grain size diameter are not always orientated slope parallel but are also orientated both in a downstream and or upward direction downslope. Additionally, isolines were identified to terminate at the flow base as a function of distance.

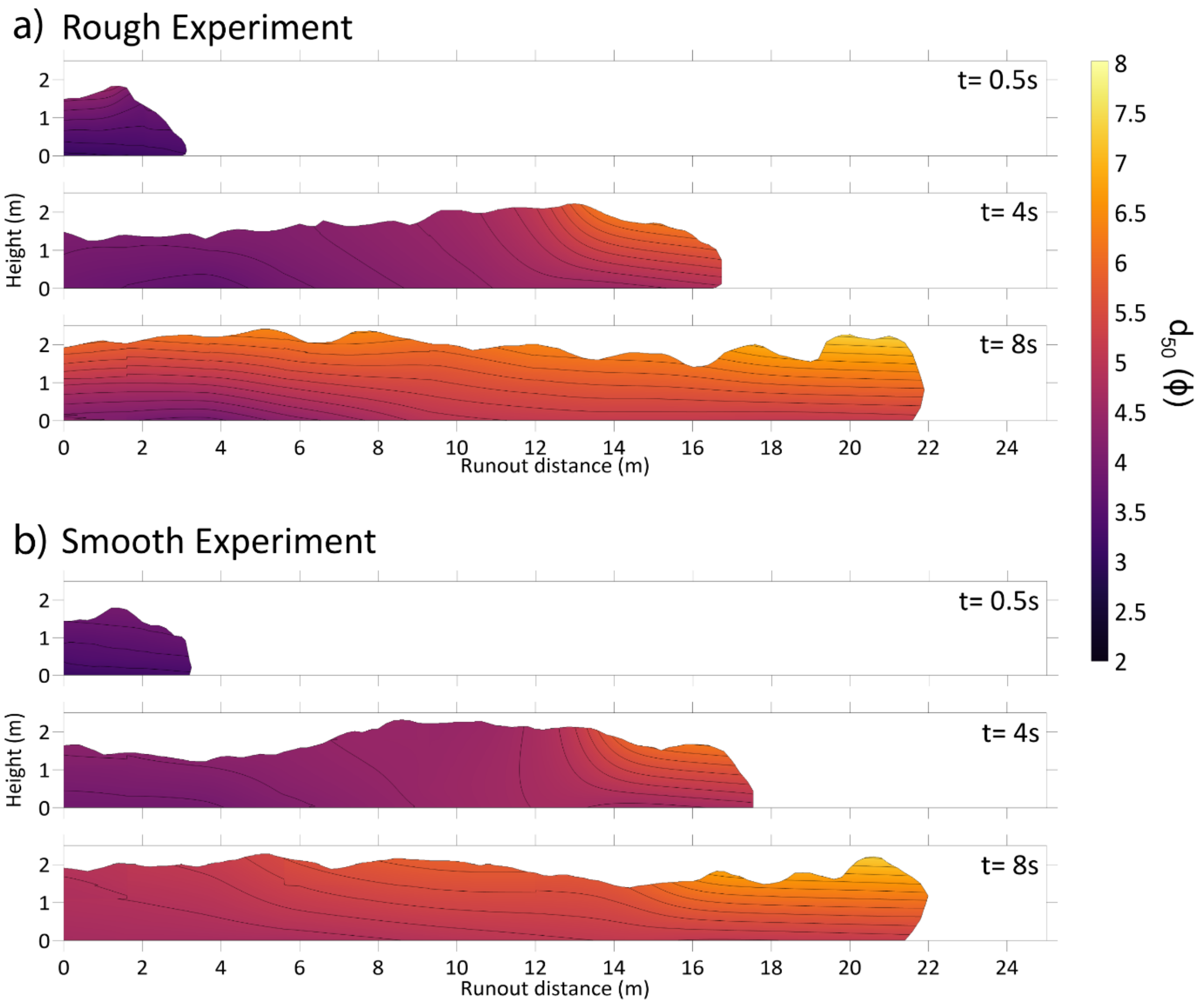

Figure 3-5: Height-distance contour plots of median grain size (d_{50}) at three different times after impact for both the rough (a) and smooth (b) experiments flows. Vertical distributions of median grainsize are a proxy for vertical stratification, where median grainsizes decrease as a function of height. Median grainsizes are calculated following Inman (1952). The black lines are isolines of constant median grainsize diameter.

3.2 Spatio-temporal depositional processes

This section (3.2.A) introduces the non-genetic lithofacies identified from the final deposits of the two experimental flows at four observer locations. Moreover, this section (3.2.B) will also introduce the sediment transport mechanisms observed to occur at the lower flow regions of the experimental flow.

3.2.A Types of depositional facies emplaced by the experimental dilute PDCs

Deposits by both the rough and smooth experiments flows display a wide range of sedimentary structures and features. To better understand the dynamics and lateral evolution of sediment deposition and erosion within these dilute PDCs, non-genetic lithofacies were identified and assigned to unit packages (Figure 3-6). Descriptions of these lithofacies were based on classifications by Branney and Kokelaar (2002).

The identified lithofacies in both the rough and smooth experiments deposits can be categorized based on the structure of the units and fall into two main categories massive and stratified lithofacies. Lithofacies can be further subdivided according to the present dominant grainsize into lapilli ash (LT) or ash(T) massive lithofacies: mLT and mT, respectively. Lithofacies identified in this study is outlined in the table below (Table 3-1). A non-structured lapilli lithofacies was also observed (Figure 3-6 c).

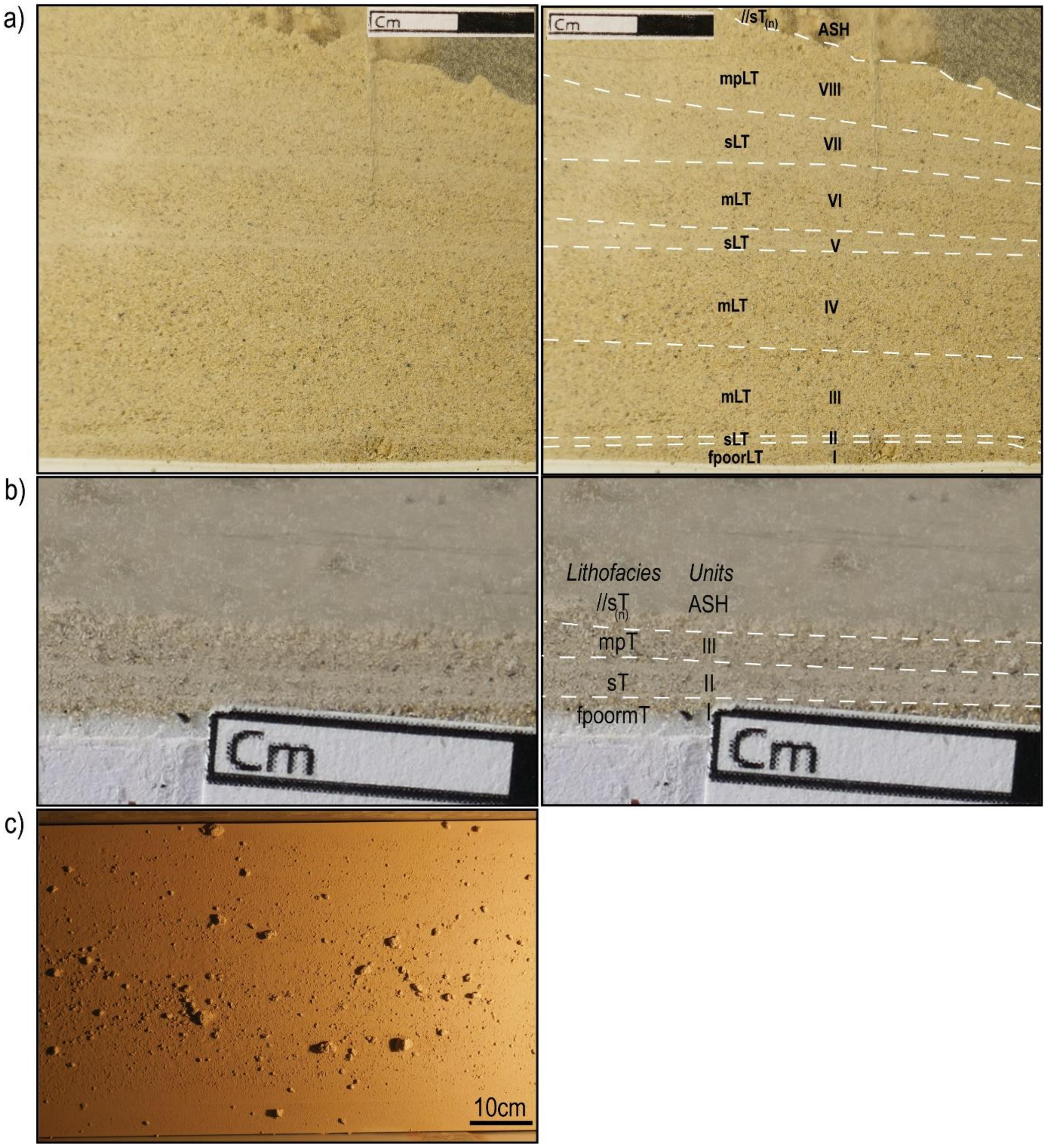

Figure 3-6: Close-up images of the rough experiment experimental deposits and assigned nongenetic lithofacies, following definitions by (Branney & Kokelaar, 2002). a) Left panel - Closeup image of the deposit taken at 1.6 m (profile 1 location) from impact. Right panel- Annotated image outlining unit boundaries and their assigned nongenetic lithofacies. b) Closeup image (left) and annotated image (right) of the deposit from the rough experiment deposit at 3.7m (profile 2 location) runout distance. C) Top-down picture taken of the deposit surface at c. 7m show the individual lapilli clasts found across the deposit surface until c.20m runout distance.

Table 3-1: Summarized descriptions of lithofacies observed in the deposits of the experimental flows.

Structure	**Grainsize**	**Lithofacies**	**Description**	**Additional features**
Massive	Lapilli-Ash	mLT	Massive and poorly sorted. Grainsizes range from fine ash to medium lapilli. The mLT units are characteristically thick, with thickness ranging from c. 0.2-1.5 cm. Bottom contact is characteristically sharp.	May be normally graded (mLT(n)) and contain faint internal stratifications.
		fpoormLT	Massive and poorly sorted. Clast-supported. Grainsizes range from fine ash to medium lapilli.	
		mpLT	Massive and poorly sorted. Pumice rich and slightly reverse graded. Grainsizes range from fine ash to medium lapilli.	Usually found at the top half of the depositional sequence
	Ash	mT	Massive and poorly sorted. Grainsizes range from fine to very coarse ash. The mT units thickness ranges from c. 0.06-0.1 cm. Bottom contact are characteristically sharp.	
		fpoormT	Massive and poorly sorted. Clast-supported. Grainsizes range from fine to very coarse ash.	
		mpT	Massive and poorly sorted. Pumice rich and slightly reverse graded. Grainsizes range from fine to very coarse ash.	Usually found at the top half of the depositional sequence
Stratified	Lapilli-Ash	sLT	Stratified beds comprising fine ash to fine lapilli grainsizes. Beds alternate between fine and coarser beds. Horizontally stratified beds, with bedding slightly dipping in the downstream direction. Thickness ranges from c. 0.1 to c. 0.5 cm. Bottom contact is. characteristically erosive and unconformable	
	Ash	sT	Stratified beds comprising very fine to coarse ash grainsizes. Beds alternate between fine and coarser beds. Horizontally stratified beds, with bedding slightly dipping in the downstream direction. The thickness ranges from c. 0.02 to c. 0.1 cm. Bottom contact is characteristically erosive and unconformable	
		//sT	Stratified beds comprising very fine to medium ash grainsizes. Alternating sequence of fine and coarser beds. Horizontally stratified beds, with bedding slightly dipping in the downstream direction.	Normally graded variant (//sT(n)) is characterised by very fine to fine grainsizes and a graded bottom contact.
N/A	Lapilli	Lapilli	Individual lapilli clasts that sit by themselves on top of the deposit surface	

3.2.B Gas-particle transport in the lower wall and bedload region

The lower flow region of the experimental dilute PDCs is subdivided (from deposit surface upwards) into: a) a bedload region characterised by strong changes in sediment transport mechanisms, low degrees of turbulence and particle concentrations in the range from 0.5 to several vol%; b) a transient region, characterised by impacting mesoscale clusters from the fully turbulent flow above, presence of saltating lapilli, and overall particle concentrations in the range from 0.1 to 1.5 vol.%; c) the fully turbulent flow above, where, within the lower most third of the flow (lower jet region and wall region) mesoscale clusters form and impact into the transient region below (Brosch and Lube, 2020).

Particle transport mechanisms within the lower most flow regions are dynamic and constantly evolving throughout flow propagation. Following Brosch and Lube (2020), sediment transport mechanisms in the bedload region are distinguished and summarized in the table below (Table 3-2).

Table 3-2: Summarized sediment transport mechanisms observed in the lower flow region of the experimental flow. The occurrences of the sediment transport mechanisms at which profiles (1 (1.6m), 2 (3.7m), 3 (5.6m), 4 (9.3m)) are also reported.

Sediment transport mechanism	**Description**	**Occurrences (profiles)**
Rolling and saltating	Coarse ash and lapilli sized particles transported through saltation and rolling.	1, 2, 3, 4
Shifting sandwaves	Short-lived mobile granular flows in the bedload region.	1
Tractional Bedload and rolling and saltating	Concentrated bedload region, associated with the formation of fast settling mesoscale cluster. Particles are observed to occasionally be ejected into the transient region due to particle-particle and particle-substrate collisions.	1, 2, 3, 4
Rolling and low traction aggradation	At low flow velocities (c. 2 m s-1), bedload region is transported through low velocity tractional transport. Concurrently, the occurrence of a transient region and formation of mesoscale clusters ceases.	1, 2, 3, 4
Falling out of suspension	Finer grained particles settling out of suspension as flow velocities fall under c. 2 m s-1.	1, 2, 3, 4

Figure 3-7 shows the observed sedimentation transport mechanism that occurs along the bedload (dashed black lines, Figure 3-7) of the rough experiment flow at the runout distance of 1.6m. As the flow passes the proximal observer location, the complete range of sedimentation transport mechanism described in Table 3-2 can be observed. Initially, at 0.23s (t=0.23s, Figure 3-7) after flow arrival, the flow displays rolling and saltating sediment transport mechanism. As the rear of the head passes at c. 1.12s (t=1.12 Figure 3-7), shifting sandwave transportation can be observed to occur concurrently with the formation of mesoscale clusters (red arrows, Figure 3-7). The passage of the body at 1.45s (t=1.45s, Figure 3-7) after flow arrival is characterised by the tractional bedload transportation mechanism along with further formation of mesoscale clusters. The settling of the mesoscale cluster during shifting sandwave and tractional bedload transportation in the lower flow regions is characterised by the formation of the transient region (dotted black lines, Figure 3-7). The passage of the distal body at 3.1s (t=3.1s, Figure 3-7) after flow arrival is characterised by rolling and low tractional sediment transport mechanism in the lower flow region. At the distal body, the cessation of mesoscale cluster formation coincides with the disappearance of the transient region. The passage of the tail at 3.53s (t=3.53s, Figure 3-7) after flow arrival is characterised by low flow velocities (average of <2 m s^{-1}) and sediment transport mechanism of slow settling out of suspension.

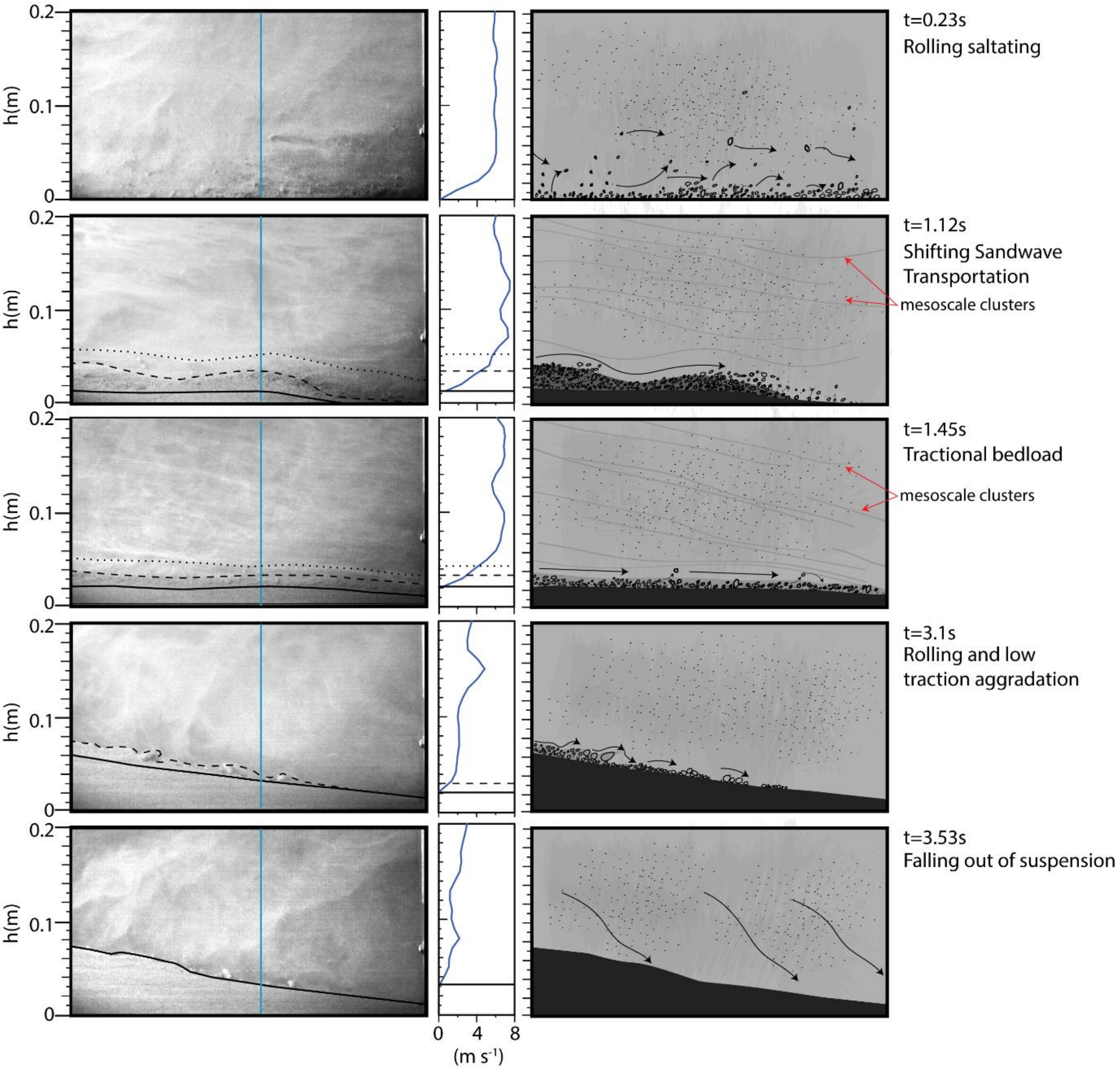

Figure 3-7: Sediment transport and deposition of the rough experiment flow at the proximal most profile 1 (1.6 m). High-speed video still images and corresponding illustrations of the lower 0.2m of the experimental dilute PDC at 5 separate times (t= seconds) are displayed. Above the deposit surface (still image: outlined by solid black line; annotated sketch: dark black colour), the lower flow region can be divided into the bedload region (still image: outlined by dashed black line; annotated sketch: dark grey shade) and transient region (still image: outlined by the dotted black line). The bedload region is characterised by strong changes in sediment transport mechanisms (rolling and saltating, shifting sandwaves, tractional bedload, low traction aggradation), while the transient region is marked by the accumulation of fast settling mesoscale clusters. Changes in horizontal velocity profiles (blue) reflect the dynamic nature of the bedload, transient and fully turbulent flow regions above the deposit during flow propagation.

3.2.C Local time-variant deposition

(i) Local depositional sequences

The following section will present stratigraphic columns of the final deposit from the rough and smooth experiments flow from four profile locations. Units identified in each profile location from both flows have also been assigned a non-genetic lithofacies. Dominant sediment transport mechanism observed during unit emplacement is also reported. Limited thickness of the deposit at profile 4 of the rough experiment, did not allow for deposit analysis.

C.I. <u>Rough Experiment</u>

(i) Profile 1

The first depositional unit I (Figure 3-8) emplaced is a fines-depleted, coarse ash to fine lapilli massive bed (fpoorLT). During the deposition of this first unit, the dominating sediment transport mechanism in the lower flow region is coarse particle to particle collisions and associated rolling, sliding and saltating of coarse particles. Emplacement of the first unit occurs rapidly at a timescale of c. 0.2 s. Immediately after emplacement of the first depositional unit, the development of a more coherent bedload within the lower flow region coincides with the deposition of the next depositional unit II (Figure 3-8). Sediment transport mechanisms shift from rolling, sliding, and saltating of individual coarse particles to particles being transported within a more developed tractional bedload. After c. 0.4 s of flow propagation, the developed tractional bedload in the lower flow region deposits a sLT lithofacies with an erosive base contact with the underlying fpoormLT lithofacies.

The emplacement of the sLT lithofacies is short lived, as immediately after 120ms of tractional bedload deposition, the arrival of a highly mobile granular sand wave interrupts the deposition of unit II (sLT) (Figure 3-8). The cessation of a single wave of the highly mobile granular deposits a very thick (0.89 cm), poorly sorted, coarse ash to fine lapilli unit III (mLT lithofacies) in 'en masse' (Figure 3-8). Within this unit III, very faint ash stratification can be observed. The contact between unit III and the underlying unit II is sharp. The arrival of a second sandwave at 0.92s after flow arrival, deposits another very thick (c. 1.1 cm), poorly sorted, coarse ash to fine lapilli unit IV (mLT lithofacies, Figure 3-8). Contact between the two mLT units (III and IV) is gradational. After the deposition unit IV through the second set of sandwaves at 1.32s, the dominant sediment transport mechanism within the lower flow region shifts back to tractional bedload.

The deposition of a subsequent stratified lapilli ash unit V (sLT lithofacies) by tractional bedload mechanism is initiated at 1.32 s after flow arrival. After c. 0.5s of tractional bedload deposition, the 0.18 cm thick unit V is interrupted by the arrival of sediment influx in the form of a highly mobile granular shifting sandwave. The third and final set of shifting sandwaves starts depositing at 1.72s after flow arrival. The deposited unit VI (mLT lithofacies) features an internal structure equivalent to the underlying units deposited by prior shifting sandwave events. However, the thickness of unit VI (0.7 cm) is less than the previous mLT units (0.89 and 1.1 cm, respectively). Sediment transport mechanism in the lower flow region reverts to tractional bedload deposition at 2.26 s after flow arrival. Tractional bedload deposition persists up to c. 2.74 s after flow arrival, slowly aggrading the c. 0.5 cm thick unit VII (sLT lithofacies), marked by an erosive contact with the underlying unit VI. Unit VII consists of alternating finer (fine to coarse ash) and coarser (moderate to fine lapilli) beds. The cessation of the deposition of unit VII occurs at 2.74 s after flow arrival.

Deposition of unit VIII occurs at 2.74 s after flow arrival. This massive, poorly sorted, pumice-rich, fine ash to moderate lapilli unit (mpLT, Figure 3-8) is deposited through low traction aggradation. Unit VIII is characterised by a sharp, slightly graded contact to the lower unit VII. Immediately after the deposition of unit VIII at 3.54s after flow arrival, dusting by individual lapilli clasts sparsely cover the deposit surface. Simultaneously, slow settling of very fine to fine ash over the course of seconds to several tens of seconds after flow passage, generates a final ASH unit that mantles the entire deposit surface. This ash cover bed (//sT$_{(n)}$ lithofacies, Figure 3-8) is normally graded and laminated and marks the termination of the depositional sequence at this profile.

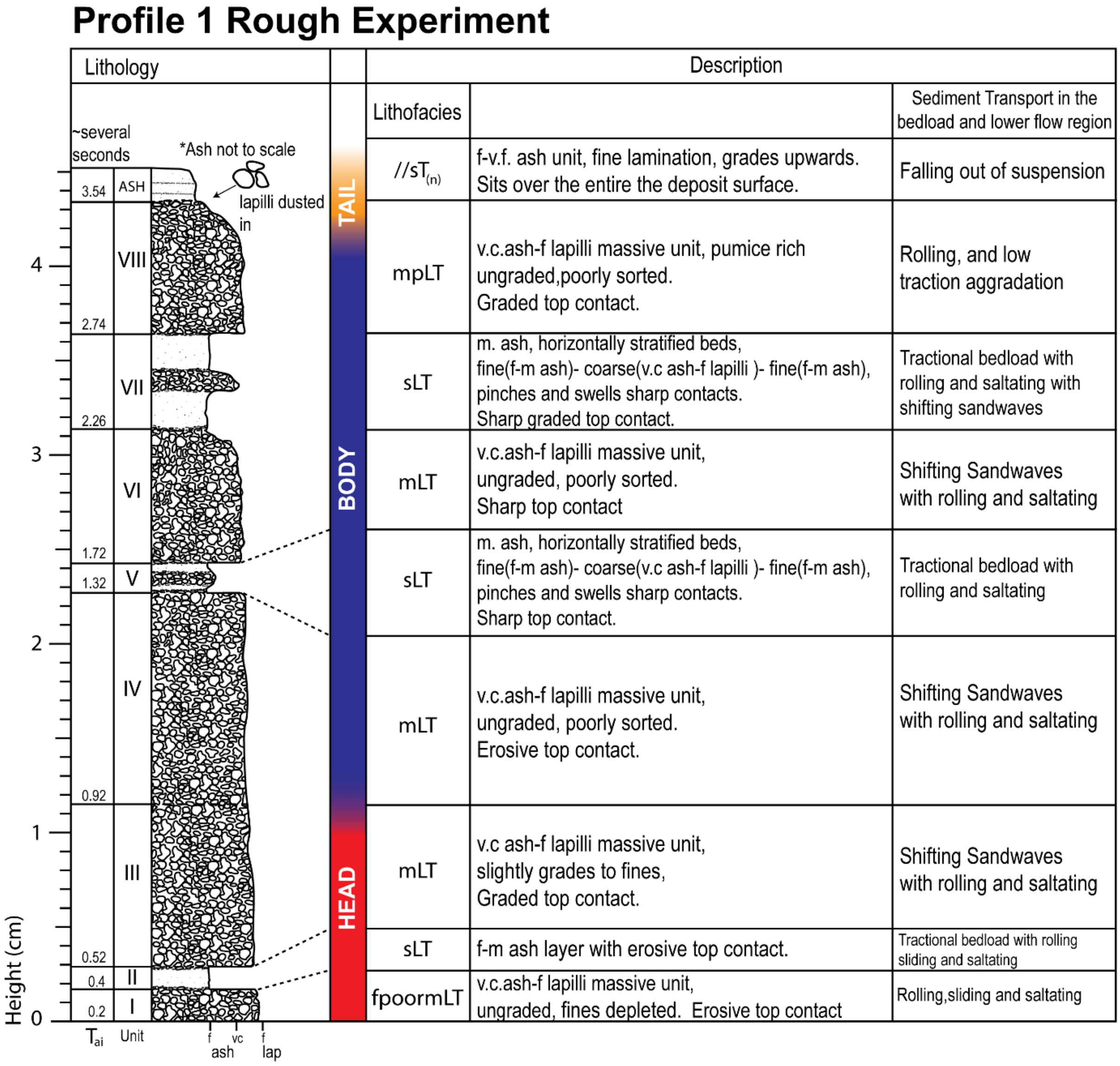

Profile 1 Rough Experiment

Description		
Lithofacies		Sediment Transport in the bedload and lower flow region
$//sT_{(n)}$	f-v.f. ash unit, fine lamination, grades upwards. Sits over the entire the deposit surface.	Falling out of suspension
mpLT	v.c.ash-f lapilli massive unit, pumice rich ungraded,poorly sorted. Graded top contact.	Rolling, and low traction aggradation
sLT	m. ash, horizontally stratified beds, fine(f-m ash)- coarse(v.c ash-f lapilli)- fine(f-m ash), pinches and swells sharp contacts. Sharp graded top contact.	Tractional bedload with rolling and saltating with shifting sandwaves
mLT	v.c.ash-f lapilli massive unit, ungraded, poorly sorted. Sharp top contact	Shifting Sandwaves with rolling and saltating
sLT	m. ash, horizontally stratified beds, fine(f-m ash)- coarse(v.c ash-f lapilli)- fine(f-m ash), pinches and swells sharp contacts. Sharp top contact.	Tractional bedload with rolling and saltating
mLT	v.c.ash-f lapilli massive unit, ungraded, poorly sorted. Erosive top contact.	Shifting Sandwaves with rolling and saltating
mLT	v.c ash-f lapilli massive unit, slightly grades to fines, Graded top contact.	Shifting Sandwaves with rolling and saltating
sLT	f-m ash layer with erosive top contact.	Tractional bedload with rolling sliding and saltating
fpoormLT	v.c.ash-f lapilli massive unit, ungraded, fines depleted. Erosive top contact	Rolling,sliding and saltating

Figure 3-8: Stratigraphical column of the deposit of the rough experiment flow at the most proximal static observer profile 1 (1.6m runout distance). Thicknesses and units belonging to the 4.48cm thick deposit are drawn to scale, except for the final ASH unit. The time stamp of each unit boundary is after flow arrival (T_{ai}). Non-genetic stratigraphical lithofacies, sediment transport mechanisms and the relevant flow structure are reported for each emplaced unit.

(ii) Profile 2

Deposit formation at static observer profile 2 (runout distance of 3.7m) starts 0.3s after flow arrival. Initially, the flow is non-depositional for the first 0.3 s of flow passage, after which a tractional bedload is generated that initiates deposition. This leads to the generation of a 0.04cm thick, massive, fines-depleted, coarse to very coarse ash unit I (fpoormT lithofacies, Figure 3-9) in 0.48 s. The bulk of unit I is rapidly deposited in the first c. 0.2 s of unit I aggradation (Figure 3-9). Immediately after deposition of unit I, at 0.78 s after flow arrival, a period of no net deposition occurs (marked as unconformity in Figure 3-9). The flow passage between 0.78 and 1.5 s after flow arrival, is marked by a non-depositional period, where beds are being deposited and eroded at a constant rate. This non-depositional phase is characterized by an unconformity between unit I and the subsequently deposited unit II.

The passage of the flow at 1.5s after flow coincides with a period of intense mesoscale cluster formation, which rapidly feeds the tractional bedload. At c. 1.5 s, the deposition of unit II begins. Unit II is made up of sets of stratified ash beds (sT lithofacies, Figure 3-9) with alternating coarse and fine ash beds. Alternating stratified beds are not laterally continuous and are characterised by a ‘pinching and swelling’. Stratified beds within unit II feature sharp contacts between each other and are slightly dipped in downstream direction. The emplacement of these stratified beds of unit II terminates due to another period (2.08 to 3.14s after flow arrival, Figure 3-9) of no net deposition.

At 3.14s after flow arrival, there is a shift in the dominant sediment transport mechanism, which is characterised by low tractional deposition, and rolling of individual coarse clasts, this leads to the emplacement of unit III. Unit III is deposited as a massive, poorly sorted, pumice rich, ash unit (mpT lithofacies, Figure 3-9). After unit III emplacement terminated at c. 3.82s after flow arrival, dusting of individual lapilli sized clasts covers the deposit surface. Concurrently and up to several tens of seconds thereafter, fine ash slowly settles, generating a finely laminated, graded, very fine to fine ash unit (ASH unit) is emplaced. The resultant ash cover unit (//$sT_{(n)}$, Figure 3-9) covers the entire deposit surface with a sharp, slightly gradational contact. The deposition of the final ash unit marks the termination of the depositional sequence at this profile location.

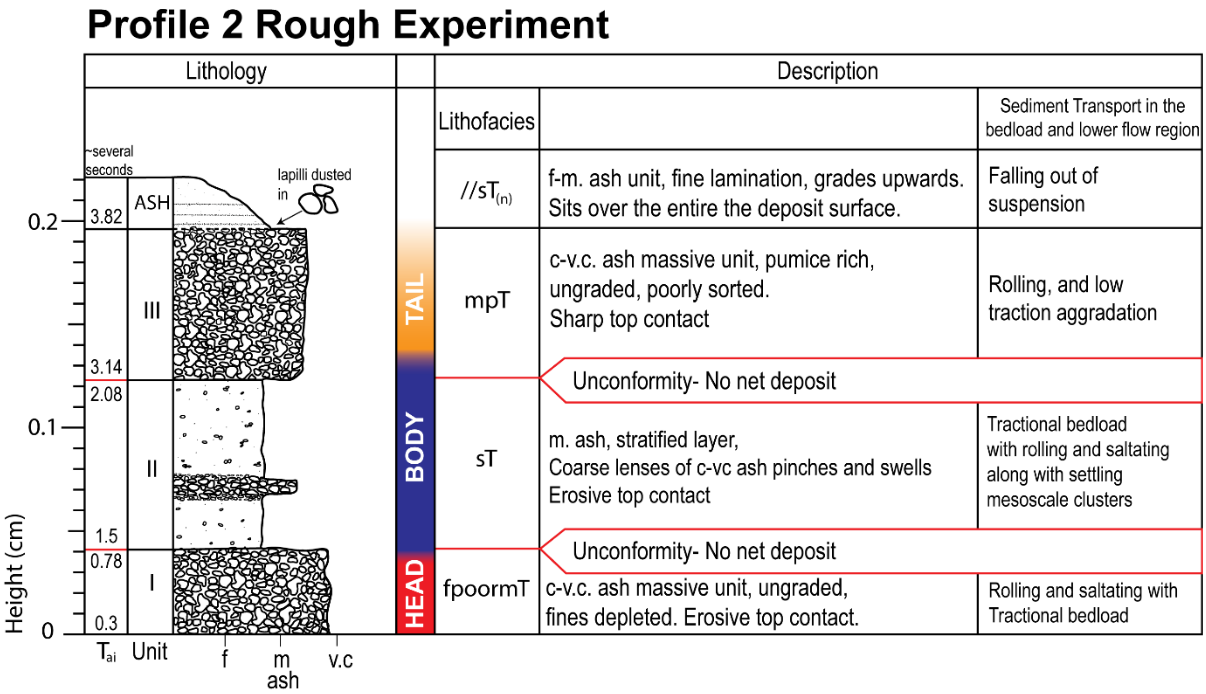

Figure 3-9: Stratigraphical column of the deposit of the rough experiment flow at the static observer profile 2 (3.7m runout distance). Thicknesses and units belonging to the 0.221 cm thick deposit are drawn to scale. The time stamp of each unit boundary is after flow arrival (T_{ai}). Unconformable boundaries (red unit boundaries) represent periods of n.n.d during flow passage. Non-genetic stratigraphical lithofacies, sediment transport mechanisms and the relevant flow structure are reported for each emplaced unit.

(iii) Profile 3

At the observer profile 3 (located at runout distance of 5.6 m) deposition starts after an initial period of non-deposition. The emplacement of a 0.056 cm thick unit I occurs at 0.24 s after flow arrival where the bulk of unit I is rapidly deposited during the first c. 0.2 s of unit aggradation (Figure 3-10). Unit I is massive, fines-depleted, composed of coarse to very coarse ash (fpoormT lithofacies). Unit I emplacement terminates at c. 0.7s after flow arrival, when sediment transport in the lower flow region becomes predominantly erosive. This erosive period lasts from c. 0.7 to 1.16s after flow arrival and leads to the generation of an erosive unconformity in the depositional record (unconformity marked in red, Figure 3-10).

After this period of erosion, net deposit formation resumes at c. 1.16s after flow arrival. The flow emplaces a 0.078 cm thick, very fine to fine ash, laminated unit II (//sT lithofacies, Figure 3-10), gently dipping in the downstream direction. The passage of the flow at unit II deposition is marked by the formation of fast settling mesoscale clusters which merge into the transient region, feeding the tractional bedload. Unit II sits on an unconformable erosive bottom contact with unit I. Cessation of unit II is associated with the deposition of a massive, 0.064cm thick, poorly sorted coarse to very coarse ash unit III (mT, Figure 3-10) at 2.6 s after flow arrival. During unit III emplacement, sediment transport mechanisms shift to low traction aggradation, and simultaneous occurrence of rolling individual medium to fine lapilli clasts.

The emplacement of unit III terminates at 3.34 s after flow. Over the course of several tens of seconds, the very fine to fine ash particles slowly settle out of suspension, leading to the generation of a final fine ash unit (//sT$_{(n)}$ lithofacies, Figure 3-10). This ash unit is normally graded and displays fine internal laminations and marks the termination of the depositional sequence at this profile.

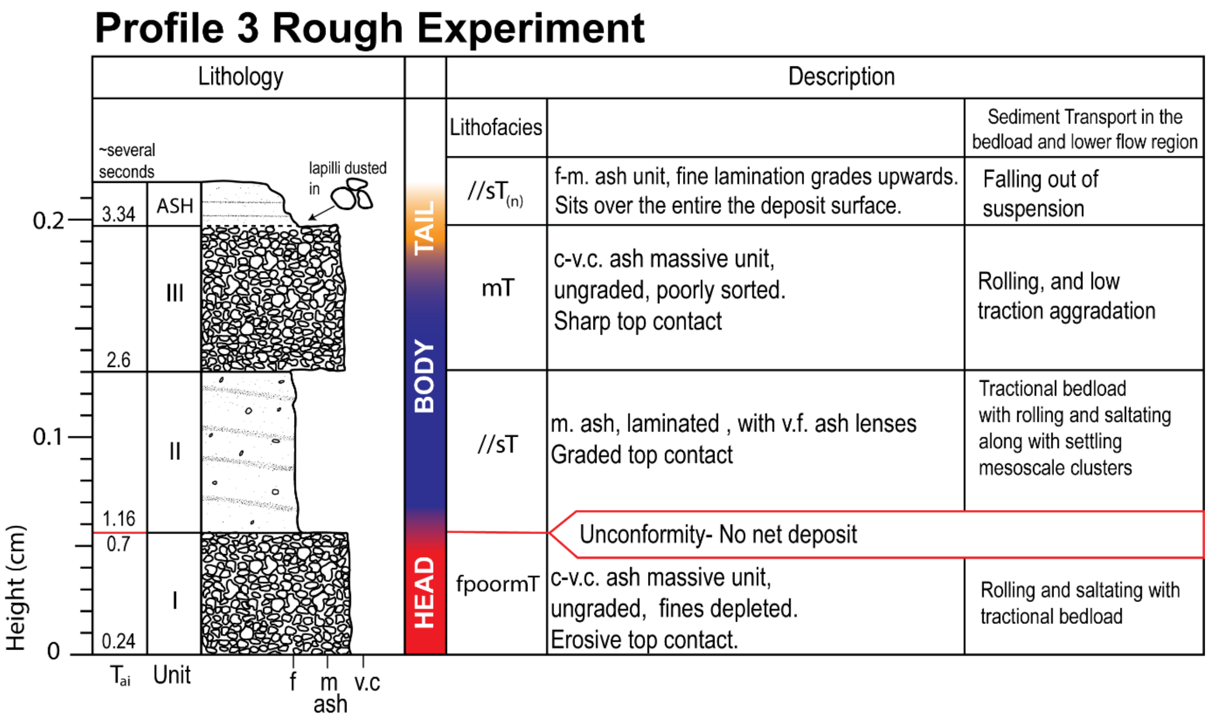

Figure 3-10: Stratigraphical column of the deposit of the rough experiment flow at the static observer profile 3 (5.6 m runout distance). Thicknesses and units belonging to the 0.216 cm thick deposit are drawn to scale. The time stamp of each unit boundary is after flow arrival (T_{ai}). Unconformable boundaries (red unit boundaries) represent periods of n.n.d during flow passage. Non-genetic stratigraphical lithofacies, sediment transport mechanisms and the relevant flow structure are reported for each emplaced unit.

C.II. Smooth Experiment

(i) Profile 1

At the observer profile 1 (located at 1.6m runout distance), the initial 0.18 s after flow arrival is non-depositional. Deposition of the first unit I (Figure 3-11) occurred at 0.18 s after flow arrival, and sediment transport mechanism in the lower flow region is characterized by rolling, sliding and saltating mechanisms. This c. 0.114 cm thick, very coarse to fine lapilli thick unit I is massive, and fines depleted (fpoormLT lithofacies, Figure 3-11). Unit I emplacement stops at c. 0.48 s after flow arrival, before the development of a distinct bedload in the lower flow region.

The generation of the tractional bedload region initiates deposition of unit II. Unit II is a c. 0.07 cm thick, stratified lapilli-ash unit (sLT lithofacies, Figure 3-11) and is emplaced through tractional bedload aggradation in the lower flow region from 0.48 to 0.6 s after flow arrival. Deposition of unit II is interrupted by the arrival of a highly mobile granular shifting sandwave at c. 0.6s after flow arrival.

The cessation of a single wave of the highly mobile, granular shifting sandwaves at 1 s after flow arrival deposits a very thick (c. 1.4 cm), poorly sorted, coarse ash to fine lapilli unit III ($mLT_{(n)}$ lithofacies) in 'en masse'. The final c. 0.1 s of unit III deposition is characterised by a period of tractional bedload aggradation, which replaces the shifting sandwaves as transport mechanism. This short-lived shift in flow transport mechanism towards the end of unit III deposition allows for the emplacement of slightly finer stratified beds within unit III. The deposition of these finer stratified ash beds at the top of the unit generates an upwards fining structure. The cessation of a second set of highly mobile granular shifting sandwaves at 1.44 s after flow arrival deposits the 2.02 cm thick, poorly sorted, coarse ash to fine lapilli unit IV (mLT lithofacies, Figure 3-11).

The emplacement of unit IV is succeeded by the deposition of a 0.47 cm thick, stratified lapilli ash unit V (sLT lithofacies, Figure 3-11) through tractional bedload aggradation in the lower flow region. Emplacement of unit V occurs from 1.44 to 2.54s after flow arrival.

Rolling and low traction aggradation in the lower flow region at 2.54s after flow arrival deposits a 1.38 cm thick, massive, poorly sorted, pumice-rich, fine ash to moderate lapilli unit VI (mpLT, Figure 3-11), marked by a sharp, slightly graded lower contact to unit V. The end of the deposition of unit VI at 3.52s after flow arrival occurs concurrently with dusting of individual lapilli clasts across the deposit surface. Simultaneously, settling of very fine to fine ash from the buoyant ash cloud takes place for several tens of seconds, which generates a laminated ash unit (//$sT_{(n)}$, Figure 3-11) that mantles the entire deposit surface. The deposition of this final ash unit marks the termination of the depositional sequence at this observer profile 1.

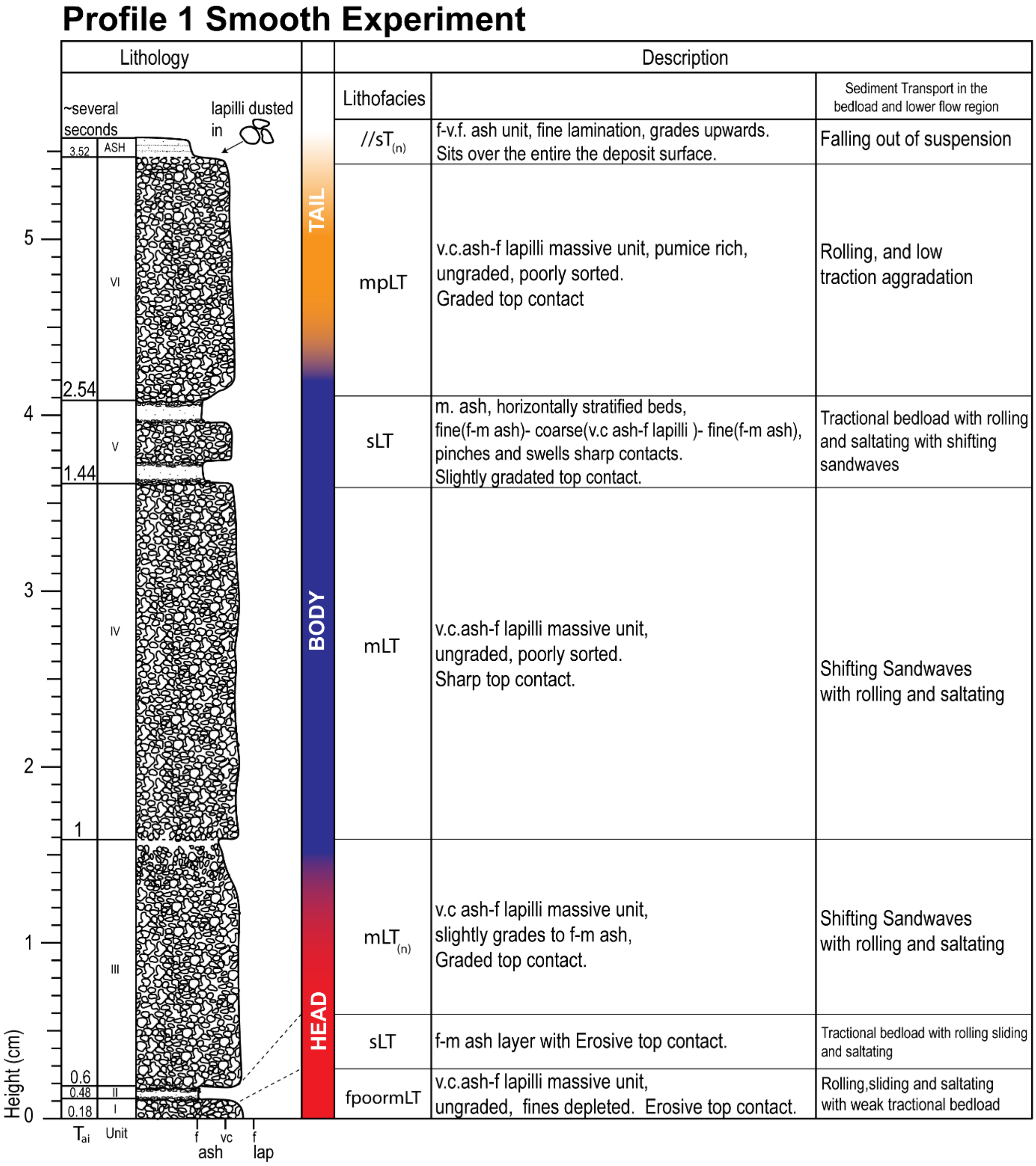

Lithofacies		Sediment Transport in the bedload and lower flow region
$//sT_{(n)}$	f-v.f. ash unit, fine lamination, grades upwards. Sits over the entire the deposit surface.	Falling out of suspension
mpLT	v.c.ash-f lapilli massive unit, pumice rich, ungraded, poorly sorted. Graded top contact	Rolling, and low traction aggradation
sLT	m. ash, horizontally stratified beds, fine(f-m ash)- coarse(v.c ash-f lapilli)- fine(f-m ash), pinches and swells sharp contacts. Slightly gradated top contact.	Tractional bedload with rolling and saltating with shifting sandwaves
mLT	v.c.ash-f lapilli massive unit, ungraded, poorly sorted. Sharp top contact.	Shifting Sandwaves with rolling and saltating
$mLT_{(n)}$	v.c ash-f lapilli massive unit, slightly grades to f-m ash, Graded top contact.	Shifting Sandwaves with rolling and saltating
sLT	f-m ash layer with Erosive top contact.	Tractional bedload with rolling sliding and saltating
fpoormLT	v.c.ash-f lapilli massive unit, ungraded, fines depleted. Erosive top contact.	Rolling,sliding and saltating with weak tractional bedload

Figure 3-11: Stratigraphical column of the deposit of the smooth experiment flow at the most proximal static observer profile 1 (1.6m runout distance). Thicknesses and units belonging to the 5.57 cm thick deposit are drawn to scale. The time stamp of each unit boundary is after flow arrival (T_{ai}). Non-genetic stratigraphical lithofacies, sediment transport mechanisms and the relevant flow structure are reported for each emplaced unit.

(ii) Profile 2

At observer profile 2 (at 3.7 m runout distance), deposit emplacement initiates at 0.2 s after flow arrival. The development of a tractional bedload in the lower flow region at 0.2 s after flow arrival leads to the aggradation of a 0.075 cm thick, massive, fines-depleted, coarse to very coarse ash unit I (fpoormT lithofacies, Figure 3-12). The full thickness of unit I is emplaced in c. 0.4 s, where most of the unit is rapidly deposited in the first c. 0.2 s of unit aggradation. Following the deposition of this first unit, a non-depositional phase starts at 0.62s after flow arrival. This non depositional phase (unconformity marked in red, Figure 3-12) lasts until 1.08s after flow arrival.

The emplacement of the second unit II occurs after the cessation of the non-deposition phase at 1.08 s after flow arrival. Tractional bedload at 1.08 to 2.32s after flow arrival aggrades the 0.0957 cm thick unit II. Unit II is a stratified unit composed of alternating coarse and fine ash beds (sT lithofacies, Figure 3-12). Stratified beds within unit II display sharp contacts, and gently dip in a downstream direction. Termination of emplacement of unit II at 2.32 s after flow arrival coincides with a shift into a short-lived period of no net deposition. The period of no net deposition lasts from 2.32 to 2.48s after flow arrival (unconformity marked in red, Figure 3-12). The period of no net deposition leads to an unconformable and erosive boundary between unit II and the subsequent unit III.

At 2.48 s after flow arrival, sediment transport mechanism in the lower flow region changes. Sediment transport mechanism in the lower flow region shifts to low tractional deposition with rolling clasts. This leads to the deposition of unit III, which is a massive, poorly sorted, coarse to very coarse ash unit (mT lithofacies, Figure 3-12). The cessation of unit III deposition at 2.76 s after flow arrival coincides with the rapid settling of fine to medium ash particles locally. This leads to the generation of unit IV, which is a 0.073cm thick, fine to medium ash, finely laminated unit (//sT lithofacies, Figure 3-12), marked by a conformable sharp boundary with the underlying unit III. Concurrent with the deposition of unit IV is the appearance of individual lapilli clasts which are observed to scatter across the deposit surface. After the deposition unit IV, sustained deposition of fine ash sized particles falling out of suspension produce the final ash cover unit. This normally graded, very fine to fine, laminated ash unit mantles the entire deposit surface(//sT$_{(n)}$ lithofacies, Figure 3-12), marked by a gradational contact to the underlying unit IV. Deposition of this top ash unit marks the termination of the depositional sequence at this profile location

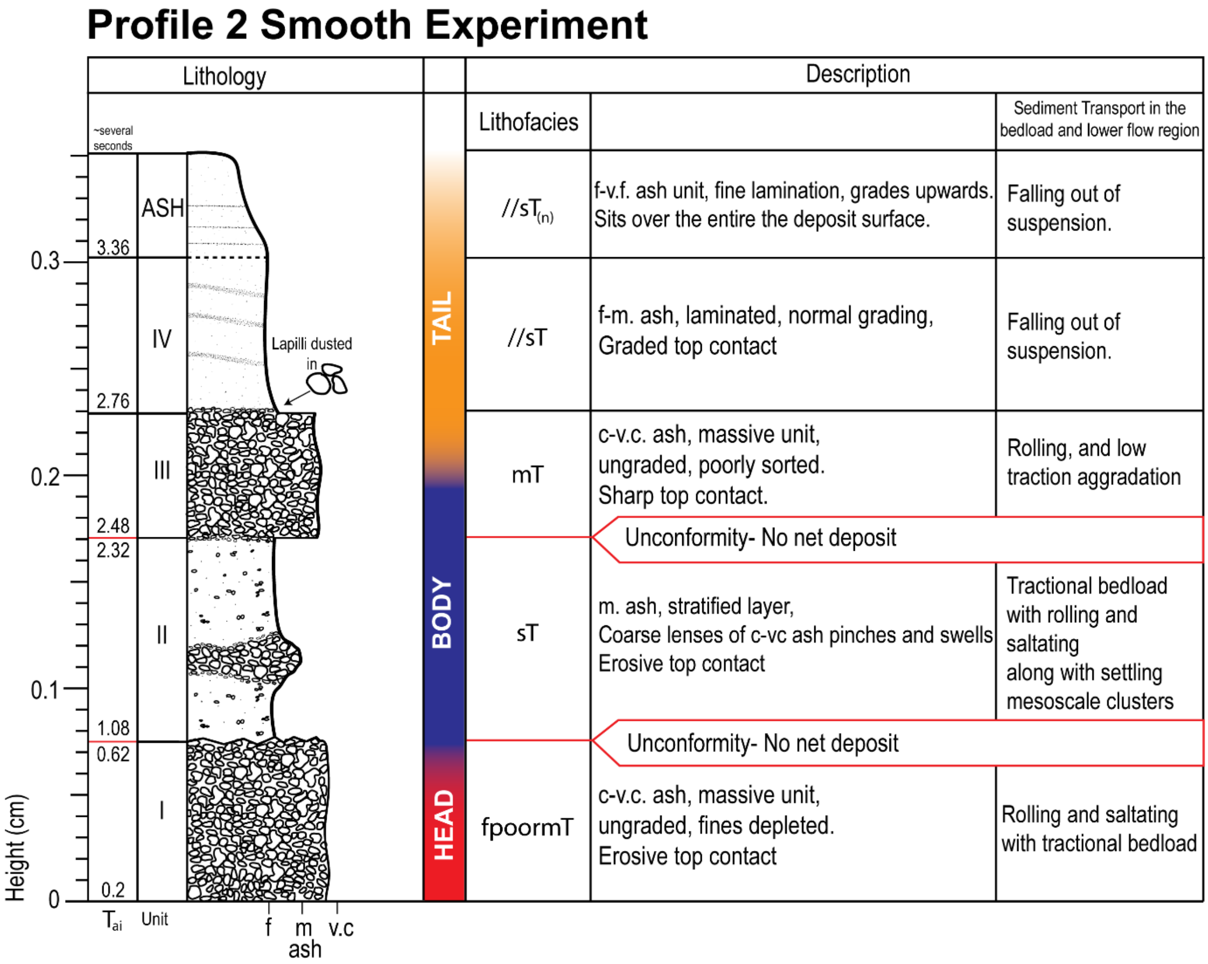

Figure 3-12: Stratigraphical column of the deposit of the smooth experiment flow at the static observer profile 2 (3.7m runout distance). Thicknesses and units belonging to the 0.351 cm thick deposit are drawn to scale. The time stamp of each unit boundary is after flow arrival (T_{ai}). Unconformable boundaries (red unit boundaries) represent periods of n.n.d during flow passage. Non-genetic stratigraphical lithofacies, sediment transport mechanisms and the relevant flow structure are reported for each emplaced unit.

(iii) Profile 3

Deposition by the smooth experiment flow at observer location profile 3 (at runout distance of 5.6 m) occurs after an initial period of non-deposition. The development of a weak tractional bedload at 0.48s after flow arrival subsequently deposits a 0.069 cm thick, massive, fines-depleted, coarse to very coarse ash unit (fpoormT lithofacies, Figure 3-13). This unit I is emplaced from c. 0.48 to 1.21 s after flow arrival, by the flow head, where the bulk of the unit is deposited within the first c. 0.2 of aggradation (Figure 3-13). Deposition of unit I terminates at 1.21 s after flow arrival.

From 1.21 to 1.68 s after flow arrival, the flow is characterized by a period of no net deposition. The period of no net deposition is characterized by the unconformable contact between unit I and II. The period of no net deposition is followed by deposition from tractional bedload, which emplaces a 0.09 cm thick unit II, characterized by very fine to fine ash laminations (//sT lithofacies, Figure 3-13), dipping in a downstream direction. During deposition of unit II, the lower turbulent flow region of the flow body displays formation of fast settling mesoscale clusters which feed the tractional bedload below. Deposition of unit II lasts until 3.28 s after flow arrival.

At 3.28s after flow arrival dusting of individual lapilli clasts occurs. Individual lapilli clasts are observed to scatter across the deposit surface. Simultaneously, over a course of several tens of seconds, very fine to fine ash particles slowly settle out of suspension. The final ash cover bed deposit is normally graded and displays fine internal laminations (//sT$_{(n)}$ lithofacies, Figure 3-13). These cover the entirety of the deposit surface and mark the termination of the depositional sequence at this observer profile location 3.

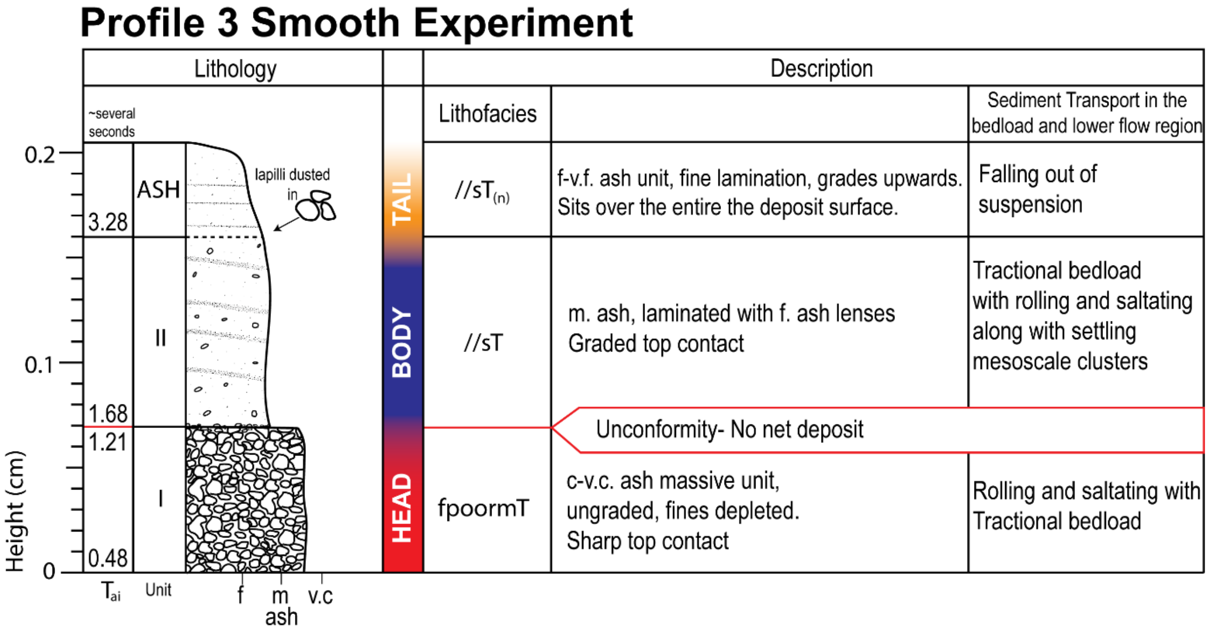

Lithofacies		Sediment Transport in the bedload and lower flow region
$//sT_{(n)}$	f-v.f. ash unit, fine lamination, grades upwards. Sits over the entire the deposit surface.	Falling out of suspension
//sT	m. ash, laminated with f. ash lenses Graded top contact	Tractional bedload with rolling and saltating along with settling mesoscale clusters
	Unconformity- No net deposit	
fpoormT	c-v.c. ash massive unit, ungraded, fines depleted. Sharp top contact	Rolling and saltating with Tractional bedload

Figure 3-13: Stratigraphical column of the deposit of the smooth experiment flow at the static observer profile 3 (5.6 m runout distance). Thicknesses and units belonging to the 0.206 cm thick deposit are drawn to scale. The time stamp of each unit boundary is after flow arrival (T_{ai}). Unconformable boundaries (red unit boundaries) represent periods of n.n.d during flow passage. Non-genetic stratigraphical lithofacies, sediment transport mechanisms and the relevant flow structure are reported for each emplaced unit

(iv) Profile 4

Deposition at the static observer profile 4 (located at 9.3 m runout distance) occurs after a brief period of non-deposition. The deposition of unit I occurs after 0.22s of flow arrival. This coincides with the development of a tractional bedload which deposits the 0.085 cm thick, massive, fines-depleted, coarse to very coarse ash unit I (fpoormT lithofacies, Figure 3-14). The bulk of unit I is rapidly deposited within the first c. 0.2 s of unit aggradation (Figure 3-14; profile 4), and its emplacement ceases at c. 1.03s after flow arrival. The termination of deposition of unit I coincides with the start of a non-depositional phase that lasts until 1.7 s after flow arrival. This erosive unconformable contact between unit I and II reflects the period of no net deposition.

With the cessation of the period of non-deposition, tractional bedload at the flow base begins depositing the 0.07cm thick, very fine to fine ash, laminated unit II (//sT lithofacies, Figure 3-14) gently dipping in downstream direction. Deposition of unit II is also associated with the formation of fast settling mesoscale clusters impacting into the transient region which feeding the tractional bedload. The deposition of unit II terminates at c. 2.64 s after flow arrival.

At 2.64s after flow arrival, individual lapilli clasts are observed to scatter across the deposit surface. A final fine ash unit is deposited simultaneously. Over the course of several tens of seconds, very fine to fine ash particles slowly settle out of suspension. This resulting ash cover bed deposit, which covers the entire deposit surface, is normally graded, and displays fine internal laminations (//sT$_{(n)}$ lithofacies, Figure 3-14). This final ash unit marks the termination of the depositional sequence at this observer profile location 4.

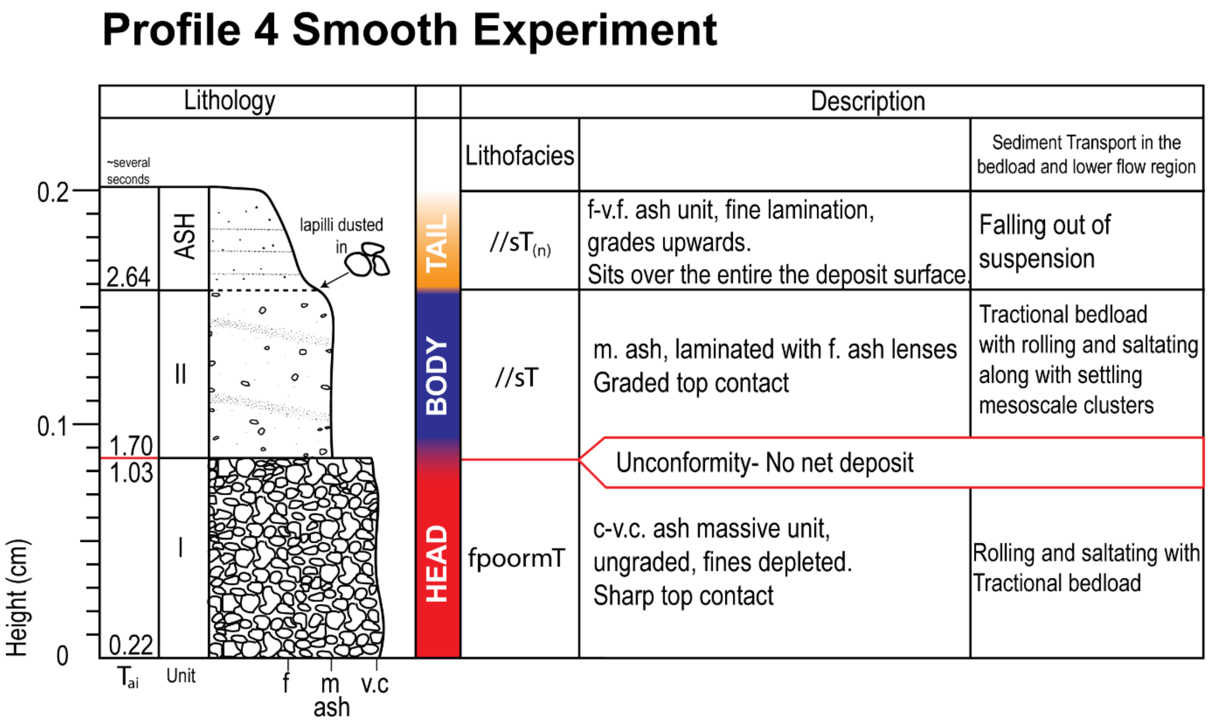

Figure 3-14: Stratigraphical column of the deposit of the rough experiment flow at the static observer profile 4 (9.3 m runout distance). Thicknesses and units belonging to the 0.201 cm thick deposit are drawn to scale. The time stamp of each unit boundary is after flow arrival (T_{ai}). Unconformable boundaries (red unit boundaries) represent periods of n.n.d during flow passage. Non-genetic stratigraphical lithofacies, sediment transport mechanisms and the relevant flow structure are reported for each emplaced unit.

3.2.D Flow structure deposit correlation

The presented depositional sequences described at the several static observer profiles for both the rough and smooth experiments flows lend themselves to establish a correlation based on bypassing flow structure. Figure 3-15 and Figure 3-16 summarises the stratigraphic sequence of the deposits emplaced by both the rough and smooth experiments flow and present a link between depositional units and the bypassing flow structure.

The emplacement of a fpoormLT/T lithofacies (Figure 3-15 and Figure 3-16) is characteristic for the first depositional unit generated by the passage of the flow head throughout the entire runout.

At the 1.6m location, both the rough and smooth experiments flows are characterised by the local occurrence highly mobile granular shifting sandwaves during deposit formation. These shifting sandwaves are associated with the deposition of mLT lithofacies. Deposition of mLT lithofacies begin at the rear of the head, and throughout the propagation of the flow body. Noteworthy is the localised occurrence of these shifting sandwaves which do not occur at static observer profiles located further downstream. In both experimental runs, the deposition of these mLT lithofacies by shifting sandwaves occurs at regular intervals of c. 0.4-0.5 s. However, i) the number of shifting sandwave pulses differs for both the rough and smooth experiments flows, where three distinct pulses are identified for the rough experiment flow, compared to only two for the smooth experiment flow, and ii) the emplaced mLT units by the shifting sandwaves are thinner in the depositional record for the rough experiment flow, compared to those found in the smooth experiment flow. At all other times of the flow body at profile 1, when shifting sandwaves do not occur, the main deposition mechanism in the lower flow boundary is associated with tractional bedload deposition.

At static observers located further than 1.6m runout distance, the back of the head is associated with a period of non-deposition/erosion. As a function of distance, the duration of non-deposition at the rear of the head stretches into the proximal flow body. The period of non-deposition occurring at the rear of the head is always marked by a near planar, erosive, unconformable contact at all observer locations. Noteworthy, this characteristic deposition pattern by the flow head is consistent between both the rough and smooth experiments experimental flows.

The presence of a laterally correlatable stratified lithofacies across the runout is characteristic with the deposit emplacement by the flow body and is the case for both the rough and smooth experiments flows (Figure 3-15 and Figure 3-16).

At observer profiles 1, the deposition of units by shifting sandwaves interrupts the deposition of the sLT lithofacies (Figure 3-15 and Figure 3-16) during the flow body passage. This concurrent deposition of sLT beds and mLT beds (through shifting sandwaves) results either in the production of multiple sets of sLT separated by mLT beds, or the deposition of an mLT bed overprinted by characteristics of the sLT bed (e.g., smooth experiment flow see profile 1, unit III; Figure 3-16).

In both experiments, stratified lithofacies emplaced by the flow body at profile 2 location (3.7m) are bounded by top and bottom erosive unconformities. The non-depositional nature of the distal flow body is exclusive to observer location profile 2 for both experimental flows.

As the flow transitions from the body to the tail, deposition of mpLT/mpT/mT lithofacies (Figure 3-15 and Figure 3-16) occurs through a low traction aggradation mechanism. At the most proximal profile location (1.6m), units emplaced during the body-tail passage are enriched in pumice components (mpLT). At profiles located further, mT bed lithofacies is deposited instead. Noteworthy is that these mT units occur up to observer profile 3 (at 5.6 m runout distance, Figure 3-15) for the rough experiment flow, and up to profile 2 (3.7 runout distance, Figure 3-16) for the smooth experiment flow. After 3.7 m, for the case of the smooth experiment flow, instead of depositing a massive unit at the body-tail boundary, the distal locations at 5.6 and 9.3m are characterized by deposition of $//sT_{(n)}$ lithofacies (Figure 3-16).

Deposition in the tail of both the rough and smooth experiments flows is characterized by the emplacement of the $//sT_{(n)}$ lithofacies (Figure 3-15 and Figure 3-16). The buoyant ash cloud deposition of the $//sT_{(n)}$ lithofacies characterizes the final deposition from the experimental currents.

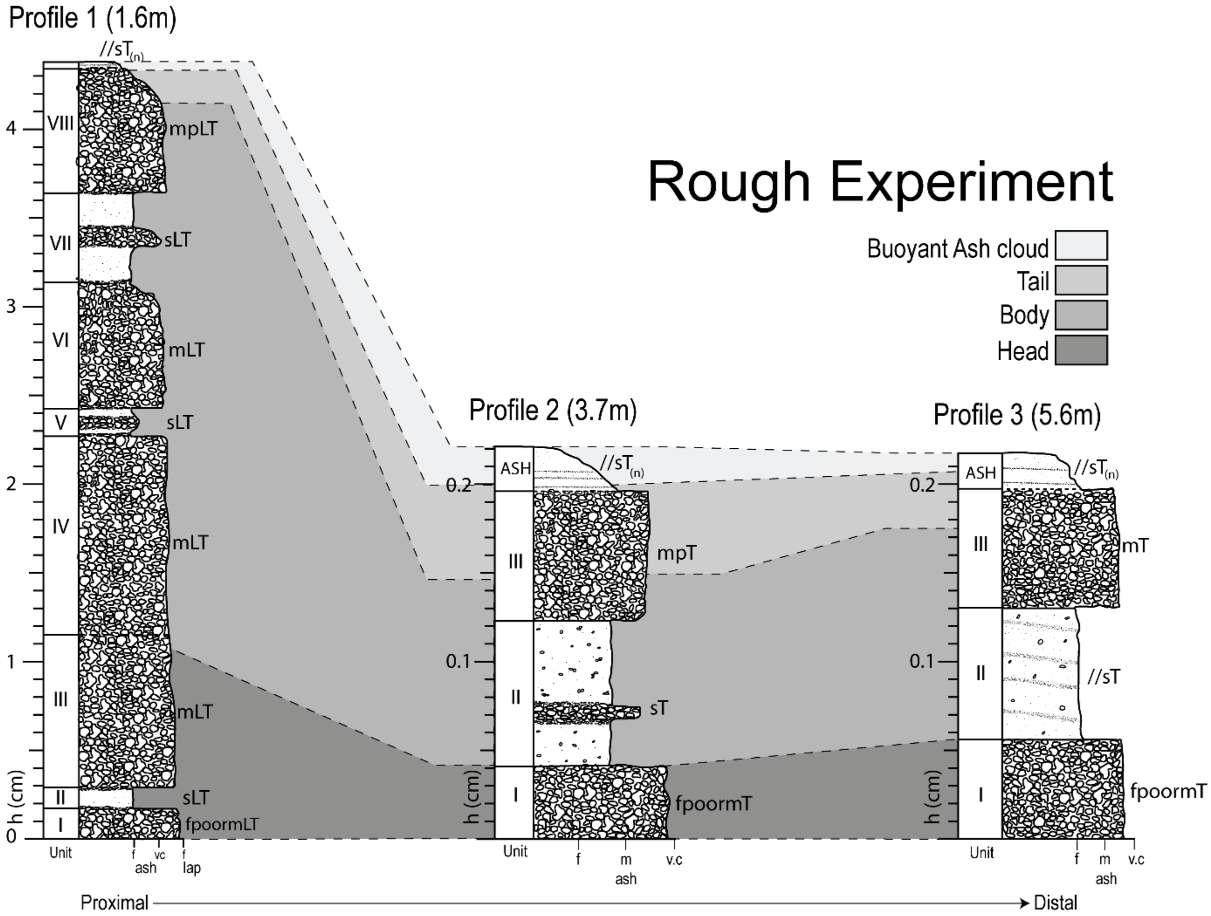

Figure 3-15: Stratigraphy of the rough experiment dilute PDC deposit highlighting depositional units and their correlation downstream. Profile 2 and 3 are not drawn to scale. Correlations in grey refer to flow regions responsible for emplacing specific depositional units. Overall, the deposits display exponential thinning over distance. The changes from profile 1 (1.6 m) to profile 2 (3.7m) highlight the very dynamic proximal deposit formation phase. Units emplaced at profile 2 (3.7m) and profile 3 (5.6m) are highly similar in their depositional architecture.

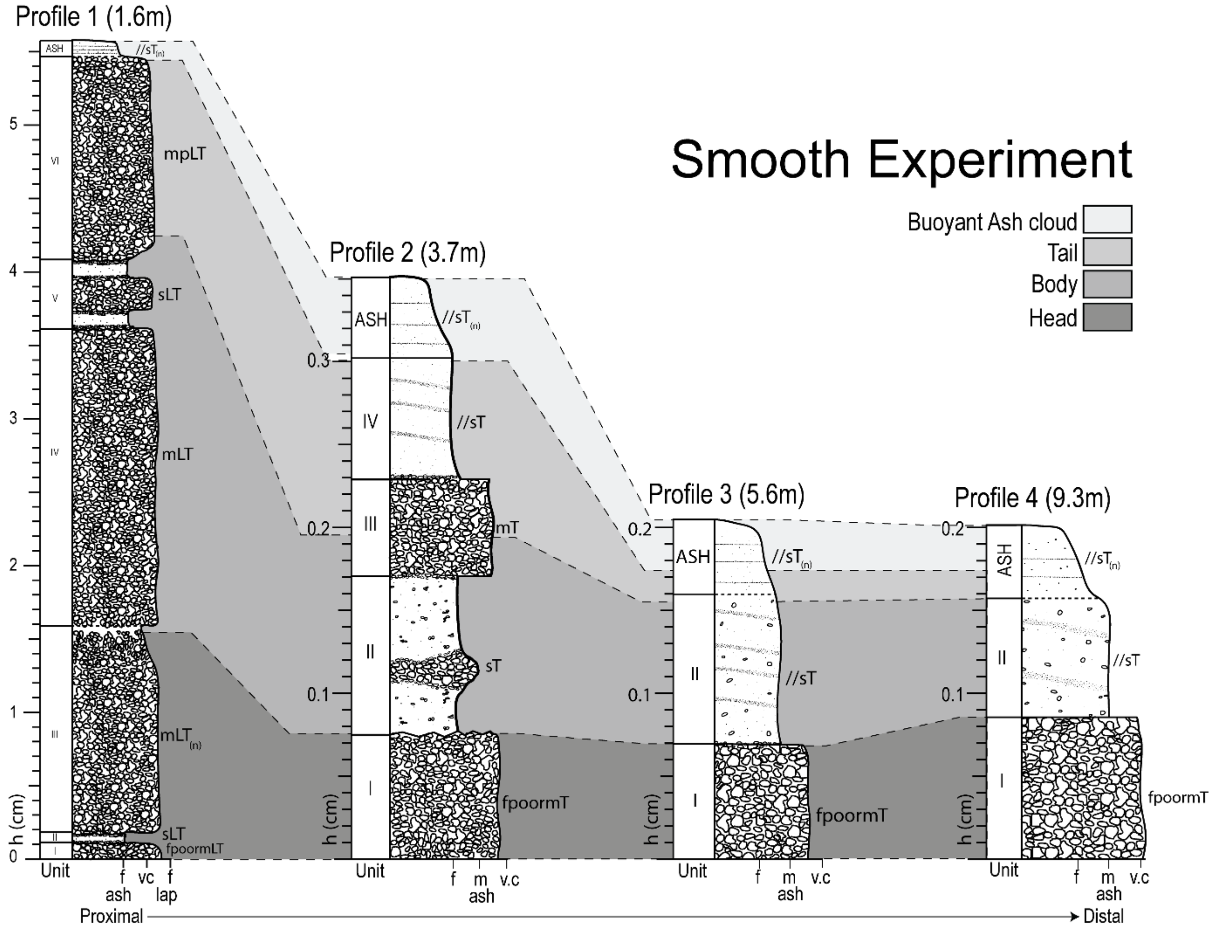

Figure 3-16: Stratigraphy of the rough experiment dilute PDC deposit highlighting depositional units and their correlation downstream. Profile 2, 3 and 4 are not drawn to scale. Correlations in grey refer to flow regions responsible for emplacing specific depositional units. Overall, the deposits display exponential thinning over distance. The changes from profile 1 (1.6 m) to profile 2 (3.7m) highlight the very dynamic proximal deposit formation phase. Units emplaced at profile 2 (3.7m), profile 3 (5.6m) and profile 4 (9.3 m) are highly similar in their depositional architecture.

At Figure 3-17, deposit isochrones of both experiments flow are displayed along with the flow structure responsible for the depositing respective regions. The final deposit have been delineated by colours to represent the flow structures (low head, body (proximal, medial, and distal body regions), tail, and buoyant ash cloud).

Proximal (<3m) vertical deposition profile represents a complete depositional sequence from flow head to tail. At 0.5s, deposition over c. 2 m runout distance solely occurs from the head. Deposition from the proximal and medial body initiates between times 0.5 to 2s. Distal body commences deposition after the 4s of flow propagation when deposit reaches c. 16 m runout distance. Shortly after, tail deposition initiates between 2-4s of deposition. After 4 s of flow propagation, the buoyant ash cloud begins emplacing a very thin cover bed. The buoyant ash cloud begins to deposit after 4s.

The complete depositional sequence from flow head to tail propagates outwards and decreases in thickness with time. Deposit reaches runout distances of c. 2, 9, 16, and 22m at flow propagation times 0.5, 2, 4, 8s. Final deposition from the buoyant ash cloud (yellow beds, Figure 3-17) at 24 m runout distance finishes at c. 20-30s.

The rough and smooth experiments flows display very similar overall deposit architecture (Figure 3-17). Up to 24m of runout distance both flows display a vertical sequence that represents a sequence of deposition from flow head-tail and a final cover bed emplaced by the ash cloud.

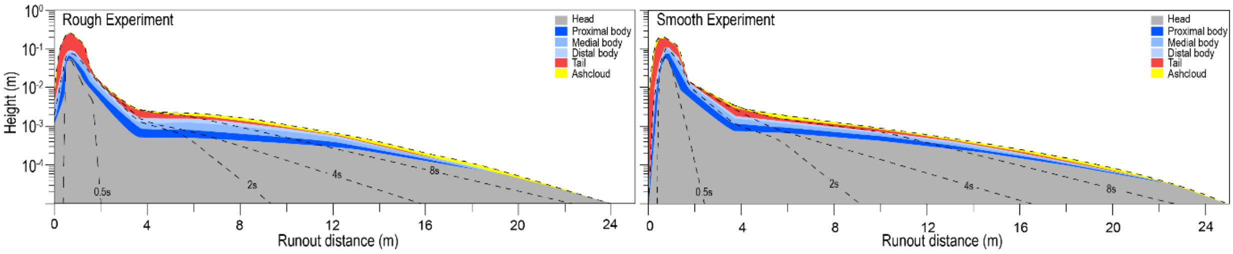

Figure 3-17: Height-distance plot of deposit and deposition isochrones (dashed lines displays relevant times of deposit emplacement in seconds) from both experiments. Outlined portions of deposit emplaced by specific flow structures are displayed (relevant colours are defined in the legend). Heights (meters) are plotted in a logarithmic scale for better visualization. Spatiotemporal deposit aggradation supports the interpretation that deposition from a dilute PDC occurs as a longitudinally diachronous sequence characterizing the deposition from a flow with a: head, body, and tail.

3.2.E Spatio-temporal sedimentation rates

The following sections explains the different sedimentation rate trends observed at a number of static observer location along the flow runout for both the rough and smooth experiments experimental flows. The here described profile locations for both flows are characterized by deposit thicknesses of c. 4-6 cm at the 1.6 m observer location (Profile 1, Figure 3-18 and Figure 3-19), thinning down to c. 0.2 cm at the 9.3 m observer location (Profile 4, Figure 3-19).

At all observer locations during flow passage, the front of the head is characterized by a non-depositional period (n.n.d, Figure 3-18 and Figure 3-19). The earliest period of deposition recorded by the head of both the rough and smooth experiments flows occur at c. 0.2 s and 0.16 s after flow arrival, respectively. Compared to all other locations downstream, profile 1 (at 1.6 m) is the only location that is marked by a constantly depositing flow during its passage.

Sedimentation rates for the rough experiment flow at profile 1 are characterized by a marked regular periodicity of c. 1 s (Figure 3-18 a). The first peak in sedimentation rate occurs at c. 1 s after flow arrival with sedimentation rates of c. 4 cm s^{-1}. Subsequent sedimentation rate peaks occur at c. 2 s (passage of the flow body) and 3.25 s after flow arrival (transition from the distal body to the tail), and feature sedimentation rates up to c. 2 cm s^{-1}. Cyclic troughs are associated with periods of low sedimentation rates (Figure 3-18 a). Conversely, the smooth experiment flow passage at profile 1 displays a less pronounced periodicity in the sedimentation rate but features a period of elevated sedimentation rate at around c. 1 s after flow arrival with values up to c. 7 cm s^{-1}. After this period of elevated sedimentation, sedimentation rates drop and maintain values around c. 1 cm s^{-1}. Similar to the rough experiment flow, the smooth experiment flow displays elevated sedimentation rates of c. 3 m s^{-1} at around 3.1 s after flow arrival during the late-stage flow propagation. Final deposit is characterized by thicknesses of c. 4.5 and 5.6 cm for the rough and smooth experiments flows, respectively.

At medial to distal reaches, periodicity in sedimentation rates decreases both in amplitude and duration. Cyclic troughs, or periods of low to negative sedimentation rate, are associated with no net deposition, while periods of increased sedimentation rate are associated with deposit aggradation. At the observer profile 2, located at 3.7 m distance from impact, sedimentation and deposit emplacement in both the rough and smooth experiments flows are characterized by the largest occurrence of periods of no net deposition (Figure 3-18 b and

Figure 3-19 b). Together with the period of non-deposition in the flow front, non-depositional periods occur at the transition from the back of the head to the proximal body, and within the distal body. The duration of these periods of no net deposition are however different between both experimental flow where the rough experiment flow exhibits longer periods of non-deposition than the smooth experiment flow. As such, average sedimentation rates during the passage of the smooth experiment flow at the static profile 2 location are higher than for the rough experiment flow, with values of 0.067 cm s^{-1} and 0.055 cm s^{-1}, respectively.

At profile 2, between these periods of no net deposition, three distinct periods of deposition can be identified. For both the rough and smooth experiments flow, the first period of deposition occurs just after the non-depositional front and is marked by higher sedimentation rates (up to 0.4 cm s^{-1} for the rough and smooth experiments flow, respectively; Figure 3-18 b and Figure 3-19 b), compared to the successive second period of deposition occurring within the body, with sedimentation rates of c. < 0.1 cm s^{-1} for the rough and smooth experiments flow, respectively. Noteworthy, is a period of high sedimentation during the late-stage flow passage of the flow tail, with rates of up to 0.4 cm s^{-1} for the rough experiment and 0.3 cm s^{-1} for the smooth experiment flows, which concomitantly mark the end of the deposit emplacement.

At observer locations profile 3 and 4, located at 5.6 m and 9,3 m runout distance, respectively, only two periods of non-deposition occur. For both the rough and smooth experiments flow, these are located at the front of the head and in the rear of the head to the body transition (Figure 3-18c and Figure 3-19 c). Overall, sedimentation rates are lower within the flow body passage, compared to the late-stage passage of the flow tail at profile 3 for the rough experiment flow. The latter are characterized by sedimentation rates up to 0.3 cm s^{-1}. However, elevated sedimentation rate at the late-stage passage of the tail compared to the body is not observed at profile 3 and 4 of the smooth experiment flow.

Rhythmic cycles in depositional rates are still present at these medial to distal runout locations. At profile 3 for both the rough and smooth experiments flow, cyclic periods of elevated deposition rate occur at intervals of c. 1 s. This periodicity in the sedimentation rate can also be observed in the most distal observer profile 4, marked by oscillations approx. every 0.45s.

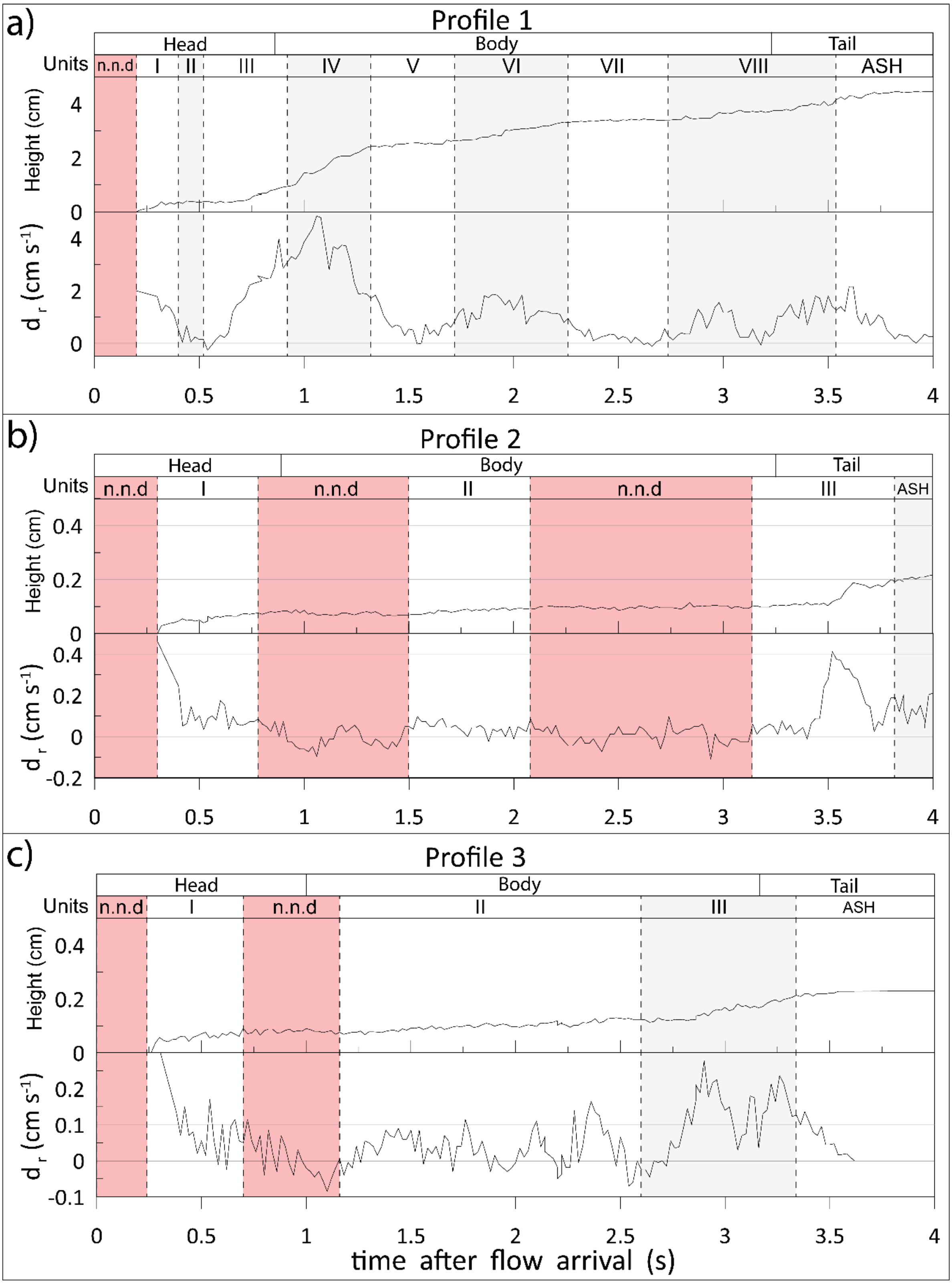

Figure 3-18: Time variant deposit thickness and sedimentation rate (d_r) plotted against time for the bypassing rough experiment flow at (a) 1.6, (b) 3.7, (c) 5.6m static observer profiles. Depositional record of profile 4 (9.3 m location) is not displayed due to measurement limitations. Flow is subdivided into head, body, and tail. Sedimentation rate is characterised by periods of no net deposition (n.n.d), resulting in unconformities in the deposit. Sedimentation rates are marked by alternating times of high and low rates, together with erosional periods throughout the duration of the flow passage.

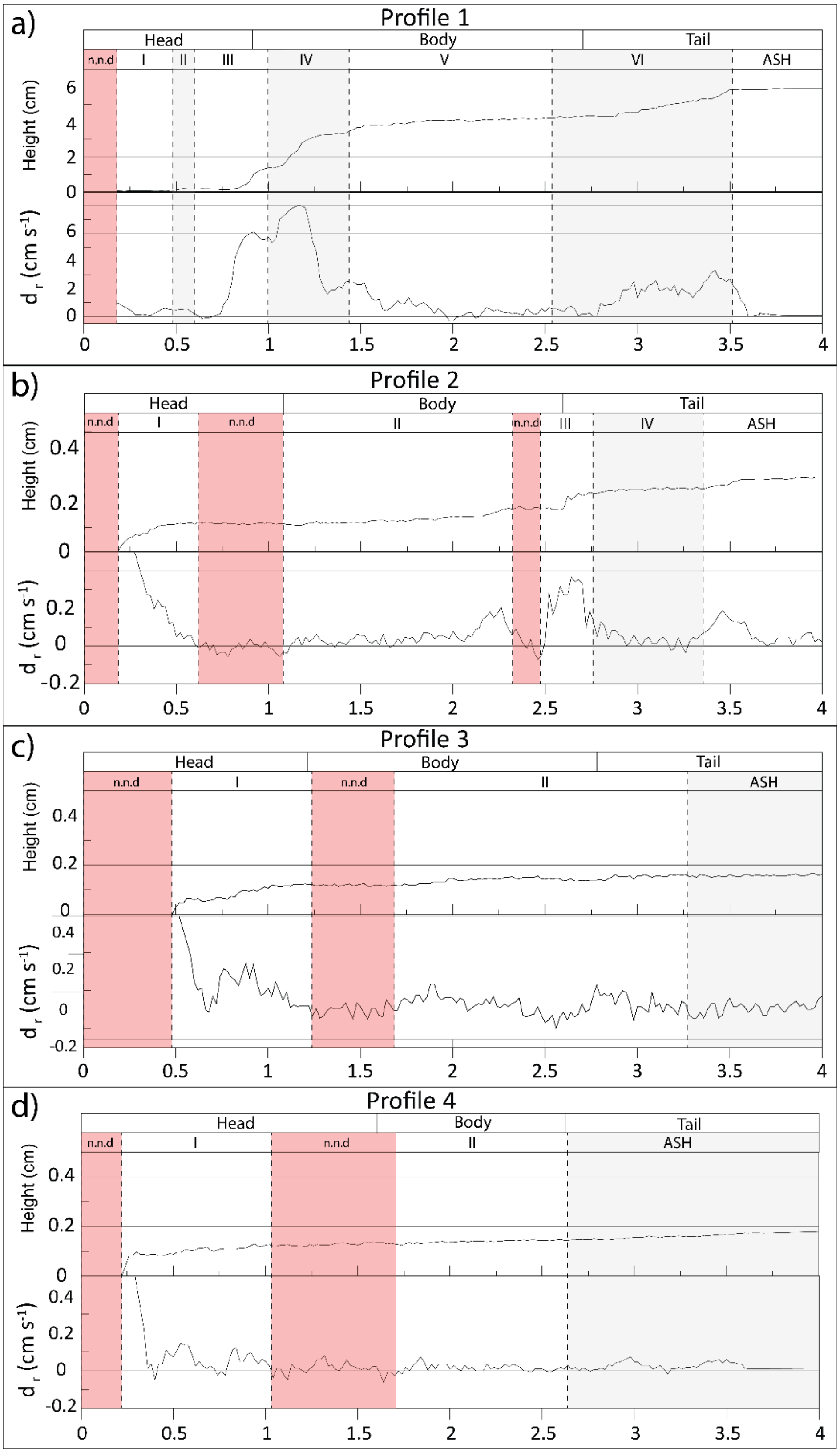

Figure 3-19: Time variant deposit thickness and sedimentation rate (d_r) plotted against time for the bypassing smooth experiment flow at (a) 1.6, (b) 3.7, (c) 5.6, and (d) 9.3 m static observer profiles. Flow is subdivided into head, body, and tail. Sedimentation rate is characterised by periods of no net deposition (n.n.d), resulting in unconformities in the deposit. Sedimentation rates are marked by alternating times of high and low rates, together with erosional periods throughout the duration of the flow passage.

3.3 Vertical flow velocity and density structure

In order to investigate potential relationships between the Spatio-temporal evolution of the deposits and the evolving internal flow structure, this research characterised the vertical flow velocity and density structure as a function of time at four different observer locations.

Figure 3-20 and Figure 3-21 display height-time contour plots of flow velocity magnitudes at four different observer locations (1.6, 3.7, 5.6, and 9.3 m from impact location).

In both experimental runs, the time-integrated velocity magnitude shows wall shear with the solid substrate produced the inner wall region, where velocities increased up into the vertical flow structure until the height of the velocity maximum, which is characterised by zero shear. The height of the velocity maximum marked the boundary between the wall and the above located outer jet region. The outer jet region was generated due to free shear with the upper flow boundary. The jet-region was furthermore characterised by the body-wake boundary, located at an average height of c. 1.2 m, above which the highly diluted flow wake region occurred.

For both the rough and smooth experiments runs, the leading frontal head structure was characterised by relative moderate to high velocities in the range of 4- 6.5 m s-1 up to the flow head boundary to the atmosphere. The frontal nose structure at the flow base sat slightly above the ground surface due to wall shear with the solid ground substrate. The centre of the head displayed moderate to high velocity magnitude (> 4 m s^{-1}) that persisted in the upper flow regions. In the rear of the head, a low velocity zone formed in a region above the body-wake boundary (above c. 1.2 m). Here, the shedding of rotating vortices (Helmholtz instabilities) from the expanding flow head constantly fed the flow wake above the flow body.

Flow velocity magnitudes fade over distance (Figure 3-20 and Figure 3-21). At 1.6 m runout distance mean velocity magnitude over 4s of flow propagation is c. 5.7 and 5 m s^{-1}, for the rough and smooth experiments flows, respectively. At 9.3 m runout distance, the mean velocity magnitude over 4s of flow is c. 3.5 and 3.3 m s^{-1}, for the rough and smooth experiments flows, respectively. The velocity magnitude structures are more intense, yet for a shorter duration in the smooth experiment flow.

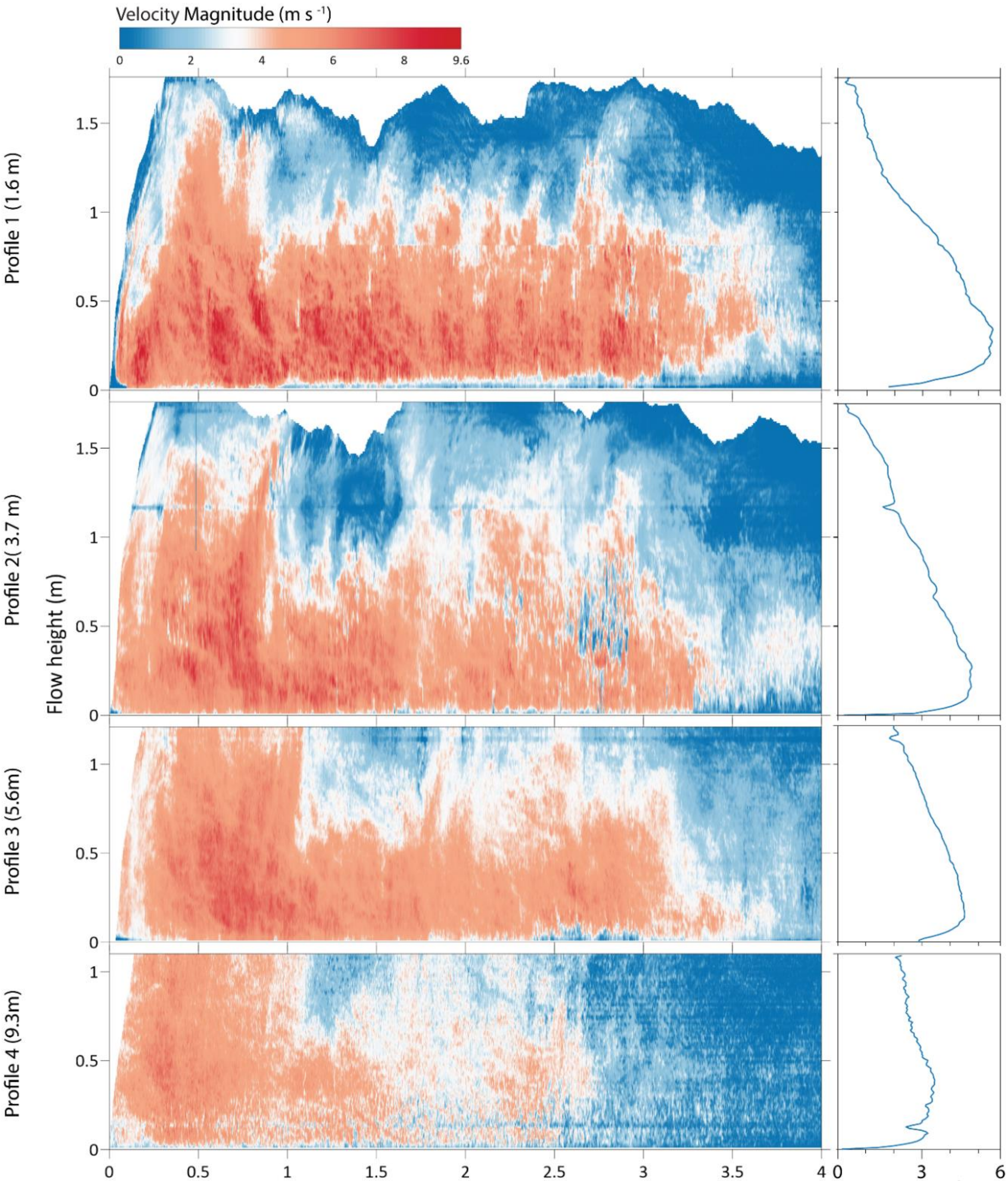

Figure 3-20: Experimental rough experiment flow velocity magnitude contour plot distributions at static observer locations 1.6, 3.7, 5.6, and 9.3 m from impact location. Mean (over 4s) velocity magnitude (m s^{-1}) profile is displayed on the right. The head of the flow is characterised by moderate-high magnitudes (c. >4 m s^{-1}, red shades) that extends into the upper flow regions (> 0.5m of flow height). The body is characterised by the moderate-high magnitudes (c. >4 m s^{-1}, red shades) that exists into the body-wake boundary (flow height of c. 0.75-1.0 m). The wake sits above the body and is characterised by the low magnitudes (c. <4m s^{-1}, blue shades). The tail of the flow is characterised by the deceleration of the velocity magnitudes in the body occurring at 2.5-3.5s after flow arrival. Over runout distance, the maximum mean (over 4s of flow passage) velocity magnitudes decreases from c. 5.7 m s^{-1} at runout distance of 1.6m, to c. 3.5 m s^{-1} at runout distance of 9.3m. Compared to the smooth experiment flow, the rough experiment flow velocity magnitudes display an overall longer flow structure (on average medium-high flow velocity magnitudes (c. >4 m s^{-1}, red shades) exists for c. 3.5s after flow arrival).

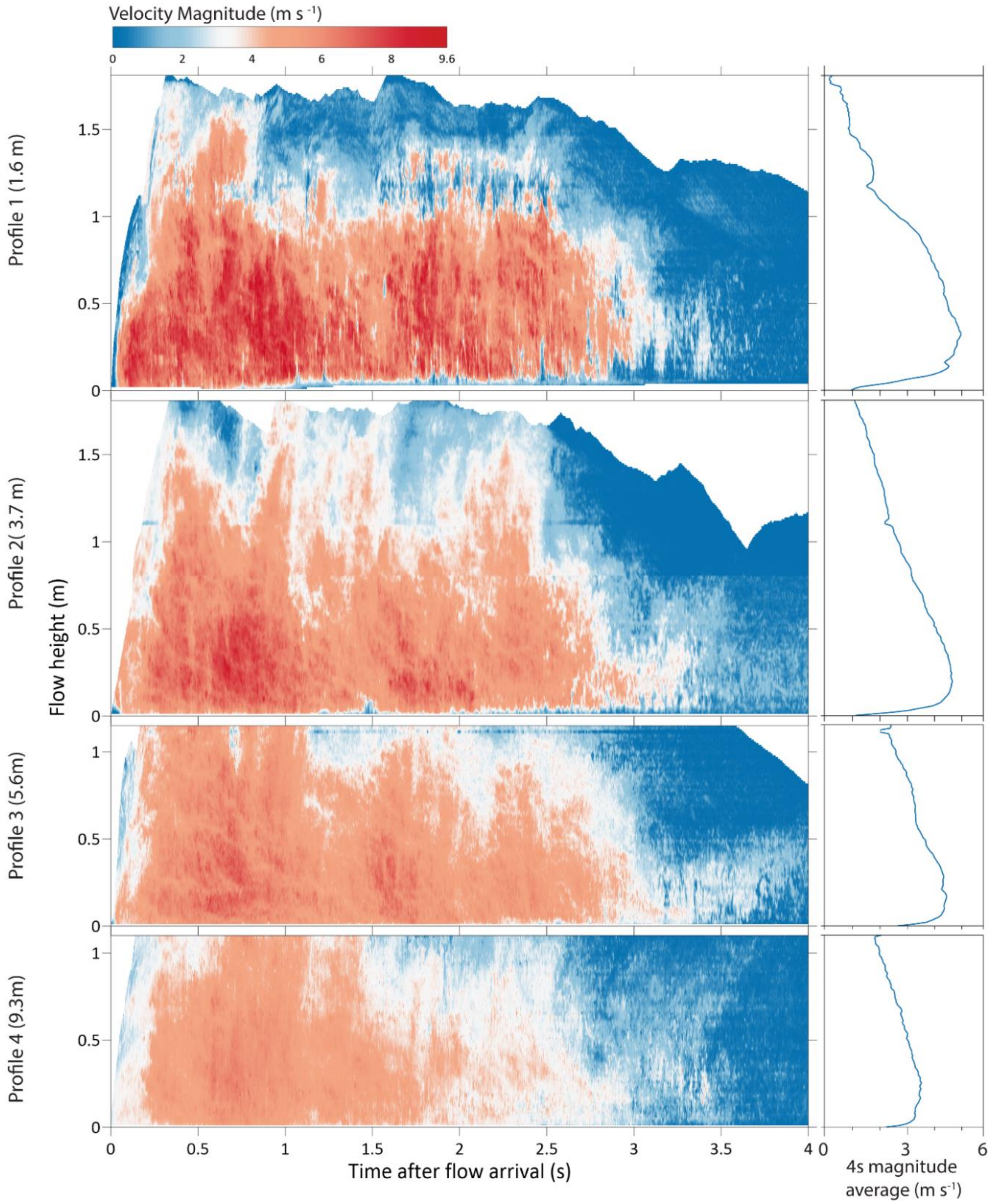

Figure 3-21: Experimental smooth experiment flow velocity magnitude contour plot distributions at static observer locations 1.6, 3.7, 5.6, and 9.3 m from impact location. Mean (over 4s) velocity magnitude (m s^{-1}) profile is displayed on the right. The head of the flow is characterised by moderate-high magnitudes (c. >4 m s^{-1}, red shades) that extends into the upper flow regions (> 0.5m of flow height). The body is characterised by the moderate-high magnitudes (c. >4 m s^{-1}, red shades) that exists into the body-wake boundary (flow height of c. 0.75-1.0 m). The wake sits above the body and is characterised by the low magnitudes (c. <4m s^{-1}, blue shades). The tail of the flow is characterised by the deceleration of the velocity magnitudes in the body occurring at 2.5-3s after flow arrival. Over runout distance, the maximum mean (over 4s of flow passage) velocity magnitudes decreases from c. 5 m s^{-1} at runout distance of 1.6m, to c. 3.3 m s^{-1} at runout distance of 9.3m. Compared to the rough experiment flow, the smooth experiment flow velocity magnitudes display an overall shorter flow structure (on average medium-high flow velocity magnitudes (c. >4 m s^{-1}, red shades) exists for c. 3.2s after flow arrival).

Figure 3-22 and Figure 3-23 show height-time contour plots of density magnitudes at four different observer locations Vertical profiles of flow densities at selected interval times after flow passage reveal a typical density profile for stratified particle-laden gravity currents.

In both cases, clearly noticeable is the change from high bulk flow density at the most proximal location (approximately 2.6 kg m^{-3}), to a highly diluted flow in medial-distal reaches (approximately 1.6 kg m^{-3}).

From proximal to distal observer locations, the bulk flow head densities (kg m^{-3}) changed from 3.15 to 1.97, and 3.22 to 1.83, for both the rough and smooth experiments flow, respectively. Similarly, the flow body and wake bulk densities (kg m^{-3}) changed from 2.61 to 1.63, and 2.54 to 1.36, when compared from proximally to distally located observer locations.

The smooth experiment flow showed density distributions that were more concentrated in the head compared to the body, while the rough experiment had a more evenly distributed densities throughout its entire flow structure. For both flows, the body regions appeared to be similarly diluted in distal reaches (static observer location 9.3 m, Figure 3-22 and Figure 3-23).

The lower flow boundary regions (lowermost 0.01 – 0.15 m flow height) of both the rough and smooth experiments flows at the static observer location 1.6 m featured the highest densities with mean values of 5.64 and 7.92 for the rough and smooth experiments flow, respectively, when compared to the subsequent downstream located profiles.

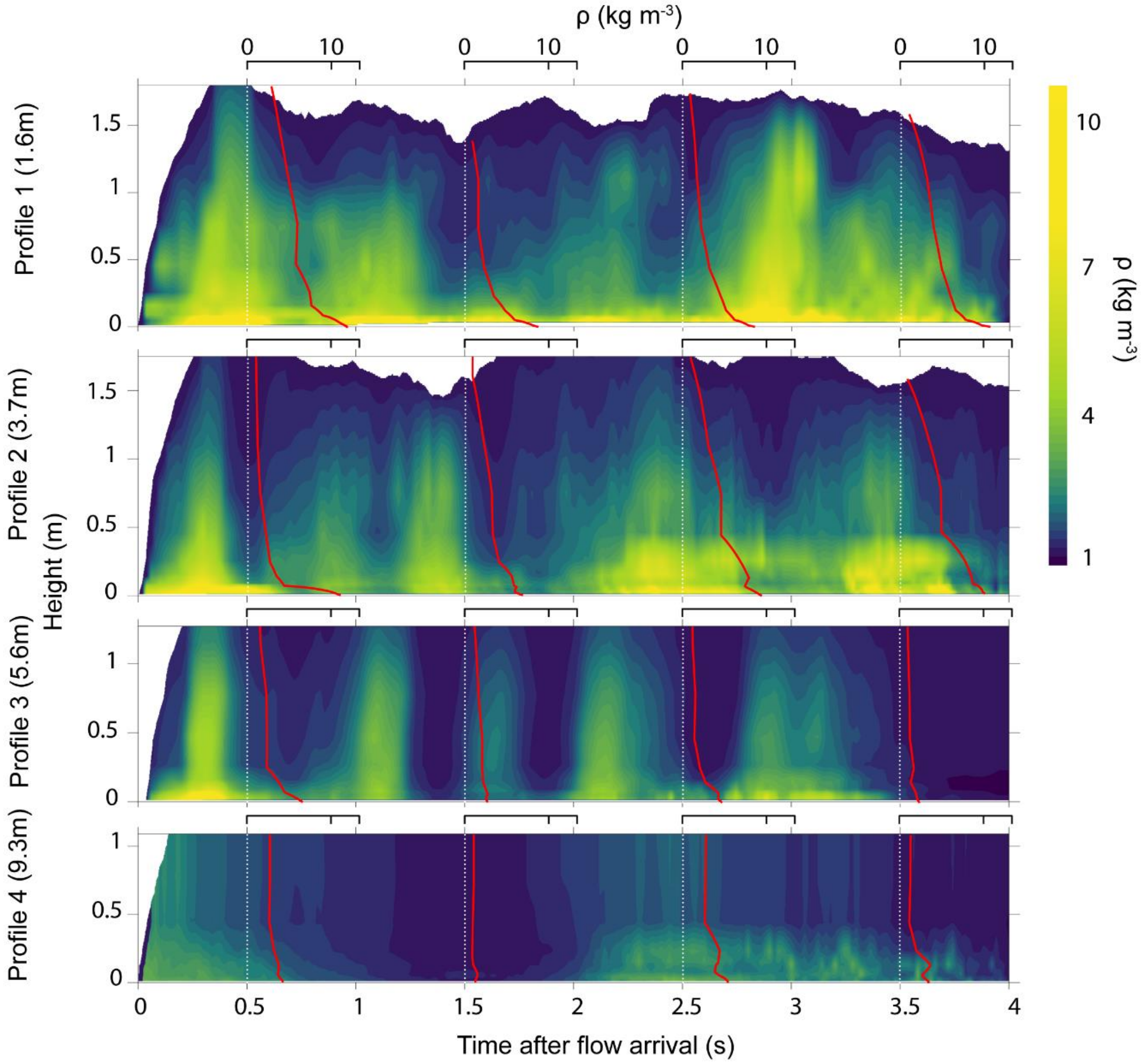

Figure 3-22: Flow density ρ contour plots of the rough experiment synthesised dilute PDC travelling on a rough substrate. Plotted vertical profiles of densities (red lines) are located at a one second interval. As the flow propagates with distance from source, flow density decreases due to sedimentation and entrainment of ambient air. Bulk density values (kg m^{-3}) of overall flow over 4 seconds: 2.69 (P1), 2.27(P2), 1.92(P3), 1.69(P4). Visible are regularly occurring oscillations at approx. 500 ms intervals at each static observer location across runout.

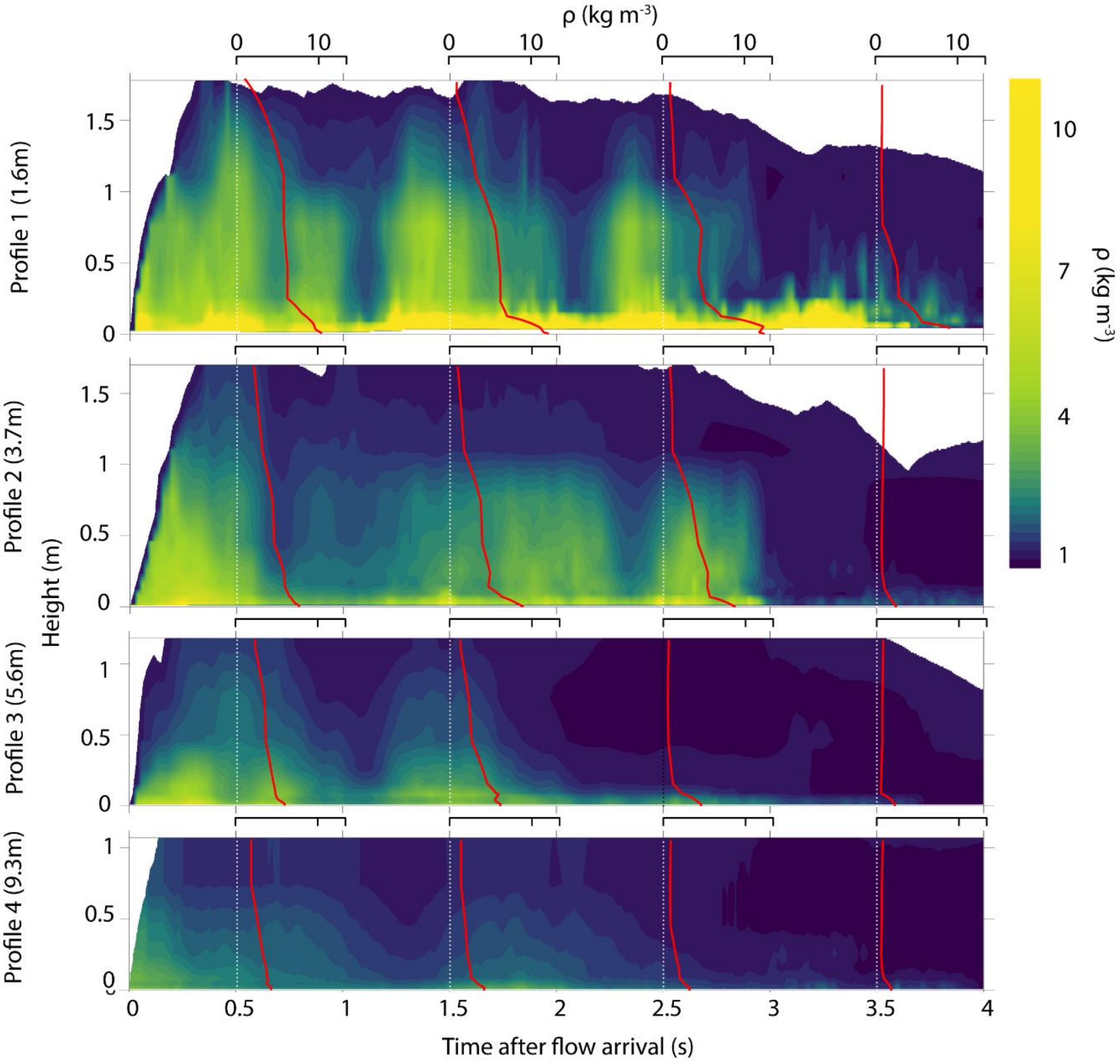

Figure 3-23: Flow density ρ contour plots of the smooth experiment synthesised dilute PDC travelling on a smooth substrate. Plotted vertical profiles of densities (red lines) are located at one second intervals after flow arrival. Density plots display systematic decrease of flow density over distance. Bulk density values (kg m^{-3}) of overall flow over 4 seconds: 2.68 (P1), 2.15(P2), 1.91(P3), 1.49(P4). Visibly are regularly occurring oscillations at approx. 1000ms intervals at each static observer location across runout.

The smooth and rough experiment flow velocity magnitude and densities show low-frequency oscillations described in Brosch et al. (2021).

Regularly occurring oscillation are more pronounced in the height-time contour plots of flow densities compared to velocity magnitudes. Density oscillations can be observed within the rough and smooth experiments flows (Figure 3-22 and Figure 3-23). Density peaks are characterised by values in the range of 1.5 to 2 kg m^{-3}, up to a flow passage time of 3.5 s at each static observer location. A total of four high density pulses (with an average period of 0.5 s) were observed to occur within the rough experiment flow over four seconds of flow passage at the observer locations. In contrast, the smooth experiment flow featured around three distinct pulses observed at the first profile location of 1.6 m runout distance. With distance from impact, the number of detectable density discontinuities decreased at each static observer location. Overall, internal density pulses in the rough experiment flow were characterised by a constant period, while density pulses appeared to shorten and converge in the smooth experiment flow. At the distal most observer location (9.3m) for both the rough and smooth experiments flows, the density pulses were restricted to the head and the tail of the flow. The longer flow duration of the rough experiment flow resulted in the presence of more internal discontinuities, compared to the shorter duration of the smooth experiment flow.

4. Discussion

4.1 Lateral correlation of experimental PDC deposit

Identified depositional lithofacies are interpreted and laterally correlated in the following section. Proximally, the experimental flows deposit is characterised by the presence of a large c 0.2m regressive dune structure that equates to c. 80 % of the final deposit volume. Medial-distal deposits are characterised by the laterally correlatable diachronous deposition of structurally comparable lithofacies.

Proximal deposits (up to 3 m in runout distance) are thickest and display the most variety in deposited lithofacies (Figure 4-1 rough experiment; Figure 4-2 smooth experiment). The presence of a large regressive dune structure characterizes deposition in the first c. 3m after impact.

At proximal regions, the front of the flow head is characterised by a strong non-depositional phase. The deposition of a fines depleted, massive, lapilli-ash (fpoormLT) lithofacies at 0.2s after flow arrival represents the first deposition at 1.6 m runout distance. Deposition of the fpoormLT lithofacies occurs through a c. 9.5 kg m^{-3} bedload region.

At 0.45 s after flow arrival, the middle of the head starts depositing a stratified, lapilli-ash (sLT) lithofacies. The deposition of the sLT lithofacies is characterised by deposition from an on average c. 11 kg m^{-3} dense tractional bedload. Deposition of the sLT lithofacies at the flow head in the proximal runout distance is interrupted by the deposition of a mLT lithofacies at the rear of the head.

The thickest lithofacies found in the proximal region are the massive, lapilli-ash (mLT) lithofacies (pink shaded units in the column located at 1.6m of Figure 4-1 rough experiment; Figure 4-2 smooth experiment). The mLT lithofacies are related to deposition through a 10 to 20 kg m^{-3} granular shifting sandwave in the bedload. In both substrate experiments, the mLT lithofacies are deposited by the highly granular shifting sandwaves and are restricted to the initial regressive dune structure found at <3 m of runout (pink shaded units in the column located at 1.6m of Figure 4-1 rough experiment; Figure 4-2 smooth experiment).

Shifting sandwaves in the proximal region are interpreted to have originated from the expanding flow of the laterally projected mixture at impact, wherein rapid settling of heavy uncoupled particles coinciding with the development of fast settling mesoscale clusters forms a granular fluid like basal underflow. Shifting sandwave sedimentation occurs from the back of the flow head and throughout the entire length of the flow body in the flow at proximal regions.

The c. 3 m long regressive dune structure observed in the proximal regions are interpreted to be the result of aggradation of successive thick units deposited by the granular shifting sandwave. It is interpreted that the lithofacies associated with the granular shifting sandwave pinch-out along with the termination of the dune (absence of pink shaded units after runout distance of 3 m, Figure 4-1 rough experiment; Figure 4-2 smooth experiment).

During periods at which shifting sandwave sedimentation is absent, deposition in the body of the flow at the proximal region shifts to tractional bedload aggradation. Tractional bedload aggradation at proximal regions, characterised by a 5-10 kg m^{-3} tractional bedload region, are associated with the aggradation of the sLT lithofacies (blue shaded units in the column located at 1.6m of Figure 4-1 rough experiment; Figure 4-2 smooth experiment).

Late-stage proximal massive, pumice-rich, lapilli-ash (mpLT) lithofacies reflects the shift from the flow distal body to tail. The late-stage flow characterised by flow dilution and deceleration results in the loss of flow competence in transporting particles. Deposition of the mpLT lithofacies characterises rapid deposition from a dense 8-15 kg m^{-3} bedload through rolling clasts and low tractional bedload aggradation. Deposition of the mpLT lithofacies through low traction aggradation occurs concurrently with the loss of lower flow stratification, and termination of the formation of fast settling mesoscale clusters.

The passage of the flow tail in proximal regions is characterised by the further deceleration of flow velocities (c. < 2 m s^{-1}). Individual lapilli clasts are observed to roll across and scour the deposit surface to form a discontinuous individual lapilli cover. Concurrently, over the course of seconds to tens of seconds very fine to fine ash particles slowly settle out of suspension from the buoyant ash cloud as the flow ceases lateral motion, forming the laminated, normally graded, ash (//sT$_{(n)}$) lithofacies (green shaded units in the column located at 1.6m of Figure 4-1 rough experiment; Figure 4-2 smooth experiment).

The range of densities displayed by the bedload whilst depositing various proximal lithofacies imply that the processes observed in the experimental lower flow region will also occur in natural flows. Observations of the laterally limited deposition of the mLT lithofacies associated with a highly mobile granular shifting sandwave in the proximal regions of the experiments give insights not only to the length scales at which equivalent natural lithofacies occur, but also the bedload processes responsible for depositing them. However, it is important to note that with the given results, the lateral extent of the associated proximal lithofacies on a field scale cannot be quantitatively predicted yet. Nonetheless, natural proximal massive lithofacies will also be in the scale of at least metres but could also potentially be further. Stratified lithofacies, on the other hand, are envisioned to laterally correlate downstream to medial and distal reaches (blue shaded units, Figure 4-1 rough experiment; Figure 4-2 smooth experiment).

At medial runout distances (c. 3-10m runout distance), absence of highly mobile shifting sandwaves is associated with the diachronous deposition of a laterally correlatable vertical sequence of lithofacies under an evolving flow structure.

The front of the flow at medial runout distances still displays a non-depositional front. Initial deposition at the head occurs at the middle-anterior portion of the head. The deposition of the fines depleted, massive, ash (fpoormT) lithofacies is characterised by the rapid aggradation from a 7-11 kg m^{-3} bedload region. The deposition of the bottommost fpoormT lithofacies at runout distance of 3.7 is interpreted to laterally correlate with the initial 2 depositional units in the proximal regions at both flows (blue shaded units, Figure 4-1 rough experiment; Figure 4-2 smooth experiment).

Over distance, the fpoormT lithofacies deposited by the head becomes thinner and finer, and at runout distances > 10 m, the internal structure evolves from being massive to being stratified, and at distances > 15 m, fpoormT becomes thinly laminated(graphical representation of the evolution of the bottommost units (shaded blue), from massive (blocks) to stratified (lines) and ultimately laminated (thin lines), Figure 4-1 rough experiment; Figure 4-2 smooth experiment). Changes in lithofacies over distance reflects the change in deposition mechanism, over distance, rapid deposition (which deposits massive lithofacies) becomes deposition through tractive processes (stratified to laminated lithofacies).

Unlike proximal regions (runout distance >3m), granular shifting sandwaves that initiate at the rear of the head and occur throughout the flow body are not observed. Instead, sediment transport mechanism occurring at the rear of the head and throughout the flow body are characterised by tractional bedload.

The back of the flow head at medial distances (3-10m runout distance) is characterised by a non-depositional and erosive phase. The fpoormT lithofacies that characterises deposition from the middle of the head of the flow is overlain with an unconformable contact due to this non-depositional and erosive phase. At distal runout distances (runout distance >10 m), the non-depositional region of the rear of the head dissipates, and contacts between depositional packages of the head and subsequent depositional units become conformable (Figure 4-1 rough experiment; Figure 4-2 smooth experiment).

At medial runout distances (3-10 m runout distance) the sediment transport mechanism in the lower flow boundary is characterised by tractional bedload mechanism. The development of a 5 - 10 kg m^{-3} dense bedload region in the flow body at 3.7 m runout distance occurs concurrently with the formation fast settling mesoscale clusters that feed into a 3 - 7 kg m^{-3} transient region. Deposition of stratified, ash (sT) lithofacies characterises deposition from a tractional bedload at the passage of the flow body at medial runout distances (3-10m runout distance).

Medial sT lithofacies can be correlated proximally to: i) faint stratifications found within mLT lithofacies (blue shaded horizons in the proximal deposits, Figure 4-1 rough experiment; Figure 4-2 smooth experiment); ii) and the sLT lithofacies (blue shaded stratified beds in the proximal deposits, Figure 4-1 rough experiment; Figure 4-2 smooth experiment). At distal runout distances (runout distance >10 m), sT lithofacies associated with the flow body becomes finer and stratifications evolve into laminations.

At the flow body-tail transition propagation at medial runout distances (< 7 m for the rough experiment deposit, and <5 m for the smooth experiment deposit), a 4-11 kg m^{-3} dense bedload deposits the massive, ash and massive, pumice rich, ash(mT/mpT) lithofacies rapidly. The deposition of the mT/mpT lithofacies represents deposition from a late-stage flow that is experiencing dilution and deceleration. The dilution and flow deceleration of the late-stage flow is also characterised by the termination of vertical stratification and formation of the turbulent mesoscale clusters. The bottom contact of the late stage massive lithofacies with the underlaying stratified lithofacies is conformable and sharp.

The mT/mpT lithofacies located at medial runout distances laterally correlate to the mpLT lithofacies in the proximal runout distances (blue shaded massive units found near the deposit surface, Figure 4-1 rough experiment; Figure 4-2 smooth experiment). Late-stage mT/mpT lithofacies pinch-out at medial runout distances (approximately c. 7 m runout distance in the rough experiment flow Figure 4-1; and approximately c. 5 m in the smooth experiment flow Figure 4-2).

Analogous to proximal regions, individual lapilli clasts are observed to roll across the deposit during the passage of the tail at medial runout distances (Figure 4-1 and Figure 4-2 lapilli dusting). Deposition of the Individual lapilli across the deposit surface from impact to 20 m runout distance display systematic grain size decrease as a function of distance. Deposition of individual lapilli clasts occurs alongside the deposition of the //sT$_{(n)}$ lithofacies in the tail. Slow settling of very fine to fine ash particles in weakly tractive conditions at the tail to buoyant ash cloud emplaces the //sT$_{(n)}$ lithofacies. The //sT$_{(n)}$ lithofacies mantles over the entire deposit surface and can be laterally correlated throughout the entire deposit surface.

Distal runout (> c. 10 m runout distance) deposit architecture is characterised by the //sT$_{(n)}$ lithofacies (Figure 4-1 rough experiment; Figure 4-2 smooth experiment). At distal runout distances, the flow is significantly diluted through entrainment of ambient gases and sedimentation from the base of the flow. The significantly diluted flow deposits the //sT$_{(n)}$ lithofacies initially through low tractive mechanism (in the flow head and body), and later through settling out of suspension of very fine ashes from the tail buoyant ash cloud (last stratigraphic profile at 18 m runout distance, Figure 4-1 rough experiment; Figure 4-2 smooth experiment). At distal runout distances, deposition from the head, body, and tail is wholly characterised by the //sT$_{(n)}$ lithofacies (last stratigraphic profile at 18 m runout distance, Figure 4-1 rough experiment; Figure 4-2 smooth experiment).

The table below summarizes the observed lithofacies, their lateral extent and deposition mechanism with their characteristic bedload density. The understanding of the density range at which the experimental lithofacies deposits over allows for the characterisation and approximation of the range at which equivalent lithofacies occur at nature.

Table 4-1: List of lithofacies, their depositional range (proximal 0-3, medial- 3-10, distal- >10 m runout distance), their depositional mechanism and the characteristic density range at bedload region during emplacement.

Lithofacies	Deposited region	Deposition mechanism	Bedload density kg m^{-3}	Depth integrated flow density kg m^{-3}
fpoormLT	Proximal	Rapid deposition	7.0-10.0	1.5-4.2
sLT	Proximal	Tractional bedload	6.0-15.0	2.5-4.2
mLT	Proximal	Shifting sandwaves	10.0-20.0	2.5-4.2
mpLT	Proximal	Low tractional bedload aggradation	8.0-15.0	1.9-4.0
fpoormT	Medial	Rapid deposition	7.0-11.0	1.3-2.3
mT/mPT	Medial	Low tractional bedload aggradation	4.0-11.0	1.4-2.3
sT	Medial-Distal	Tractional bedload	5.0-10.0	1.4-2.3
//sT(n)	Proximal-Distal	Grain by grain under weak tractive conditions	1.3-2	1.3-1.7

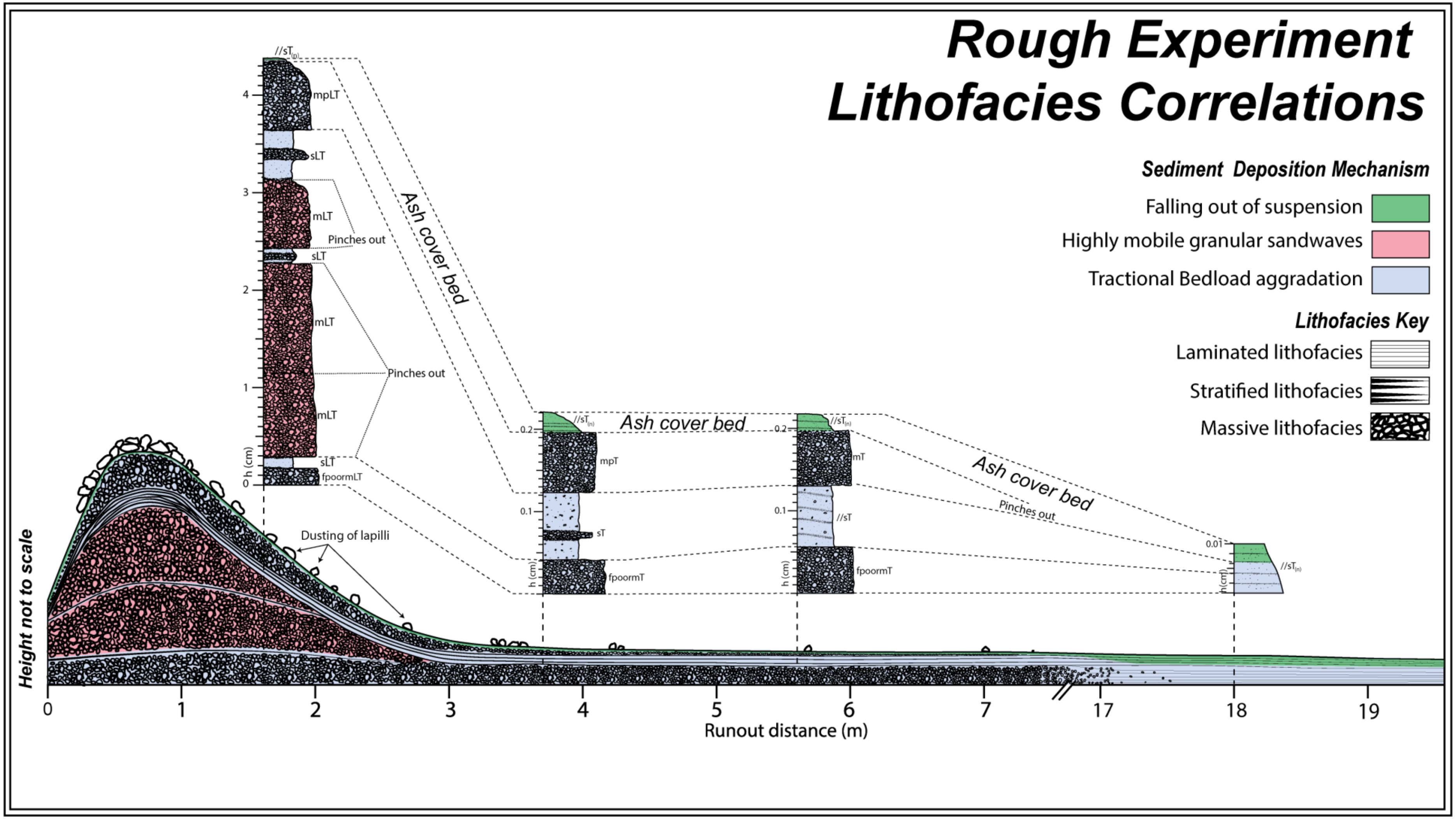

Figure 4-1: Schematic illustration of the lateral lithofacies variation of the deposit emplaced by the rough experiment's dilute PDC. Schematic illustration displays the lithofacies variation from proximal to distal runout distances. Colours delineate the different deposit emplacement mechanisms. Stratigraphical columns of static observation profiles (1.6, 3.7, 5.6 , and 18 m) and corresponding lithofacies correlations are displayed. A break in x axis located at 7 – 17 m runout distance. The proximal deposit (<3 m runout distance) is characterised by the occurrence of a large regressive dune structure mainly composed of lithofacies deposited by granular sandwaves.

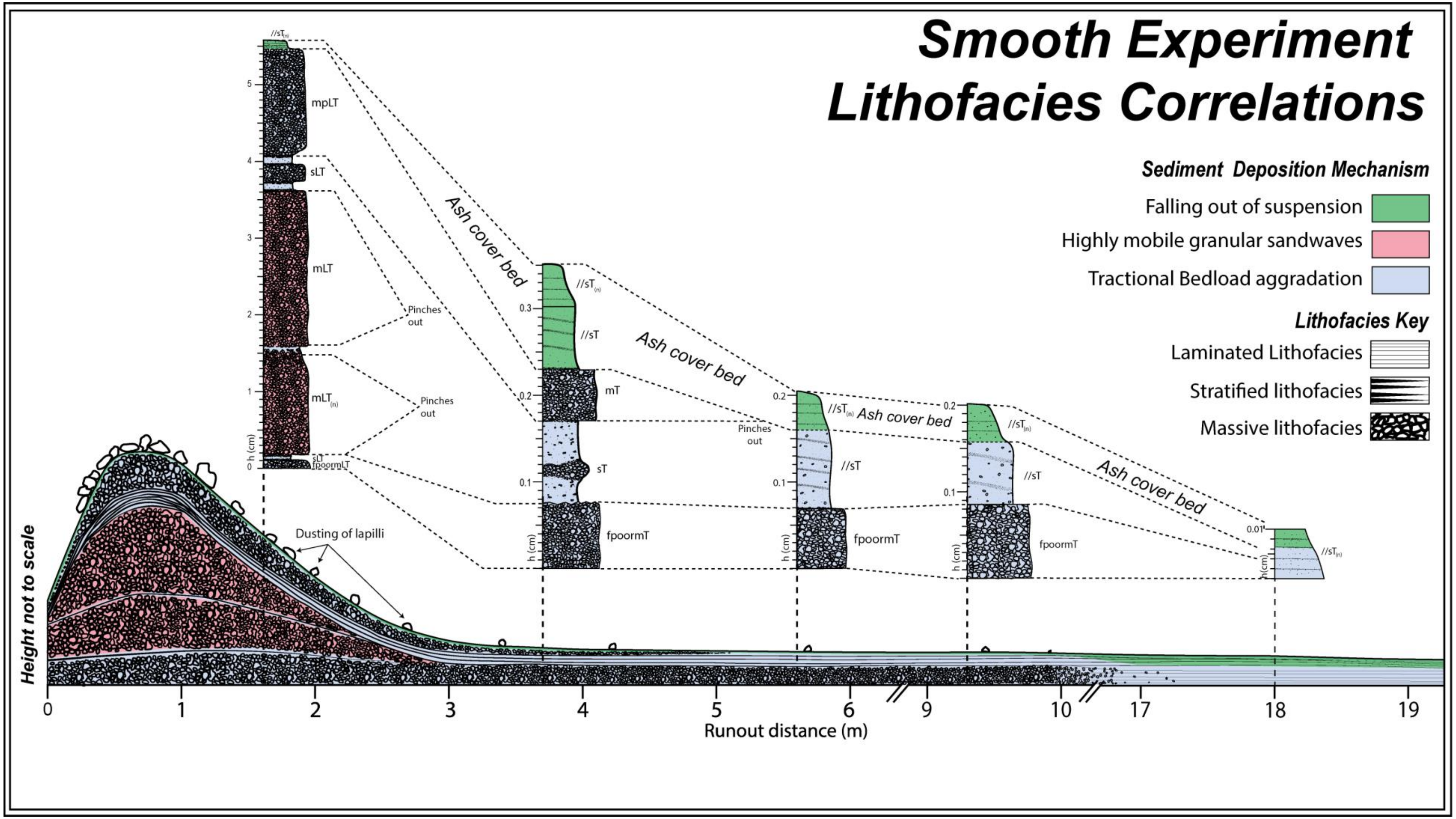

Figure 4-2: Schematic illustration of the lateral lithofacies variation of the deposit emplaced by the smooth experiment's dilute PDC. Schematic illustration displays the lithofacies variation from proximal to distal runout distances. Colours delineate the different deposit emplacement mechanisms. A break in x axis located at 6 – 9 and 10 – 17 m runout distance. Stratigraphical columns of static observation profiles (1.6, 3.7, 5.6 , and 18 m) and corresponding lithofacies correlations are displayed.

4.2 Effect of substrate roughness on deposition

The observations made on the deposit of the two different flows travelling on contrasting roughness allows for the discussion of the role that substrate roughness have on deposition.

Overall flow and depositional characteristics from the rough and smooth experiment flow display high degrees of similitude (Figure 4-1 and Figure 4-2). Proximally, both flows deposited a large regressive dune structure composed of thick mLT lithofacies. At both experiments, the proximal dune structure pinch-out at approximately 3m of runout distance. At medial to distal runout distances, both flows display very similar vertical and longitudinal lithofacies evolution.

Observed are the subtle local variations in deposition, i.e., lithofacies might be slightly thicker (mLT lithofacies at 1.6 m runout distance are thicker in the smooth experiment than the rough experiment (Figure 4-1 and Figure 4-2)), or runout further (late-stage massive lithofacies runout further in the deposit of the rough experiment flow compared to the smooth experiment flow (Figure 4-1 and Figure 4-2)).

In the cases of both experiments, the subtle differences in the thickness of the mLT lithofacies at the proximal regions cannot be attributed to differences in substrate roughness. This is because the effected lithofacies are not deposited onto the pure substrate roughness, but on a surface emplaced by the flow. Deposition from the dilute PDCs at the proximal location occurs at 0.2 s after flow arrival, after which the current traverses on an emplaced substrate. In the case of the rough experiment, the current deposition overcomes the effective roughness of the substrate (5mm) within 0.5s after flow arrival. While the current travelling on the hydraulically smooth surface traverses on the emplaced rougher surface. The first mLT lithofacies at both experiment is deposited after 0.5 s post flow arrival.

Runout distance of the late-stage massive lithofacies (mpT/mT) goes further in the rough substrate experiment (pinch-out at c. 7 m runout distance) compared to the smooth experiment (pinch-out at c. 5 m runout distance). At runout distance of c. 4 m after impact, the average deposit thickness of the rough experiment (c. 2 mm) is less than the effective substrate roughness (5 mm). By contrast, deposition from the current of the smooth experiment creates a rougher surface compared to the set boundary condition (hydraulically smooth). The effect that substrate roughness has on medial distance deposits are that of the slightly extended runout distance of late-stage lithofacies.

At both flows, especially the flow travelling on a hydraulically smooth surface at runout distance > 4 m, the only part of the flow that travels on the set substrate boundary condition is the front of the head. On average, the flow deposits 0.2-0.5 s after flow arrival. Subsequently, the flow deposition modifies the substrate roughness. In the rough experiment, at distances where deposit thickness overcomes the effective substrate roughness (5 mm), the deposition of material results in the loss of effective roughness. Alternatively, deposition from the flow travelling on a hydraulically smooth surface results in the generation of a rougher surface dependant on the grainsize of the deposited material.

4.3 Comparisons to natural PDC deposits

This section will discuss how the deposits emplaced by the experimental flows compare to ones observed in nature. As discussed in 4.2, the generated deposit of the flows travelling on contrasting substrate roughness are comparable, henceforth the experimental deposits from the two experiments will be treated the alike when comparing them to the observed natural deposits.

The recently mapped deposits of a blast-like surge deposit of the August 2012 eruption of Te Maari in New Zealand (Breard et al., 2015; Lube et al., 2014) shows a comparable ‘tripartite’ deposit structure to other previously mapped deposits of natural dilute PDCs (tripartite deposit structures have also been observed in deposits of : blast-like surges (Belousov et al., 2007; Cronin et al., 2013), phreatic explosions low-temperature surges (Fujinawa et al., 2008), and base surges (Dellino et al., 2004)).

The tripartite deposit, initially described in the deposits of a directed blast flow of Bezymianny volcano in Kamchatka, Russia (Belousov, 1996), defines a sequence that typically sits above a typically strong basal erosive unconformity. The tripartite architecture defines a sequence that includes a lower massive to faintly stratified bed (layer A), a middle stratified to laminated beds (layer B), and an uppermost planar-bedded stratified to laminated ashes (layer C). Furthermore, the nature of the contact between beds in units A and B is characterised by a strong erosive unconformity, though beds belonging to unit C only display a mildly erosive to conformable lower contact. The whole depositional sequence is sparsely speckled by lapilli and overlain by a thin cover bed of fine to very fine ash that is susceptible to reworking (Lube et al., 2014).

An interpretation of the deposition of the tripartite sequence is that each unit reflects the bypassing flow structure, i.e., the flow’s head (layer A), body (layer B), and tail (layer C). An alternative interpretation envisages a strongly vertically stratified current where particle size decreases as a function of height (Dellino et al., 2004; Valentine, 1987), and longitudinal variations were related to changes in concentration profiles and the flow’s capability in transporting particles of varying sizes.

The natural layer A, characterised by the massive, poorly sorted structure, is suggested to be deposited in a very rapid manner, with little to no lateral movement (Breard et al., 2015; Druitt, 1992). The suggested high particle concentration region behind the head is thought to have a dampening effect on local turbulence which results in the rapid deposition of the layer A (Esposti Ongaro et al., 2012; Lube et al., 2014).

The occurrence of a traction-dominated regime during the passage of the flow deposits layer B as a distinct stratified layer. Alternating coarse- and fine-grained laminae within layer B represent the unsteady nature of the flow-boundary-zone (Branney & Kokelaar, 2002). The last and slowest region of the flow deposits the laminated layer C through grain-by-grain aggradation under weak tractive conditions (Breard et al., 2015; Dellino et al., 2004).

Deposit architecture and vertical sequence of the experimental and natural flows reveals similarities. Proximal deposition of the experimental flow is characterised by thick mLT lithofacies that make up a large regressive dune structure. The regressive dune structure that can be found up to 3 m of runout distance is interpreted as an equivalent to the natural proximal breccia deposits (Breard et al., 2015; Fujinawa et al., 2008).

In natural directed blasts and blast-like PDCs, initial flow expansion is often supersonic and associated with the emplacement of a thick, massive breccia deposit before the development of a gravity current (Breard et al., 2015; Lube et al., 2014; Wohletz & Sheridan, 1979). In the case of the experimentally synthesised flow, the initially expanding flow after impact is wholly subsonic. The development of the gravity current structure occurs rapidly, and the formation of a proximal breccia deposit is not observed. Nevertheless, the proximal c. 3m long regressive dune structure composed mainly of mLT lithofacies may represent a comparable deposit of such proximal breccia deposit found in nature.

At medial to distal runout distances, the experimental flow deposits display a tripartite vertical sequence that is found in natural PDCs. In the case of the experimental flow, the tripartite sequence characterises depositional lithofacies that reflect the passage of, and deposition from the flow's head, body, and tail.

The fpoormLT/T lithofacies in the experimental flow characterises rapid deposition from the middle of the head through rapid sedimentation from a weakly developed tractional bedload; the deposition of the fpoormLT/T lithofacies associated with the head is interpreted as an equivalent to the natural layer A (Belousov et al. (2007); described as unit A by Breard et al. (2015)).

Deposition from experimental flow body through tractional bedload and concurrent formation of fast settling mesoscale clusters emplaces a stratified lithofacies (sLT/T, //sT). The emplaced stratified lithofacies through tractional bedload processes is envisaged to be equivalent to the natural layer B (Belousov et al. (2007); described as unit B by Breard et al. (2015)).

Up to medial runout distances (<7m runout length), transition in the waning flow from distal body to tail in the experimental flow is characterised by the rapid sedimentation of a mT lithofacies through low traction aggradation and rolling clasts. The massive late stage lithofacies is equivalent to the naturally occurring lower part of layer C (described as layer *Ca* by Belousov et al. (2007), and layer *A2a* by Fisher (1990), the lower part of layer C is found up to medial runout distances). It is suggested that the natural lower part of layer C is emplaced from a separate gravity flow that deposited layer B (Fisher, 1990), or alternatively deposition was from a waning phase current (Valentine, 1987). Otherwise, lower part of layer C has also been interpreted to originate from rapid sedimentation under a moderate concentration, weakly tractive conditions (Druitt, 1992).

The upper part of the natural deposit layer C (described as layer *Cb* by Belousov et al. (2007), and layer *A2b* by Fisher (1990)) is equivalent to the //sT$_{(n)}$ lithofacies deposited by the tail and buoyant ash cloud of the experimental flow. Low tractive and settling out of suspension is responsible for the deposition of the //sT$_{(n)}$ lithofacies in the experimental flow.

Deposition of the tripartite vertical sequence in the experimental flow shows that it is the product of deposition that reflects the bypassing of a flow head, body and tail. Over the runout distance, dilution from entrainment of ambient gas and deposition at the flow boundary leads overall fining of the deposition. It is also noted that over runout distance, rapid sedimentation mechanism (responsible for deposition of massive lithofacies) transitions into more tractional dominated sedimentation mechanism (responsible for deposition of stratified and laminated lithofacies in medial to distal runout distances). Resemblances between the experimental and natural deposit architecture suggests that particle deposition and erosion mechanism in play are also analogous.

In the following, results from this study will be compared to a similar study (Brosch & Lube, 2020) that made observations solely from a profile 1 equivalent (runout distance 1.6m).

Previous work looking into depositional processes of experimental dilute PDCs has suggested that prolonged tractional bedload deposition and erosion at the base of dilute PDCs are subordinate mechanism of deposition (Brosch & Lube, 2020). Instead, deposition at the base of the flow occurs mainly through the feeding of the bedload region by the transient region. The fluctuating transient region is in turn fed by the unsteady fast settling mesoscale clusters. The presence of the transient region, and the shifting sandwaves are attributed to be the dominant sediment transport mechanism within the lower flow region. Observations from the current study, however, suggests that the presence of the transient and tractional bedload region is independent from the occurrence of the granular shifting sandwaves.

At profile 1, the current study finds agreement with the statement that tractional bedload deposition and erosion is subordinate to shifting sandwave deposition (Brosch & Lube, 2020). The presence of the granular shifting sandwaves in this study is however, not attributed wholly to the formation of mesoscale clusters, instead, their presence is attributed to the rapid accumulation of particles in the bedload that were not effectively transported in the turbulent flow due to their high settling velocities. At periods when granular shifting sandwaves are absent, the fast-settling mesoscale clusters is observed to feed the transient region above a well-developed tractional bedload which subsequently deposits stratified lithofacies. It is envisaged that proximally, tractional bedload occurs throughout the passage of the flow during periods of strong mesoscale cluster formation, but deposition through the tractional bedload is overwhelmed by rapid deposition of massive lithofacies emplaced by the granular underflow.

Unlike Brosch and Lube (2020), the current study has allowed for the closer observation of sedimentation mechanism at medial runout distances (3 - 10 m after impact) due to the increased number of static observer locations. This study finds that deposition at medial runout distances do not relate with deposition from shifting sandwave sedimentation, but instead are characterised by: i) rapid deposition of massive lithofacies in the middle of the head; ii) deposition of a stratified lithofacies at the body from a well-developed tractional bedload with intense formation of fast settling mesoscale clusters; iii) a rapidly sedimented massive lithofacies (laterally limited) deposited through weak tractive conditions associated with the waning flow; iv) sedimentation of a laminated lithofacies under a weak tractive conditions from the tail and buoyant ash cloud.

4.4 Relationships between flow structure, deposit characteristic and spatiotemporal deposition

The findings of the oscillatory behaviour in sedimentation rate have led to an opportunity to observe the possible relationships between the evolving flow structure and the spatiotemporal deposition of dilute PDCs. Preliminary findings are reported in the following section.

4.4.A Periodicity in flow structure and sedimentation rate

Time-series data of the depth averaged flow density and dynamic pressure, and turbulence fluctuation reveal regular pulsatory behaviour of the flow (Figure 4-3). In this study, the flow is characterised by the occurrence of long-period oscillations of four to five density and dynamic pressure peaks in 4s. As observed by Brosch et al. (2021), the strongly time-correlated velocity, density and dynamic pressure oscillations in dilute PDCs are the result of the development of coherent, large-eddy structures within the turbulent dilute flow. The generation of coherent structures within the flow has been attributed to the shear with the lower and upper flow boundaries.

The temporal evolution of sedimentation rate also shows a similar oscillatory behaviour. Sedimentation rate in the rough experiment flow at 3.7 m runout distance is characterised by approximately three periods of sedimentation in 4s of flow passage. Sedimentation at profile 2 of the rough experiment indicate a strong anti-correlation between peaks in sedimentation rate and peaks of density, and dynamic pressure (plots of sedimentation rate, depth average density and dynamic pressure plotted against time after flow arrival, Figure 4-3). Peaks in flow densities and dynamic pressures are characterised by a minimal and negative values in sedimentation rate (shaded regions, Figure 4-3), while troughs in depth averaged values in density and dynamic pressure are indicative of periods of elevated sedimentation rate. The anti-correlative relationship does not display any time-shifts between the upper flow structure and deposition at the base of the flow.

Turbulence fluctuation in the flow wall region (0-0.2 m flow height) are also indicative of sedimentation rate (relationship between contour plot of turbulence fluctuation and sedimentation rate, Figure 4-3). A period of heightened turbulence fluctuation (blue colour in contour plot of turbulence fluctuation, Figure 4-3) in the wall region displays a minimum and negative value of sedimentation rate (shaded regions, Figure 4-3). In contrast, periods of decreased turbulence fluctuation (blue colour of turbulence fluctuation, Figure 4-3) in the wall region are characterised by an increase value of sedimentation rate.

The deposition of the fpoormT lithofacies (unit I, Figure 4-3) at the head occurs as density, and dynamic pressure begins to decrease from a maximum. The passing of the first turbulent structure leads to the rapid uninterrupted deposition of the unit I. Deposition of unit II (sT lithofacies) at the body is characterised by interrupted sedimentation due to the passage of approximately two to three turbulent structures. Deposition of unit III (mpT) in the tail is related to the decrease in dynamic pressure leading to the loss of the ability of the flow to transport particles in a sustained tractional bedload. Late-stage flow tail and buoyant ash cloud, characterised by the absence of coherent turbulent structures, emplaces a final ash cover bed (//$sT_{(n)}$) over seconds to tens of seconds.

As suggested by Andrews and Manga (2012), the passage of a single turbulent flow structure in a dilute PDC is recorded as a single continuous lamina in the final deposit. The current study finds that the passage of three to four coherent turbulent structures at runout distance of 3.7m of the rough experiment flow is characterised by the deposition of four depositional units. Each depositional unit represents a period between the passage of coherent turbulent structures. Moreover, the passage of coherent turbulent structures within the lower flow regions is characterized by erosion and muted sedimentation rates. However, these findings are not reported by Andrews and Manga (2012), the scaling limitations in their flows failed to display the suppressed sedimentation at the passage of a coherent turbulent structure.

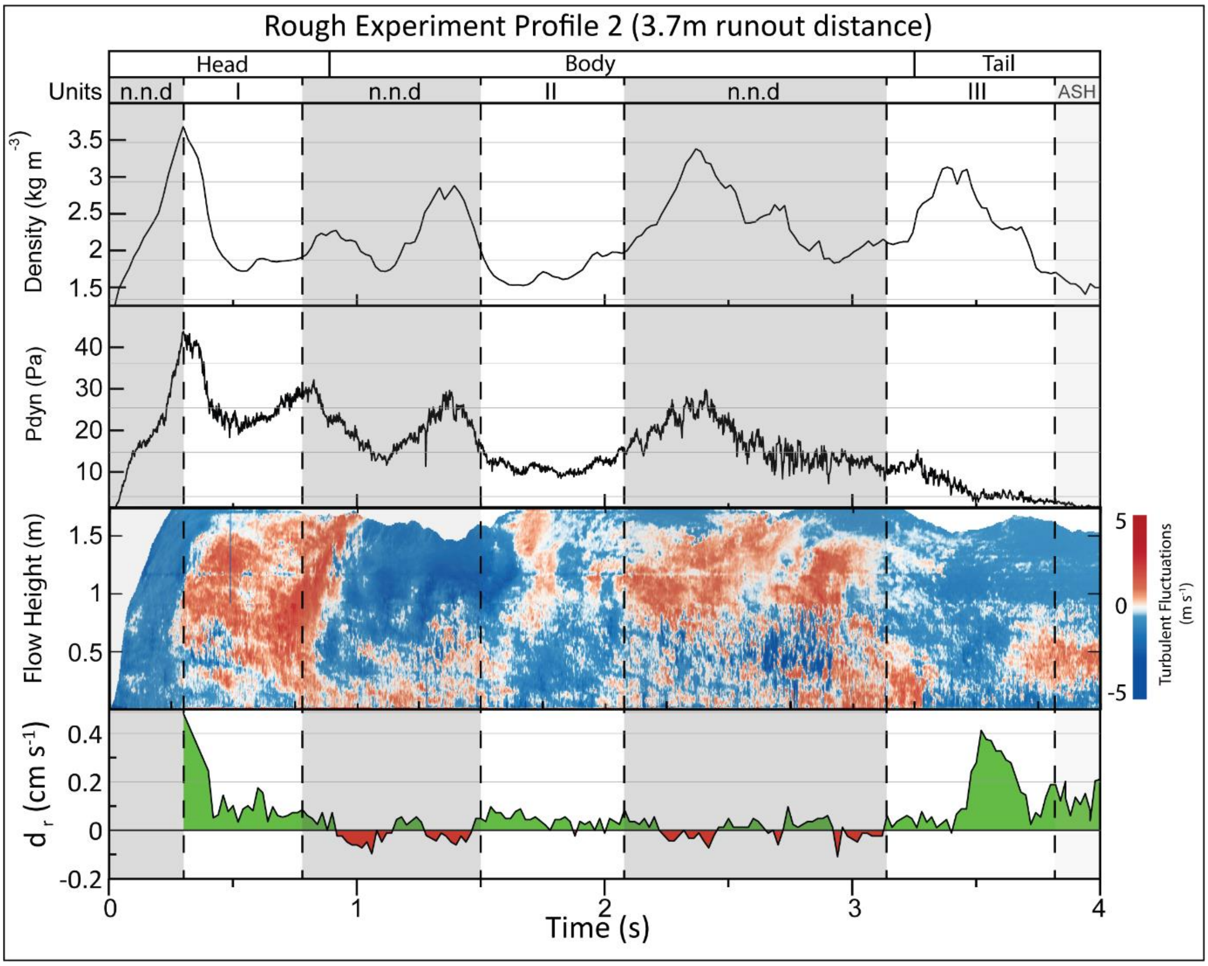

Figure 4-3: Comparison of measured depth averaged flow properties (Density (y-axis begins at ambient density c. 1.2kg m^{-3}), Dynamic pressure (Pdyn)) and contour plot of turbulence fluctuation against sedimentation rate (d_r) over a period of 4 s of flow passage at static observer profile located at 3.7 m runout distance of the rough experiment flow. For better visualization negative values in the sedimentation rate is shaded red, whilst positive values have been shaded green. At medial runout distances, deposition rate exhibit periods of no net deposition (n.n.d). Three to four depth averaged density and dynamic pressure peaks over 4s of flow passage characterises the passage of a coherent turbulent structures. Sedimentation rate also display approximately three peaks in sedimentation rate over 4 s of flow passage. Sedimentation rate peaks shows strong anticorrelation with depth averaged density and dynamic pressure peaks. Sedimentation rate increase is characterised with the negative slope in density and dynamic pressure curves with minimal time shift. Moreover, increase in sedimentation rate is characterised by a minimum value in turbulence fluctuation at the wall region (flow height 0-0.2m). These findings show, for the first time, the role coherent turbulent structures have on dilute PDCs sedimentation.

5. Conclusion

This MSc research is centred around furthering the understanding of deposition of dilute pyroclastic density currents. The utilization of a novel large-scale experimental approach allows for the observation and characterization of the spatio-temporal evolution of sedimentation from a well scaled dilute PDC. A total of two experimental flows were synthesised on differing substrate roughness, one on a hydraulically smooth surface and another on a rough plate composing of pebbles sized 3 to -2 φ in diameter. The flow velocity, density, dynamic pressure and observations of the temporally variant deposit formation were measured at four different static observer profiles. Through internal flow measurements, the sedimentation and deposition mechanisms of the dilute PDCs were subsequently characterised. The main findings of this research are:

- Lateral evolution in deposit lithofacies reflects overall flow dilution and deceleration.
- Final deposit architecture does not vary considerably between different roughness, due to the capability of the flow to generate and subsequently travel on their own roughness.
- The emplaced deposits of the experimental PDC display a ‘tripartite’ structure which has been commonly observed in natural deposits generated by blast, blast-like PDC and base surges.
- The emplaced tripartite structure at medial-distal runout lengths reflects the passage of a flow with a: i) head, ii) body and iii) tail and iv) buoyant ash cloud structure.
- The front of the PDC is characterised by a non-depositional region at proximal to medial runout distances.
- Deposition of dilute PDCs at proximal runout distances is characterised by massive deposits that are rapidly deposited from highly mobile granular basal underflows.
- At medial runout distances, rapid sedimentation is responsible for deposition of a massive lithofacies at the middle of the head
- Tractional bedload deposition at the flow body is characterised by deposition of stratified lithofacies which coincides with the formation of fast-settling mesoscale clusters at the lower flow regions.

- Rapid deposition of a laterally limited late-stage massive lithofacies occurs at through low traction aggradation at the flow body-tail transition
- Deposition of suspended particles emplaces a laminated lithofacies under low-tractive conditions at the flow tail and buoyant ash cloud
- Flow sedimentation rate show anti-correlation with depth average density, dynamic pressure and turbulence fluctuations values.
- Sedimentation rate is elevated during periods of declining depth averaged density, and dynamic pressure. Sedimentation rate is only affected by turbulence fluctuation values in the wall region.
- Deposition from dilute PDCs at medial-distal runout distances are largely controlled by the passage of coherent turbulent structures.

6. References

Andrews, B. J., & Manga, M. (2011). Effects of topography on pyroclastic density current runout and formation of coignimbrites. *Geology*, *39*(12), 1099-1102. https://doi.org/10.1130/g32226.1

Andrews, B. J., & Manga, M. (2012). Experimental study of turbulence, sedimentation, and coignimbrite mass partitioning in dilute pyroclastic density currents. *Journal of Volcanology and Geothermal Research*, *225-226*, 30-44. https://doi.org/https://doi.org/10.1016/j.jvolgeores.2012.02.011

Auker, M. R., Sparks, R. S. J., Siebert, L., Crosweller, H. S., & Ewert, J. (2013). A statistical analysis of the global historical volcanic fatalities record. *Journal of Applied Volcanology*, *2*(1), 2. https://doi.org/10.1186/2191-5040-2-2

Belousov, A. (1996). Deposits of the 30 march 1956 directed blast at bezymianny volcano, kamchatka, russia. *Bulletin of Volcanology*, *57*(8), 649-662. https://doi.org/10.1007/s004450050118

Belousov, A., Voight, B., & Belousova, M. (2007). Directed blasts and blast-generated pyroclastic density currents: A comparison of the bezymianny 1956, mount st helens 1980, and soufrière hills, montserrat 1997 eruptions and deposits. *Bulletin of Volcanology*, *69*(7), 701. https://doi.org/10.1007/s00445-006-0109-y

Best, J., & Bridge, J. (1992). The morphology and dynamics of low amplitude bedwaves upon upper stage plane beds and the preservation of planar laminae. *Sedimentology*, *39*(5), 737-752.

Bouma, A. H., Kuenen, P. H., & Shepard , F. P. (1962). *Sedimentology of some flysch deposits : A graphic approach to facies interpretation*. Elsevier Pub. Co.

Bourdier, J. L., Boudon, G., & Gourgaud, A. (1989). Stratigraphy of the 1902 and 1929 nuée-ardente deposits, mt. Pelée, martinique. *Journal of Volcanology and Geothermal Research*, *38*(1), 77-96. https://doi.org/https://doi.org/10.1016/0377-0273(89)90031-0

Branney, M. J., & Kokelaar, B. P. (2002). Pyroclastic density currents and the sedimentation of ignimbrites.

Breard, E. C. P., Lube, G., Cronin, S. J., & Valentine, G. A. (2015). Transport and deposition processes of the hydrothermal blast of the 6 august 2012 te maari eruption, mt. Tongariro. *Bulletin of Volcanology*, *77*(11), 100. https://doi.org/10.1007/s00445-015-0980-5

Breard, E. C. P., & Lube, G. (2017). Inside pyroclastic density currents – uncovering the enigmatic flow structure and transport behaviour in large-scale experiments. *Earth and Planetary Science Letters*, *458*, 22-36. https://doi.org/https://doi.org/10.1016/j.epsl.2016.10.016

Brosch, E., & Lube, G. (2020). Spatiotemporal sediment transport and deposition processes in experimental dilute pyroclastic density currents. *Journal of Volcanology and Geothermal Research*, *401*, 106946. https://doi.org/https://doi.org/10.1016/j.jvolgeores.2020.106946

Brosch, E., Lube, G., Cerminara, M., Esposti-Ongaro, T., Breard, E. C. P., Dufek, J., Sovilla, B., & Fullard, L. (2021). Destructiveness of pyroclastic surges controlled by turbulent fluctuations. *Nature Communications*, *12*(1), 7306. https://doi.org/10.1038/s41467-021-27517-9

Burgisser, A., Bergantz, G. W., & Breidenthal, R. E. (2005). Addressing complexity in laboratory experiments: The scaling of dilute multiphase flows in magmatic systems. *Journal of Volcanology and Geothermal Research*, *141*(3-4), 245-265.

Clarke, A. B., & Voight, B. (2000). Pyroclastic current dynamic pressure from aerodynamics of tree or pole blow-down. *Journal of Volcanology and Geothermal Research*, *100*(1), 395-412. https://doi.org/https://doi.org/10.1016/S0377-0273(00)00148-7

Cronin, S. J., Lube, G., Dayudi, D. S., Sumarti, S., & Subrandiyo, S. (2013). Insights into the october–november 2010 gunung merapi eruption (central java, indonesia) from the stratigraphy, volume and characteristics of its pyroclastic deposits. *Journal of Volcanology and Geothermal Research*, *261*, 244-259.

Crowe, B. M., & Fisher, R. V. (1973). Sedimentary structures in base-surge deposits with special reference to cross-bedding, ubehebe craters, death valley, california. *GSA Bulletin*, *84*(2), 663-682. https://doi.org/10.1130/0016-7606(1973)84

Dellino, P., & La Volpe, L. (2000). Structures and grain size distribution in surge deposits as a tool for modelling the dynamics of dilute pyroclastic density currents at la fossa di vulcano (aeolian islands, italy). *Journal of Volcanology and Geothermal Research*, *96*(1), 57-78. https://doi.org/https://doi.org/10.1016/S0377-0273(99)00140-7

Dellino, P., Isaia, R., & Veneruso, M. (2004). Turbulent boundary layer shear flows as an approximation of base surges at campi flegrei (southern italy). *Journal of Volcanology and Geothermal Research*, *133*, 211-228. https://doi.org/10.1016/s0377-0273(03)00399-8

Dellino, P., Mele, D., Sulpizio, R., La Volpe, L., & Braia, G. (2008). A method for the calculation of the impact parameters of dilute pyroclastic density currents based on deposit particle characteristics. *Journal of Geophysical Research: Solid Earth*, *113*(B7).

Dellino, P., Zimanowski, B., Büttner, R., La Volpe, L., Mele, D., & Sulpizio, R. (2007). Large-scale experiments on the mechanics of pyroclastic flows: Design, engineering, and first results. *Journal of Geophysical Research: Solid Earth*, *112*(B4). https://doi.org/https://doi.org/10.1029/2006JB004313

Dioguardi, F., & Mele, D. (2018). Pyflow_2.0: A computer program for calculating flow properties and impact parameters of past dilute pyroclastic density currents based on field data. *Bulletin of Volcanology*, *80*(3), 28. https://doi.org/10.1007/s00445-017-1191-z

Douillet, G. A., Tsang-Hin-Sun, È., Kueppers, U., Letort, J., Pacheco, D. A., Goldstein, F., Von Aulock, F., Lavallée, Y., Hanson, J. B., Bustillos, J., Robin, C., Ramón, P., Hall, M., & Dingwell, D. B. (2013). Sedimentology and geomorphology of the deposits from the august 2006 pyroclastic density currents at tungurahua volcano, ecuador. *Bulletin of Volcanology*, *75*(11), 765. https://doi.org/10.1007/s00445-013-0765-7

Druitt, T. H. (1992). Emplacement of the 18 may 1980 lateral blast deposit ene of mount st. Helens, washington. *Bulletin of Volcanology*, *54*(7), 554-572. https://doi.org/10.1007/BF00569940

Dufek, J. (2016). The fluid mechanics of pyroclastic density currents. *Annual Review of Fluid Mechanics*, *48*(1), 459-485. https://doi.org/10.1146/annurev-fluid-122414-034252

Esposti Ongaro, T., Clarke, A. B., Voight, B., Neri, A., & Widiwijayanti, C. (2012). Multiphase flow dynamics of pyroclastic density currents during the may 18, 1980 lateral blast of mount st. Helens [https://doi.org/10.1029/2011JB009081]. *Journal of Geophysical Research: Solid Earth*, *117*(B6). https://doi.org/https://doi.org/10.1029/2011JB009081

Fisher, R., & Waters, A. (1969). Bed forms in base-surge deposits: Lunar implications. *Science*, *165*(3900), 1349-1352.

Fisher, R. V. (1990). Transport and deposition of a pyroclastic surge across an area of high relief: The 18 may 1980 eruption of mount st. Helens, washington. *GSA Bulletin*, *102*(8), 1038-1054. https://doi.org/10.1130/0016-7606(1990)102

Fujinawa, A., Ban, M., Ohba, T., Kontani, K., & Miura, K. (2008). Characterization of low-temperature pyroclastic surges that occurred in the northeastern japan arc during the late 19th century. *Journal of Volcanology and Geothermal Research*, *178*(1), 113-130.

Gardner, J. E., Nazworth, C., Helper, M. A., & Andrews, B. J. (2018). Inferring the nature of pyroclastic density currents from tree damage: The 18 may 1980 blast surge of mount st. Helens, USA. *Geology*, *46*(9), 795-798. https://doi.org/10.1130/g45353.1

Hjulstrom, F. (1935). Studies of the morphological activity of rivers as illustrated by the river fyris, bulletin. *Geological Institute Upsalsa*, *25*, 221-527.

Hoblitt, R. P. (1986). *Observations of the eruptions of july 22 and august 7, 1980, at mount st. Helens, washington* [Report](1335). (Professional Paper, Issue. http://pubs.er.usgs.gov/publication/pp1335

Huppert, H. E., & Simpson, J. E. (1980). The slumping of gravity currents. *Journal of Fluid Mechanics*, *99*(4), 785-799. https://doi.org/10.1017/S0022112080000894

Inman, D. L. (1952). Measures for describing the size distribution of sediments. *Journal of Sedimentary Research*, *22*(3), 125-145. https://doi.org/10.1306/d42694db-2b26-11d7-8648000102c1865d

Jenkins, S., Komorowski, J. C., Baxter, P. J., Spence, R., Picquout, A., Lavigne, F., & Surono. (2013). The merapi 2010 eruption: An interdisciplinary impact assessment methodology for studying pyroclastic density current dynamics. *Journal of Volcanology and Geothermal Research*, *261*, 316-329. https://doi.org/https://doi.org/10.1016/j.jvolgeores.2013.02.012

Lacroix, A. (1904). *La montagne pelée et ses éruptions*. Masson.

Lipman, P. W., & Mullineaux, D. R. (1981). *The 1980 eruptions of mount st. Helens, washington* [Report](1250). (Professional Paper, Issue. G. P. O. U.S. http://pubs.er.usgs.gov/publication/pp1250

Livingstone, I., Wiggs, G. F., & Weaver, C. M. (2007). Geomorphology of desert sand dunes: A review of recent progress. *Earth-science reviews*, *80*(3-4), 239-257.

Lube, G., Breard, E., Cronin, S., & Jones, J. (2015). Synthesizing large-scale pyroclastic flows: Experimental design, scaling, and first results from pele. *Journal of Geophysical Research: Solid Earth*, *120*(3), 1487-1502.

Lube, G., Breard, E. C., Cronin, S. J., Procter, J. N., Brenna, M., Moebis, A., Pardo, N., Stewart, R. B., Jolly, A., & Fournier, N. (2014). Dynamics of surges generated by hydrothermal blasts during the 6 august 2012 te maari eruption, mt. Tongariro, new zealand. *Journal of Volcanology and Geothermal Research*, *286*, 348-366.

Lube, G., Breard, E. C. P., Esposti-Ongaro, T., Dufek, J., & Brand, B. (2020). Multiphase flow behaviour and hazard prediction of pyroclastic density currents. *Nature Reviews Earth & Environment*, *1*(7), 348-365. https://doi.org/10.1038/s43017-020-0064-8

Lube, G., Breard, E. C. P., Jones, J., Fullard, L., Dufek, J., Cronin, S. J., & Wang, T. (2019). Generation of air lubrication within pyroclastic density currents. *Nature Geoscience*, *12*(5), 381-386. https://doi.org/10.1038/s41561-019-0338-2

Middleton, G. V. (1965). Antidune cross-bedding in a large flume. *Journal of Sedimentary Research*, *35*(4), 922-927. https://doi.org/10.1306/74d713ac-2b21-11d7-8648000102c1865d

Scharff, L., Hort, M., & Varley, N. R. (2019). First in-situ observation of a moving natural pyroclastic density current using doppler radar. *Scientific Reports*, *9*(1), 7386. https://doi.org/10.1038/s41598-019-43620-w

Schmincke, H.-U., Fisher, R. V., & Waters, A. C. (1973). Antidune and chute and pool structures in the base surge deposits of the laacher see area, germany [https://doi.org/10.1111/j.1365-3091.1973.tb01632.x]. *Sedimentology*, *20*(4), 553-574. https://doi.org/https://doi.org/10.1111/j.1365-3091.1973.tb01632.x

Simpson, J. E. (1999). *Gravity currents: In the environment and the laboratory*. Cambridge university press.

Small, C., & Naumann, T. (2001). The global distribution of human population and recent volcanism. *Global Environmental Change Part B: Environmental Hazards*, *3*(3), 93-109. https://doi.org/10.3763/ehaz.2001.0309

Smith, G., Rowley, P., Williams, R., Giordano, G., Trolese, M., Silleni, A., Parsons, D. R., & Capon, S. (2020). A bedform phase diagram for dense granular currents. *Nature Communications*, *11*(1), 2873. https://doi.org/10.1038/s41467-020-16657-z

Sparks, R. S. J. (1976). Grain size variations in ignimbrites and implications for the transport of pyroclastic flows. *Sedimentology*, *23*(2), 147-188.

Sulpizio, R., Dellino, P., Doronzo, D. M., & Sarocchi, D. (2014). Pyroclastic density currents: State of the art and perspectives. *Journal of Volcanology and Geothermal Research*, *283*, 36-65. https://doi.org/https://doi.org/10.1016/j.jvolgeores.2014.06.014

Valentine, G. A. (1987). Stratified flow in pyroclastic surges. *Bulletin of Volcanology*, *49*(4), 616-630. https://doi.org/10.1007/BF01079967

Valentine, G. A. (1998). Damage to structures by pyroclastic flows and surges, inferred from nuclear weapons effects. *Journal of Volcanology and Geothermal Research*, *87*(1), 117-140. https://doi.org/https://doi.org/10.1016/S0377-0273(98)00094-8

Wohletz, K., & Sheridan, M. (1979). A model of pyroclastic surge. *Geol. Soc. Am. Spec. Paper*, *180*. https://doi.org/10.1130/SPE180-p177

Wohletz, K. (2001). Pyroclastic surges and compressible two-phase flow. *From magma to tephra*.